Optimization of High-order Harmonic Generation for Attosecond Science

Weissenbilder, Robin

2023

Document Version:
Publisher's PDF, also known as Version of record

Citation for published version (APA):
Weissenbilder, R. (2023). *Optimization of High-order Harmonic Generation for Attosecond Science*. Department of Physics, Lund University.

Total number of authors:
1

LUND UNIVERSITY

PO Box 117
221 00 Lund
+46 46-222 00 00

Optimization of High-order Harmonic Generation for Attosecond Science

ROBIN WEISSENBILDER
ATOMIC PHYSICS | FACULTY OF ENGINEERING | LUND UNIVERSITY

Optimization of High-order Harmonic Generation for Attosecond Science

Optimization of High-order Harmonic Generation for Attosecond Science

by Robin Weissenbilder

Thesis for the degree of PhD in Physics
Thesis advisors: Prof. Anne L'Huillier, Dr. Cord L. Arnold,
Dr. Mathieu Gisselbrecht
Faculty opponent: Dr. Carlos Hernández-García

To be presented, with the permission of the Faculty of Engineering, LTH of Lund University, for public criticism in Rydberg lecture hall at the Department of Physics on Friday, the 27th of October 2023 at 09:15.

Organization
LUND UNIVERSITY

Atomic Physics
Box 118
SE–221 00 LUND
Sweden

Document name
DOCTORAL DISSERTATION

Date of disputation
2023-10-27

Sponsoring organization

Author(s)
Robin Weissenbilder

Title and subtitle
Optimization of High-order Harmonic Generation for Attosecond Science

Abstract

High-order harmonic generation is a highly nonlinear, though inherently inefficient, process which can lead to emission of coherent, broadband extreme ultraviolet radiation in the form of attosecond pulses. Attosecond pulses are crucial for experiments investigating photoionization dynamics on the femto- and attosecond timescales. As attosecond research tends towards increasingly complex light-matter interactions, demands on high flux attosecond sources grow. This thesis deals with light-matter interactions in the non-perturbative and perturbative regimes. Optimal generation of high-order harmonics in gases is studied, and the attosecond pulses are applied in two-photon pump-probe photoelectron interferometry schemes to unravel photoionization dynamics on the intrinsic timescales of the electron.

The first part of this thesis focuses on optimization of the conversion efficiency in high-order harmonic generation in gases, with emphasis on macroscopic phase-matching effects. We explain the large variety of gas target designs in the literature through an analytic model. The model predicts, independently of the driving laser focusing geometry, that efficient high-order harmonic generation is possible for a wide range of densities and medium lengths, if these follow a hyperbolic relation. The model suggests the existence of two phase-matching regimes with similar efficiency but different spatial and temporal characteristics of the emitted extreme ultraviolet radiation. We verify the model for a wide range of generation parameters experimentally and using numerical simulations.

The second part of this thesis concerns the application of attosecond pulse trains, consisting of high-order harmonics, to infer information about electron correlations in atoms. Photoionization dynamics occurring on the femto- and attosecond timescales are probed by measuring the amplitude and phase of oscillations in the photoelectron signal, induced by path interference of two-photon transitions. Two interference techniques are used: First, Reconstruction of Attosecond Beatings By Interference of Two-photon transitions (RABBIT) is used to study (i) photonionization time delays across the 4d giant dipole resonance in xenon, (ii) resonant below-threshold two-photon ionization of the 1s3p, 1s4p and 1s5p Rydberg states in helium and (iii) autoionization dynamics from the $3s^1 3p^6 4p$ Fano resonance in argon. Secondly, to fully characterize mixed photoelectron quantum states, a quantum state tomography protocol for photoelectrons (KRAKEN) is developed theoretically and tested experimentally for non-resonant photoionization of helium and argon.

DOKUMENTDATABLAD enl SIS 61 41 21

Key words
High-order Harmonic Generation, Attosecond, Photoionization

Classification system and/or index terms (if any)

Supplementary bibliographical information

Language
English

ISSN and key title
0281-2762

ISBN
978-91-8039-742-1 (print)
978-91-8039-741-4 (pdf)

Recipient's notes

Number of pages
277

Price

Security classification

I, the undersigned, being the copyright owner of the abstract of the above-mentioned dissertation, hereby grant to all reference sources the permission to publish and disseminate the abstract of the above-mentioned dissertation.

Signature ____________________

Date 2023-09-11

Optimization of High-order Harmonic Generation for Attosecond Science

by Robin Weissenbilder

LUND
UNIVERSITY

Funding information: The thesis work was financially supported by the Swedish Research Council, the European Research Council, infrastructure support by LTH and the Knut and Alice Wallenberg Foundation.

Faculty of Engineering, LTH, Atomic Physics

ISBN: 978-91-8039-742-1 (print)
ISBN: 978-91-8039-741-4 (pdf)
ISSN: 0281-2762

Printed in Sweden by Media-Tryck, Lund University, Lund 2023

Abstract

High-order harmonic generation is a highly nonlinear, though inherently inefficient, process which can lead to emission of coherent, broadband extreme ultraviolet radiation in the form of attosecond pulses. Attosecond pulses are crucial for experiments investigating photoionization dynamics on the femto- and attosecond timescales. As attosecond research tends towards increasingly complex light-matter interactions, demands on high flux attosecond sources grow. This thesis deals with light-matter interactions in the non-perturbative and perturbative regimes. Optimal generation of high-order harmonics in gases is studied, and the attosecond pulses are applied in two-photon pump-probe photoelectron interferometry schemes to unravel photoionization dynamics on the intrinsic timescales of the electron.

The first part of this thesis focuses on optimization of the conversion efficiency in high-order harmonic generation in gases, with emphasis on macroscopic phase-matching effects. We explain the large variety of gas target designs in the literature through an analytic model. The model predicts, independently of the driving laser focusing geometry, that efficient high-order harmonic generation is possible for a wide range of densities and medium lengths, if these follow a hyperbolic relation. The model suggests the existence of two phase-matching regimes with similar efficiency but different spatial and temporal characteristics of the emitted extreme ultraviolet radiation. We verify the model for a wide range of generation parameters experimentally and using numerical simulations.

The second part of this thesis concerns the application of attosecond pulse trains, consisting of high-order harmonics, to infer information about electron correlations in atoms. Photoionization dynamics occurring on the femto- and attosecond timescales are probed by measuring the amplitude and phase of oscillations in the photoelectron signal, induced by path interference of two-photon transitions. Two interference techniques are used: First, Reconstruction of Attosecond Beatings By Interference of Two-photon transitions (RABBIT) is used to study (i) photonionization time delays across the 4d giant dipole resonance in xenon, (ii) resonant below-threshold two-photon ionization of the 1s3p, 1s4p and 1s5p Rydberg states in helium and (iii) autoionization dynamics from the $3s^1 3p^6 4p$ Fano resonance in argon. Secondly, to fully characterize mixed photoelectron quantum states, a quantum state tomography protocol for photoelectrons (KRAKEN) is developed theoretically and tested experimentally for non-resonant photoionization of helium and argon.

Populärvetenskaplig Sammanfattning

Ljus som ett verktyg för att mäta ultrakorta tidsskalor

För att mäta längden på ett objekt behöver du en linjal med en skala som är mindre än objektet du vill mäta. För att fånga ett händelseförlopp behöver du på ett liknande sätt en tidsskala som är kortare än händelsen. I till exempel en kamera bestäms denna tidsskala av den kortaste tid som du samlar in ljus, det vill säga den kortaste ljuspuls som du belyser objektet med. När man studerar objekt med mindre storlek så sker vanligtvis dess rörelse på en allt kortare tidsskala. Exempelvis tar det 1 sekund $= 10^0$ sekund för ett hjärta att slå ett slag, och 1 millisekund $= 0.001$ sekund $= 10^{-3}$ sekund för ett bi att slå ett vingslag. Dessa tidsskalor kan uppfattas av människans öga eller en vanlig kamera. För att uppfatta elektroners rörelse krävs dock extremt korta ljuspulser. I Niels Bohrs berömda atommodell tar det endast 150 attosekunder för en elektron i en väteatom att kretsa kring atomkärnan. En attosekund är en miljarddels miljarddel av en sekund (1 attosekund $= 10^{-18}$ sekund). I den här doktorsavhandlingen presenteras en modell för hur man på ett effektivt sätt kan producera ljuspulser på attosekundstidsskalan. Attosekundspulserna används för att studera hur elektroner beter sig i olika atomer på attosekundsskalan.

Allt ljus runtomkring oss består av elektromagnetisk strålning med olika våglängder. Vi uppfattar de olika våglängderna som olika färger, där rött ljus har en längre våglängd än blått ljus. Alla elektromagnetiska vågor är dock inte synliga för oss människor. De flesta våglängder är faktiskt utanför det synliga spektrat, vilket visas i Fig. 1. För varje våglängd av ljus är den kortaste ljuspulsen som kan skapas begränsad av hur lång en våglängd är, samt vågens hastighet – den konstanta ljushastigheten. För en våglängd på 800 nanometer är den här gränsen 2700 attosekunder, medan för ultraviolett ljus med 30 nanometer vågländ, är gränsen 100 attosekunder. Det är tydligt att man därför vill ha kortare våglängder för att studera snabba händelseförlopp. Lasrar som producerar ljus med korta våglängder, i det ultravioletta spektralområdet, är dessvärre inte tillgängliga. Däremot finns det en process som kallas *övertonsgenerering* som kan användas istället.

Du kanske känner till övertoner, eller harmonier, från musikinstrument där det helt enkelt är en frekvsen som är en multipel av en grundfrekvens. Uttryckt i våglängder, om grundfrekvensen har våglängden L, så har den tredje övertonen våglängden $L/3$. När du spelar på en sträng på till exempel en violin så vibrerar strängen med en viss frekvens. Strängen vibrerar dock inte bara med grundfrekvensen, utan även med flera andra övertonsfrekvenser samtidigt. På samma sätt kan ljus med korta våglängder genereras som övertoner av en lång våglängd. Detta kan åstadkommas genom att fokusera en laserpuls i en liten punkt i en gas. Gasen i det här fallet agerar som strängen på violinen, och laserpulsen är stråken.

I båda fallen ovan beror styrkan hos övertonen på hur mycket kraft man tillför strängen

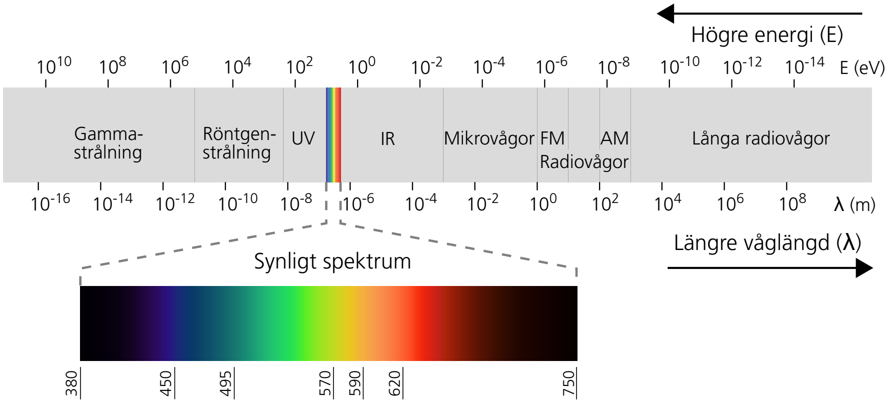

Figure 1: Elektromagnetiska spektrumet. [Adapted from Philip Ronan, Gringer under CC-BY-SA-3.0]

(eller gasen), men typiskt minskar styrkan väldigt snabbt för högre övertoner. Genom att tillföra mer kraft, det vill säga använda en starkare laserpuls, kan man öka styrkan på övertonen. Däremot är effektiviteten, hur stark överton du får ut relativt till hur mycket kraft du tillför, densamma. När man genererar höga övertoner i gaser så kan en *bra* effektivitet vara så låg som 0.001%, och mycket arbete har lagts ner på att öka effektiviteten. En del av min avhandling har fokuserat på det här problemet. Vi har utvecklat en modell baserad på datorsimuleringar, och verifierad genom experimentella mätningar, som säger hur gasmediet ska utformas för att generera attosekundspulser med hög effektivitet.

De korta våglängderna som fås då höga övertoner genereras kan användas för att studera hur elektroner beter sig i atomer. Ljus som har en kort våglängd är mer energirikt, vilket visas i Fig. 1. Då ljuspartiklar, *fotoner*, med tillräckligt hög energi kolliderar med en atom kan de knuffa ut en elektron i en process som kallas den fotoelektriska effekten, eller *fotojonisering*. Då detta händer kommer de andra elektronerna i atomen att omfördela sig mycket snabbt, på attosekundstidskalan. Den joniserande elektronen fortsätter att känna av de andra elektronernas rörelse samtidigt som den lämnar atomen. Genom att studera den joniserande elektronen kan man därför få viss information om omfördelningen av de andra elektronerna. I den andra delen av min avhandling har vi studerat fotojonisering från olika atomer med en tidsupplösning på attosekundsskalan. Den här typen av fundamental forskning kan förbättra vår förståelse för, och modeller av, naturens mest grundläggande byggstenar. Att förstå hur elektroner *beter sig* i atomer och molekyler är det första steget för att lära sig *kontrollera* deras rörelse. Ett långsiktigt mål inom fältet attosekundsforskning är att kunna kontrollera elektroners rörelse i kemiska reaktioner på deras naturliga tidsskalor.

Popular Science Summary

Light as a tool for measuring ultrashort timescales

To measure the length of an object, you need a ruler with a scale smaller than the object of interest. In a similar way, to capture the evolution in time of some event, you need to use light flashes which are shorter than the event itself. When the weight of an object gets smaller and smaller, its motion typically occurs on shorter and shorter timescales. For example the human heartbeat is roughly $1\,\text{second} = 10^0\,\text{second}$, and the wing flap of a bee is around $1\,\text{millisecond} = 0.001\,\text{second} = 10^{-3}\,\text{second}$. These timescales can be captured by the human eye, or a normal camera. Recording electron motion on its natural timescale, however, requires extremely short pulses of light. In Niels Bohr's famous atomic model, the electron in a hydrogen atom orbits the nucleus in a mere 150 attoseconds, where one attosecond is a billionth of a billionth of a second ($1\,\text{as} = 10^{-18}\,\text{s}$). In this thesis, a model is developed describing how to efficiently produce light pulses on the attosecond timescale. The attosecond pulses are applied to study, with attosecond time resolution, the behavior of electrons in different atoms.

All light around us consists of electromagnetic radiation of different wavelengths, which we perceive as different colors, with red light having a longer wavelength than blue light. However not all electromagnetic waves are visible to us. In fact, most wavelengths lie outside the visible spectrum, as shown in Fig. 2. For any color of light, the shortest pulse duration is limited by the length of a single wavelength, and the speed of the wave – the constant speed of light. For a wavelength of 800 nanometer this limit is 2700 attoseconds, while for extreme ultraviolet light of 30 nanometer wavelength the limit is 100 attoseconds. Clearly, one would like short wavelength light to study fast events. Lasers producing wavelengths in the extreme ultraviolet region of the spectrum are unfortunately not readily available. Luckily, a process known as *harmonic generation* can be used instead.

You might know harmonics, or overtones, from musical instruments, where it is simply a frequency multiple of some fundamental frequency. Expressed in wavelengths, if the fundamental wavelength is of length L, then the third harmonic has a wavelength of $L/3$, and so on. When playing the string on, for example, a viola, you are not only making the string vibrate at the fundamental frequency. Rather, it vibrates at a range of harmonic frequencies simultaneously. In the same way, light of very short wavelengths can be produced as harmonics of a longer wavelength. This can be done by focusing a laser pulse into a small volume in a gas. Here, the gas acts as the string on the viola, and the laser pulse is the bow.

In both cases, the strength of the harmonics depends on the force applied to the string (or gas), but typically it falls off rapidly as the harmonic order increases. Applying more force, *i.e.* a stronger laser pulse, increases the strength of the harmonic, but the efficiency, the ratio

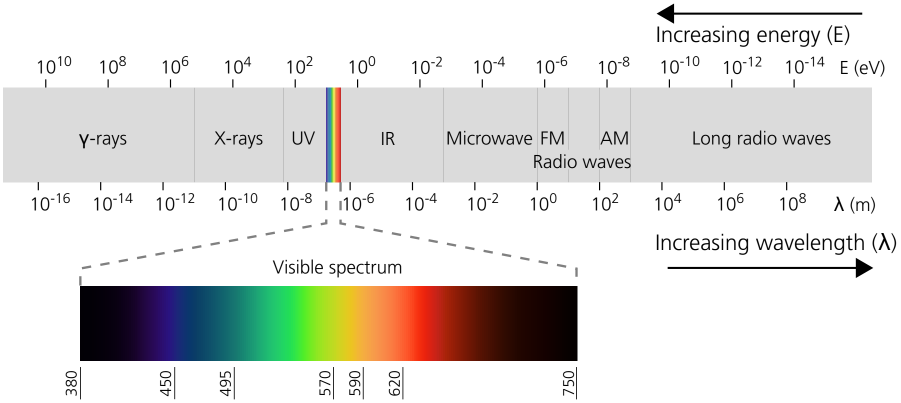

Figure 2: Spectrum of electromagnetic radiation. [Adapted from Philip Ronan, Gringer under CC-BY-SA-3.0]

of the energy you put in to what you get out, remains the same. In high-order harmonic generation in gases, a *good* efficiency may be as low as 0.001%, and much effort has been devoted towards increasing it. One part of my thesis work has focused on this aspect. In particular, we have developed a model based on computer simulations, and verified through experimental measurements, which tells how the gas medium should be designed to obtain a high efficiency.

The short wavelength light obtained through high-order harmonic generation can be used to study electron behavior in atoms. As shown in Fig. 2, a short wavelength corresponds to high energy light. When particles of light, *photons*, with high enough energy collide with an atom, they may kick out an electron in a process called the photoelectric effect, or *photoionization*. When this happens, the remaining electrons rearrange themselves inside the atom on the attosecond time scale. As it is ejected from the atom, the ionizing electron continues to interact with the remaining electrons. The electron motion inside the atom taking place on the attosecond timescale can be inferred from the imprint that this interaction leaves on the ionizing electron. In the second part of my thesis work, we have performed studies of such photoionization events in different atomic species. This type of fundamental research aims at improving our understanding and models of natures most basic building blocks. Understanding how electrons *behave* in atoms and molecules is the first step towards learning how to *control* their motion, and one long-term goal of the attosecond research community is to be able to reliably control electron motion in chemical reactions on their natural timescale.

List of Publications

This thesis is based on the following publications, referred to by their Roman numerals:

I **How to optimize high-order harmonic generation in gases**

R. Weissenbilder, S. Carlström, L. Rego, C. Guo, C. M. Heyl, P. Smorenburg, E. Constant, C. L. Arnold, A. L'Huillier
Nature Reviews Physics **4** 713–722, (2022)

II **The two phase-matching regimes in high-order harmonic generation**

E. Appi, **R. Weissenbilder**, B. Nagyillés, Z. Diveki, J. Peschel, B. Farkas, M. Plach, F. Vismarra, V. Poulain, N. Weber, C. L. Arnold, K. Varjú, S. Kahaly, P. Eng-Johnsson, A. L'Huillier
Optics Express **31** 19 (2023)

III **Ultrastable, high-repetition-rate attosecond beamline for time-resolved XUV-IR coincidence spectroscopy**

D. Ertel, M. Schmoll, S. Kellerer, A. Jäger, **R. Weissenbilder**, M. Moioli, H. Ahmadi, D. Busto, I. Makos, F. Frassetto, L. Poletto, C. D. Schröter, T. Pfeifer, R. Moshammer, G. Sansone
Review of Scientific Instruments **94** 073001 (2023)

IV **Ultra-stable and versatile high-energy resolution setup for attosecond photoelectron spectroscopy**

S. Luo*, **R. Weissenbilder***, H. Laurell, M. Ammitzböll, V. Poulain, D. Busto, L. Neoričić, C. Guo, S. Zhong, D. Kroon, R. J. Squibb, R. Feifel, M. Gisselbrecht, A. L'Huillier, C. L. Arnold
Advances in Physics X **8** 1 (2023)

V **Attosecond electron–spin dynamics in Xe 4d photoionization**

S. Zhong, J. Vinbladh, D. Busto, R. J. Squibb, M. Isinger, L. Neoričić, H. Laurell, **R. Weissenbilder**, C. L. Arnold, R. Feifel, J. M. Dahlström, G. Wendin, M. Gisselbrecht, E. Lindroth, A. L'Huillier
Nature Communications **11** 5042, (2020)

VI **Resonant two-photon ionization of helium atoms studied by attosecond interferometry**
L. Neoričić*, D. Busto*, H. Laurell, **R. Weissenbilder**, M. Ammitzböll, S. Luo, J. Peschel, H. Wikmark, J. Lahl, S. Maclot, R. J. Squibb, S. Zhong, P. Eng-Johnsson, C. L. Arnold, R. Feifel, M. Gisselbrecht, E. Lindroth, A. L'Huillier
Frontiers in Physics **05**, (2022)

VII **The influence of final state interactions in photoelectron interferometric measurements of Fano resonances**
S. Luo, **R. Weissenbilder**, H. Laurell, R. Y. Bello Romero, C. Marante, M. Ammitzböll, L. Neoričić, A. Ljungdahl, R. J. Squibb, R. Feifel, M. Gisselbrecht, C. L. Arnold, F. Martín, E. Lindroth, L. Argenti, D. Busto, A. L'Huillier
(In manuscript)

VIII **Continuous-variable quantum state tomography of photoelectrons**

H. Laurell, D. Finkelstein-Shapiro, C. Dittel, C. Guo, R. Demjaha, M. Ammitzböll, **R. Weissenbilder**, L. Neoričić, S. Luo, M. Gisselbrecht, C. L. Arnold, A. Buchleitner, T. Pullerits, A. L'Huillier, D. Busto
Physical Review Research **4** 033220, (2022)

IX **Measuring the quantum state of photoelectrons**

H. Laurell*, S. Luo*, **R. Weissenbilder**, M. Ammitzböll, H. Söderberg, S. Ahmed, C. L. M. Petersson, V. Poulain, C. Guo, C. Dittel, D. Finkelstein-Shapiro, R. J. Squibb, R. Feifel, M. Gisselbrecht, C. L. Arnold, A. Buchleitner, E. Lindroth, A. Kockum, A. L'Huillier, D. Busto
(Submitted)

All papers are reproduced with permission of their respective publishers.

Related publication by the author, not included in this thesis:

A high-repetition rate attosecond light source for time-resolved coincidence spectroscopy
S. Mikaelsson, J. Vogelsang, C. Guo, I. Sytcevich, A-L. Viotti, F. Langer, Y-C. Cheng, S. Nandi, W. Jin, A. Olofsson, **R. Weissenbilder**, J. Mauritsson, A. L'Huillier, M. Gisselbrecht, C. L. Arnold
Nanophotonics **10** 117-128 (2021)

Abbreviations

1/2/3D	One/Two/Three Dimensional
ADK	Ammosov-Delone-Krainov
AOPDF	Acousto-Optical Programmable Dispersive Filter
APT	Attosecond Pulse Train
ATI	Above-Threshold Ionization
CAMP	Chamber for Atomic and Molecular Physics
CE	Conversion Efficiency
CEP	Carrier-Envelope Phase
CPA	Chirped Pulse Amplification
CW	Continuous Wave
ELI-ALPS	Extreme Light Infrastructure–Attosecond Light Pulse Source
EWP	Electron Wave Packet
FWHM	Full-Width-at-Half-Maximum
HHG	High-order Harmonic Generation
IAP	Isolated Attosecond Pulse
IR	InfraRed
KRAKEN	quantum state tomography of attosecond electron wave packets
MBES	Magnetic Bottle Electron Spectrometer
MCP	MicroChannel Plate
Nd:YLF	Neodymium-doped Yttrium-Lithium-Flouride
PAD	Photoelectron Angular Distribution
PPT	Perelomov-Popov-Teren'tev
PES	PhotoElectron Spectrum
QST	Quantum State Tomography
RABBIT	Reconstruction of Attosecond Beating By Interference of Two-photon transitions
RMS	Root Mean Square
RPAE	Random Phase Approximation with Exchange
RRPA	Relativistic Random Phase Approximation
SAE	Single Active Electron
SAR	Single Atom Response
SB	SideBand
SFA	Strong Field Approximation
S–O	Spin–Orbit
TBP	Time-Bandwidth Product
TDSE	Time-Dependent Schrödinger Equation
Ti:Sa	Titanium:Sapphire
ToF	Time-of-Flight
TSM	Three-Step Model
VMIS	Velocity Map Imaging Spectrometer
XUV	Extreme UltraViolet

Contents

Part I: Thesis

Chapter I

Introduction

1.1 Photoelectron Spectroscopy

Light has been used to infer the properties of matter since the birth of the field of spectroscopy in the 17th century due to Newton, at a time when neither the structure of matter nor the wave-particle duality of light was known. The first quantum revolution at the turn of the 20th century, including Bohr's atomic model and the explanation of the photoelectric effect by Einstein [1] completely changed the understanding of light-matter interactions, and laid the groundwork for new spectroscopic techniques.

Photoemission spectroscopy, or *photoelectron spectroscopy* of core electrons was pioneered in the 1950s by Kai Siegbahn using X-rays [2]. The principle of photoelectron spectroscopy is simple, and directly related to the photoelectric effect. The binding energy I_p, which provides information about the electronic structure, is related to the difference of the photon energy and the kinetic energy of the ionized electron,

$$I_\mathrm{p} = \hbar\omega - E_\mathrm{kin} \tag{1.1}$$

where $\hbar$ is Planck's reduced constant, ω is the angular frequency of the light, and E_kin is the kinetic energy of the photoelectron.

The light sources used for this type of spectroscopy range from continuous light from the sun or flames, at the time of Newton, to X-ray tubes, discharge flash lamps and high brilliance synchrotrons producing tunable light bursts with pulse durations down to 0.1 to 10 ns [4]. Because of their temporal properties, these sources were used primarily to probe electronic structure, transition amplitudes and transient decays in the nanosecond to microsecond range. Ultrafast time-resolved spectroscopy aims to probe dynamics on much

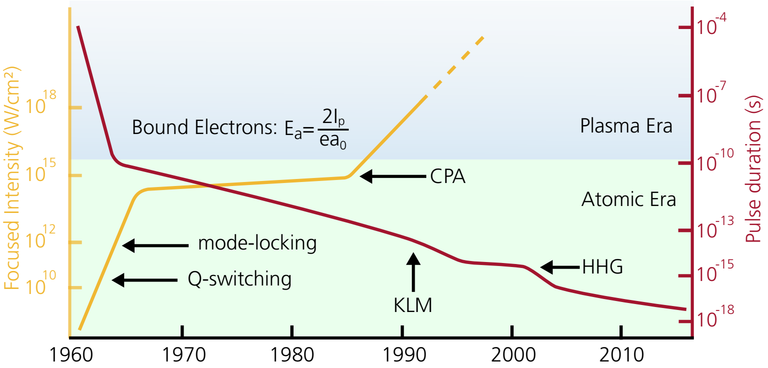

Figure 1.1: History of light pulses. Focused laser intensity (yellow) assuming a beam size on the order of 1 cm^2, and shortest light pulse duration (red). Major milestones leading to increased intensities or shorter pulses are indicated. [Adapted with permission from Ref. [3]].

shorter timescales. Chemical reactions and electron motion occur on the femtosecond (10^{-15} s) and attosecond (10^{-18} s) timescales, which can be understood heuristically from the Heisenberg uncertainty relation

$$\Delta\tau\Delta E \geq \frac{\hbar}{2}, \tag{1.2}$$

where $\Delta\tau$ is a time interval[1], and ΔE is *e.g.* the energy difference between two atomic levels. For atoms, the minimum energy required for ionizing the ground state is in the 3 to 25 eV range, which by the above relation gives $10\,\mathrm{as} \leq \Delta\tau \leq 110\,\mathrm{as}$.

Clearly, shorter pulses are needed to resolve dynamics on this timescale. The first laser built in 1960 by Maiman [6] initiated a rapid development towards shorter optical pulses. A timeline including some major breakthroughs is given in Fig. 1.1. The Q-switching [7], and especially the mode-locking [8] techniques, have been essential to this development. In mode-locking, a broad range of cavity modes are phase-locked, leading to constructive interference of all the frequency components. The average power of the otherwise Continuous Wave (CW) laser is then contained in a short pulse, hence a more or less direct relation between the peak intensity in the pulse and its duration can be seen until the mid 1980s. Due to the high intensities, damage thresholds of gain media hampered further development. The invention of the Chirped Pulse Amplification technique (CPA) [9] (see Sec. 2.1.1), and Kerr-Lens Mode-locking (KLM) [10], has led to intense laser pulses of femtosecond duration.

---

[1] A more rigorous interpretation consistent with quantum mechanics is the Mandelstam-Tamm uncertainty relation [5], where $\Delta\tau$ should be understood as the shortest time interval during which the expectation value of an observable changes by its standard deviation.

1.2 Ultrafast Spectroscopy

Femtosecond pulses were the catalyst for the field of femtochemistry, beginning with a 1988 paper by Ahmed Zewail [11], where chemical reactions, *e.g.* chemical bond breaking, was studied on their natural timescale. The attosecond pulses needed to resolve electron dynamics in atoms are, however, unobtainable with conventional lasers due to the limit imposed by the single-cycle duration of the available laser wavelengths. Indeed, a femtosecond plateau can be seen in Fig. 1.1 during the 1990's. In parallel with the application of femtosecond pulses to probe molecular dynamics, the peak electric field amplitudes obtained with CPA based lasers reached the level of the Coulomb potential of bound electrons in atoms, opening up the door to many new nonlinear optical phenomena. High order-Harmonic Generation (HHG), which was discovered by strongly focusing picosecond laser pulses in gases and plasmas [12–14], greatly benefited from CPA, and it was subsequently demonstrated that this process generated trains of attosecond pulses [15].

Because electronic devices are not fast enough to directly capture the attosecond electron dynamics, measurements of processes occurring below the picosecond timescale are commonly performed using two-photon *pump-probe spectroscopy*. In this thesis, one such technique called Reconstruction of Attosecond Beatings By Interference of Two-photon transitions (RABBIT) is utilized [15]. The Extreme UltraViolet (XUV) radiation of the Attosecond Pulse Train (APT) initiates the dynamics, acting as the pump, and an InfraRed (IR) femtosecond pulse with a variable delay probes the system at different times. Initially the technique was used to characterize the APT itself, however, knowing the structure of the APT, the RABBIT technique has been utilized to measure the spectral amplitude and phase of Electron Wave Packets (EWPs) photoionized from atoms [16–19], molecules [20] and solids [21]. In contrast to synchrotron experiments, where the spectral amplitude is measured, the additional access to spectral phase information provides information about the temporal dynamics of the photoionization process [16, 22].

1.3 Quantum Coherence in Attosecond Science

In the past few decades, quantum technologies have attracted a lot of interest, marking the start of a second quantum revolution [23, 24]. For any technological application of a quantum system, the quantum coherence, a measure of the "quantumness" of the system, is vital. The interest in coherence has also reached the field of attosecond science [25], where loss of coherence may occur due to incomplete measurements of entangled states, or due to coupling to environmental degrees of freedom. In contrast to the previously described RABBIT measurements, which assume a wave function formalism, the characterization of a quantum state requires the measurement of its full density matrix. New methods have been developed in attosecond science to this end. A quantum state tomography (QST) protocol has been applied to the reconstruction of the density matrix of a photoelectron ionized by an APT [26]. Using an APT and a time-delayed IR probe, control of the degree of entanglement between an H_2^+ ion and photoelectron, and as a consequence the vibrational coherences in the ion, has been studied [27].

1.4 Introduction to High-order Harmonic Generation

From the previous discussion, it should be clear that the light source is often the enabling technology for time-resolved spectroscopic techniques. At the heart of attosecond science is the HHG process[2], which provides a table-top source of spatially and temporally coherent, broadband XUV radiation. However, HHG is by nature a highly inefficient process, which sets limits on the experiments that can be performed.

Depending on the experiment, two complementary scaling directions can be taken [29]. (i) Loose focusing of high pulse energy, low repetition rate driving lasers are used when generating harmonics to explore phenomena which depend nonlinearly on the XUV intensity [30]. (ii) High repetition rates and consequently low pulse energies, requiring tight focusing, is beneficial to improve statistics in experiments where *e.g.* multiple ionization fragments are detected in coincidence [31, 32]. In both cases, the efficiency of the HHG process is key to enable novel experiments to be performed.

Recently, scaling laws for HHG were described by Heyl *et al.* [33], demonstrating that the propagation equation in the generating medium is invariant under changing focusing conditions if the pulse energy of the driving field and the length and density of the gas medium are scaled appropriately. The scaling laws furthermore show that the same Conversion Efficiency (CE) can be achieved in vastly different focusing conditions [34], which explains the successful application of HHG in both the loose and tight focusing schemes described above.

1.5 Motivation

This thesis aims to further improve our knowledge in two directions:

(i) Optimization of the conversion efficiency in HHG. In particular, the scaling laws described above do not make any claims about *how* the focusing geometry and generating medium should be chosen for the efficiency to be optimized. In the literature, the charac-

---

[2] Free Electron Lasers (FELs) also produce ultrashort x-ray pulses for the study of ultrafast dynamics. The pulse duration has been pushed down to attoseconds at LCLS [28].

teristics of the generating medium can vary strongly while still achieving similar efficiencies, even for similar driving field parameters and focusing conditions. In this thesis, we develop a general, scaling invariant model predicting the laser focusing geometry and medium density and length that should be used for optimal CE, given a driving pulse energy and duration. The model suggests that a high CE can be achieved in a large range of gas densities and medium lengths given that these follow a hyperbolic relation. This conclusion is also verified by experimental results.

(ii) High spectral resolution attosecond interferometry of photoelectrons. Motivated by challenges posed by measurements in xenon, carried out at the start of this thesis, in spectrally congested regions and with low statistics, we upgraded the laser repetition rate and built a new setup with improved resolution and temporal stability, which also offers more flexibility in two-pulse pump-probe schemes. With the improved capabilities of the setup, we uncover new information in high-resolution RABBIT measurements. We also move towards complete characterization of mixed quantum states by developing a QST protocol for photoelectrons called KRAKEN[3] (quantum state tomography of attosecond electron wavepackets). The protocol is verified by measuring the density matrix of photoelectrons ionized by APTs in argon and helium.

1.6 Papers and Outline

This thesis is based on 9 papers, which can broadly be partitioned into two categories, (i) optimization of high-order harmonic generation and (ii) attosecond photoionization studies in noble gases using pump-probe photoelectron spectroscopy.

In papers **I** and **II** we study optimal conditions for high-order harmonic generation in gases theoretically and experimentally. A simple, scalable, analytic model is developed, predicting that efficient phase-matching of high-order harmonic generation in gases is possible over a wide range of pressures and medium lengths if these follow a certain hyperbolic relationship. The model is validated using numerical simulations, and shown to be, to a large degree, independent of focusing geometry, driving pulse duration, intensity, harmonic order and atomic species. Experimental measurements performed at ELI-ALPS (Extreme Light Infrastructure-Attosecond Light Pulse Source) Szeged, Hungary, further verify the hyperbolic relationship maximizing the conversion efficiency. In paper **III** a collinear pump-probe delay line for photoelectron-photoion coincidence spectroscopy is implemented and characterized in the group of Giuseppe Sansone at the University of Freiburg. The divergence of harmonic radiation generated in gas jets and gas cells is explored and compared to simulations performed in Lund.

---

[3] The acronym comes from the Swedish "KvanttillståndstomogRafi av AttoseKundElektroNvågpaket".

In paper **IV** we describe an ultra-stable and versatile Mach-Zehnder interferometer for attosecond pump-probe photoelectron interferometry. The interferometer is actively stabilized directly to the phase relation of the pump and probe femtosecond laser pulses, which allows us to implement separate spectral shapers in both the pump and probe beams, and to easily switch between the RABBIT and KRAKEN schemes.

In paper **V** we study photoionization time delays from the xenon 4d shell in the 70 to 100 eV range. Combining coincidence spectroscopy and attosecond interferometry using the RABBIT technique allows us to disentangle the different ionization channels. By performing time-frequency analysis, we identify the interference of two ionization mechanisms: a broad giant dipole resonance, and a narrow resonance close to threshold exhibiting spin-flip dynamics.

In papers **VI** and **VII** we study resonant photoionization using the RABBIT technique in helium and argon. In particular, we study angle-resolved and high resolution angle-integrated photoionization from the helium 3p, 4p, 5p Rydberg series. With the help of theoretical calculations we explain the observed phase jumps both as a function of angle and photoelectron energy. In argon we study the $3s^1 3p^6 4p$ Fano resonance with ultra-high energy resolution, resolving the spin–orbit split components. We explore the effects of coupling of the two-photon ionization to resonances in the final continuum.

In paper **VIII** we develop a new protocol for continuous variable quantum state tomography of pure and mixed photoelectron states, called KRAKEN. A bichromatic infrared probe pulse consisting of two narrowband components spaced by a variable frequency is used to interfere different spectral parts of a photoelectron wave packet, ionized by an XUV harmonic. By varying the delay between XUV and IR, and the bichromatic probe frequency difference, both amplitude and phase of the density matrix are extracted. In paper **IX** we experimentally verify the KRAKEN protocol for pure photoelectron states in helium, and mixed states in argon.

The topics above are all connected through basic underlying principles, in particular through interference of waves, be it light- or matter-waves, with well defined phase relations. The following chapters of this thesis attempts to demonstrate precisely these relations. The thesis structured as follows: Chapter 2 gives an introduction to femtosecond laser pulse generation and their application to attosecond pulse generation through the process of high-order harmonic generation, in the single atom picture. Chapter 3 introduces the most important macroscopic concepts in high-order harmonic generation, and discussed how to optimize the conversion efficiency taking both microscopic and macroscopic concepts into consideration. Chapter 4 deals with the theory of attosecond pulse trains applied to photoelectron spectroscopy, using the RABBIT and KRAKEN techniques, and the experimental methods used. Chapter 5 presents the main experimental results of the photoionization studies. We conclude in Chapter 6 with a summary and an outlook.

Chapter 2

Introduction to Attosecond Pulse Generation

The experimental studies of attosecond photoionization dynamics in this thesis rely on the controlled, efficient generation of XUV attosecond pulses. The generation of these attosecond pulses is a highly nonlinear process, driven by the interaction of intense femtosecond laser pulses with matter. Efficient generation of attosecond pulses depends, in general, on two things, (i) the nonlinear response of a single atom to an intense laser field and (ii) the degree of coherence of the simultaneous emission of many atoms in the generating medium. This chapter introduces the relevant methods of producing intense femtosecond laser pulses, and the single atom aspects of attosecond pulse generation.

2.1 Femtosecond Pulses

An optical pulse can in general be described by its complex representation

$$\tilde{\mathcal{E}}(t) = |\mathcal{E}(t)| \exp\left[\mathrm{i}(\omega_0 t + \phi(t))\right], \tag{2.1}$$

where ω_0 is the carrier frequency and $\phi(t)$ is the temporal phase. $\mathrm{Re}\{\tilde{\mathcal{E}}(t)\}$ is the real valued electric field, and $|\mathcal{E}(t)|$ is the amplitude of the complex envelope. Here, and in the following, a $\sim$ will be used to indicate any rapidly oscillating function.

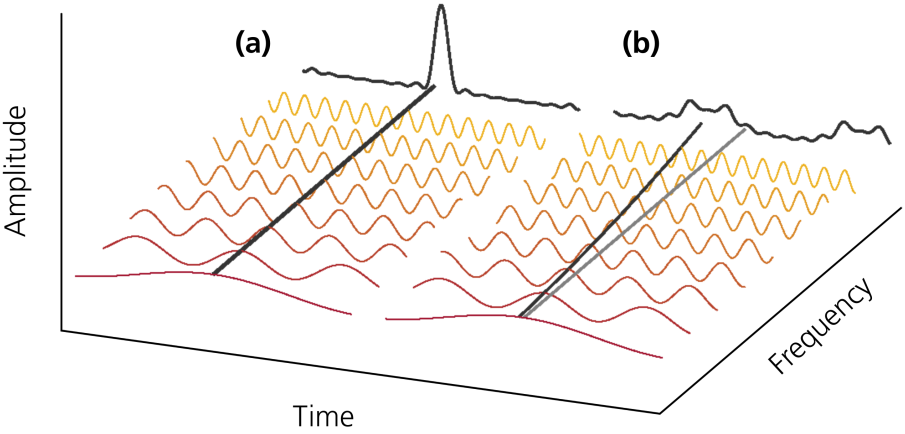

Figure 2.1: Principle of wave interference. Waves of low frequency are shown in red, and higher frequencies in yellow. The black curve shows the resulting intensity of the sum of all waves. (a) All frequencies are in phase, indicated by the straight black line, such that the maxima coincide in time. (b) A quadratic chirp is present, indicated by the black line. Different frequencies have maxima off-set in time with respect to each other, leading to partial destructive interference, and a less intense and longer pulse. The gray line indicates the phase in (a) for reference.

$\tilde{\mathcal{E}}(t)$ is related to its spectral counterpart through a Fourier transform,

$$\tilde{E}(\omega) = \frac{1}{\sqrt{2\pi}} \int_{-\infty}^{\infty} \mathrm{d}t\, \tilde{\mathcal{E}}(t) \exp\left[-\mathrm{i}\omega t\right] = |E(\omega)| \exp\left[\mathrm{i}\Phi(\omega)\right], \tag{2.2}$$

where $\Phi(\omega)$ is the spectral phase, and $|E(\omega)|^2$ is the spectral intensity.

The Heisenberg-Gabor limit states that a function and its Fourier transform cannot both have finite domains. More generally, it means that there is an inverse relationship between the duration of a pulse and its spectral width. This relation is succinctly summarized by the Time-Bandwidth Product (TBP)

$$\Delta\tau\Delta\nu \geq \Gamma_{\mathrm{TBP}}, \tag{2.3}$$

where $\Delta\tau$ and $\Delta\nu$ are the Full-Width at Half-Maximum (FWHM) of the temporal and spectral intensities ($\nu = \omega/2\pi$), respectively, and Γ_{TBP}, is a factor determined by the pulse envelope. For Gaussian pulses it is given by $\Gamma_{\mathrm{TBP}}, = 2\ln 2/\pi \approx 0.44$.

Ultrashort optical pulses, on the femtosecond timescale, thus require a spectrum which is very broad. The reverse is however not necessarily true, as a broad spectrum may still lead to a long pulse in time due to variations of the temporal phase $\phi(t)$. The influence of the temporal phase is illustrated in Fig. 2.1. To the left, the phase difference between consecutive frequency components is constant, which results in a linear temporal phase, and peak amplitudes of all frequency components coinciding at some time t. All frequency components constructively interfere, leading to a Fourier transform limited pulse of duration $\Delta\tau = \Gamma_{\text{TBP}}/\Delta\nu$.

A relative phase difference of any higher order will result in a change over time of the instantaneous angular frequency, defined as

$$\omega(t) = \omega_0 + \frac{\partial\phi(t)}{\partial t}. \tag{2.4}$$

The case where $\phi(t) \propto t^2$ is shown on the right in Fig. 2.1. It leads to an angular frequency with a linear time dependence, $\omega(t) \propto \omega_0 + bt$, such that the peak amplitude of different frequencies arrive at different times and the result is a pulse which is chirped. Here, the chirp parameter is $b = \frac{\partial^2\phi}{\partial t^2}$.

2.1.1 Chirped Pulse Amplification

As discussed in the introduction, mode-locked laser oscillators with broadband gain media supporting femtosecond pulses are commercially available. However, the pulse energies are relatively low, which becomes a limitation for applications in extreme, nonlinear light-matter interaction. To increase the pulse energy, amplification is performed through stimulated emission in a population inverted gain medium. Direct amplification of these femtosecond pulses tends to be unsuitable, as the peak intensity of the amplified pulse will quickly lead to unwanted nonlinear effects or optical damage in the gain medium. Simply expanding the involved beams and optics also quickly becomes untenable. Instead, the solution is to use the 4th dimension, stretching the pulse in time by using the concept of chirp discussed in the previous section.

To increase the duration and hence reduce the peak intensity during amplification, the pulse is chirped intentionally in a technique referred to as chirped pulse amplification. This technique was developed by Donna Strickland and Gérard Mourou in 1985 [9], who subsequently were awarded the 2018 Nobel prize in physics for their work. The principle is sketched in Fig. 2.2, where in the first step, an oscillator producing a femtosecond laser pulse is sent into a stretcher. While in the original 1985 paper a 1.4 km fiber was used for stretching[1], here, the most common method using a pair of gratings is shown. Due to technical reasons related to the recompressability, the choice is usually a positive dispersion

---

[1] In combination with a grating compressor, it achieved a 100-fold increase in peak power, but produced unwanted pre- and post-pulses after compression.

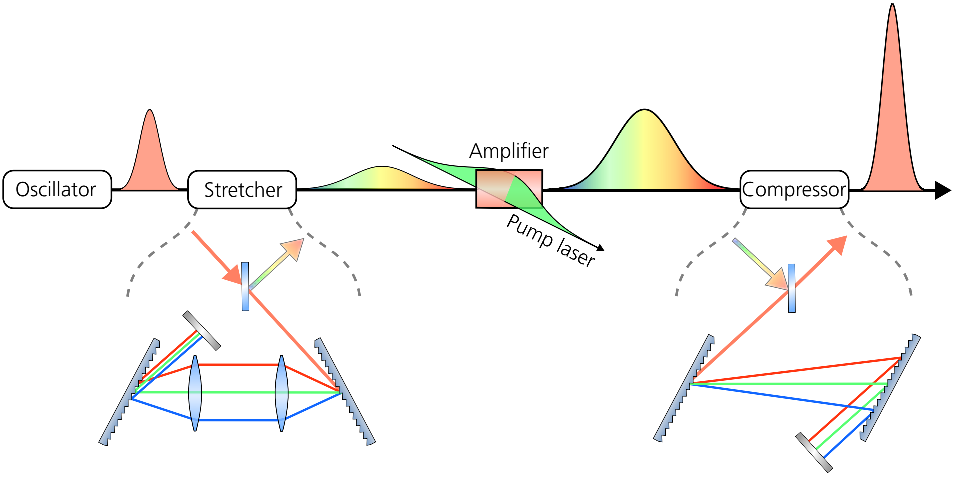

Figure 2.2: Principle of chirped pulse amplification. In the first step, the pulse is chirped in the stretcher. Shorter wavelengths present in the broadband pulse travel a longer distance inside the stretcher, here in a Martinez configuration [35]. The resulting pulse has a much lower peak intensity. In the next step, the chirped pulse is amplified. After the amplifier the pulses are still long, but with a much higher pulse energy. The final step is temporally compressing the pulse, shown here in the Treacy configuration [36]. The output is an ultrashort, high energy pulse.

configuration, which requires the use of additional imaging optics, here in the form of a pair of lenses [35][2]. Depending on the desired amplification, the pulse is stretched from femtoseconds to picoseconds. After the pulse has been chirped, it is amplified by overlapping it in time and space with a pump laser pulse in a gain medium. Finally, the pulse is recompressed by compensating for the positive dispersion of the stretcher. The compressor in Fig. 2.2 is again shown using two gratings, but in a negative dispersion configuration. The output is a femtosecond pulse with high pulse energy.

2.1.2 Nonlinear Response of Matter to Electromagnetic Fields

The response of a dielectric medium to an external electric field is described by the density of induced dipole moment in the medium, or polarization, $\tilde{\mathcal{P}}(t)$. The field of nonlinear optics concerns the nonlinear polarization response of an optical medium in the presence of an external optical field. In the nonlinear regime, the optical properties of the medium are modified as a function of the applied field strength, and may in turn change the behavior of the driving field itself.

---

[2] See Ref. [3] for a detailed review.

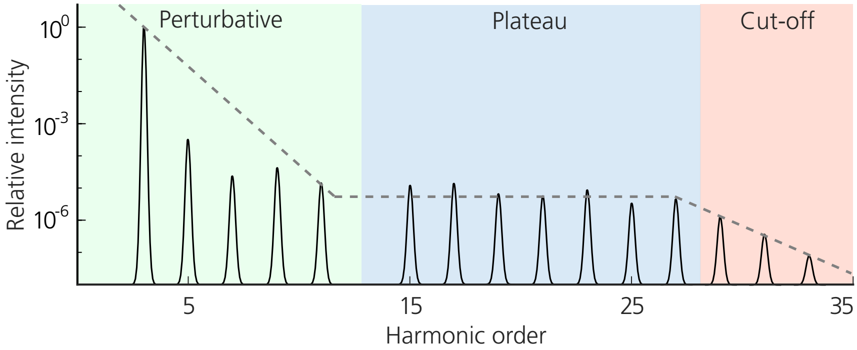

Figure 2.3: Sketch of relative intensity of optical harmonics. Based on data from one of the first experimental verifications of high-order harmonics by Ferray *et al.* [14], generated with a 1064 nm Nd:YAG laser in argon. Three regimes are indicated: the perturbative below threshold regime, the high-harmonic plateau, and the high-harmonic cut-off region. The 13th harmonic is missing due to a high cross section of 5d photoexcitation at 81.9 nm, leading to reabsorption of the harmonic radiation in the medium.

Some nonlinearities due to high intensity light had been observed already in the 1940s [37], but with the demonstration of the first laser by Maiman in 1960 [6], a light source capable of reaching the field amplitudes required for a plethora of new nonlinear effects became available. Already one year later, in 1961, Franken *et al.* showed the existence of optical second harmonic generation in solids [38], after which the discovery of many other nonlinear optical phenomena followed in quick succession.

To describe the nonlinear polarization response, the polarization is in general expanded in Taylor series in the external electric field strength as [39]

$$\tilde{\mathcal{P}}(t)\epsilon_0^{-1} = \underbrace{\chi^{(1)}\tilde{\mathcal{E}}(t)}_{\text{Linear}} + \underbrace{\chi^{(2)}\tilde{\mathcal{E}}(t)^2 + \chi^{(3)}\tilde{\mathcal{E}}(t)^3 + \ldots}_{\text{Nonlinear}}, \tag{2.5}$$

where $\chi^{(q)}$ is the q^{th} order susceptibility and ϵ_0 is the vacuum permittivity. The electric field is assumed to be linearly polarized so that all quantities are scalar quantities. It is important to note that the above expansion assumes that the external electric field can be treated as a perturbation to any internal fields of the medium.

As the driving field is varying in time, so will the induced dipole density. From this consideration, it is easy to see that the q^{th} order nonlinearity generates a field oscillating at frequency $q\omega$

$$\tilde{\mathcal{E}}(t)^q \propto \exp\left[\mathrm{i}\omega t\right]^q = \exp\left[\mathrm{i}q\omega t\right]. \tag{2.6}$$

These harmonics, when the Taylor expansion in Eq. (2.5) is valid, are expected to decrease exponentially in strength as the order q increases.

As laser technology improved, the intensities reached in the medium also increased drastically. When generating high-order harmonics from intense laser interaction with noble gases [13, 14], high density plasmas [12], solids [40] and liquids [41], the relative harmonic intensity is not well described by the perturbative expansion in Eq. (2.5). Rather than an exponential decrease in harmonic intensity as a function of harmonic order, a plateau of many high-order harmonics, of nearly equal intensity, is observed. Fig. 2.3 shows a sketch of the perturbative regime, plateau and return to exponentially decreasing harmonic intensity in what is called the *cut-off* regime [see Sec. 2.2.1].

For the extremely high intensities in these experiments, the perturbative Taylor series expansion no longer necessarily converges, since the laser field strength may reach or even greatly exceed the strength of the internal fields of the material. For the ground state in hydrogen this corresponds to approximately[3] $5 \times 10^{11}\ \mathrm{V\,m^{-1}}$ or an intensity of $3.5 \times 10^{16}\ \mathrm{W\,cm^{-2}}$. Non-perturbative models are required to treat the light-matter interaction at these intensities.

2.2 Attosecond Pulses

A simple semiclassical model by Kulander *et al.* [42] and Corkum [43] was developed soon after the discovery of high-order harmonics. While semiclassical, the model could, among other things, explain not only the existence of the plateau but also reproduce the position of the transition to the cut-off regime discovered by Krause *et al.* using numerically calculations [44]. A range of quantum mechanical descriptions were also developed in the early 90s [45, 46]. The semiclassical model, also known as the simple man's model or, as it will be referred to here, the Three Step Model (TSM), remains a surprisingly powerful tool to gain insight into the HHG process. As the name suggests, the model is based on three steps, which are outlined below.

2.2.1 Three Step Model

In step (i) of the TSM, the combined potential of the atom and the interaction with a strong, low frequency electric field leads to the formation of a potential barrier during the peak of the electric field. An electron may then partially tunnel ionize through the barrier, as sketched in Fig. 2.4(a). The TSM does not provide any details on the tunnel ionization probability itself, but considering the electron as a wave function rather than a classical particle, some further insight can be gained. The probability of tunnel ionization is directly linked to the width of the barrier, inside which the wave solution has an exponentially

---

[3] Based on the ratio of the ionization potential and the Bohr radius.

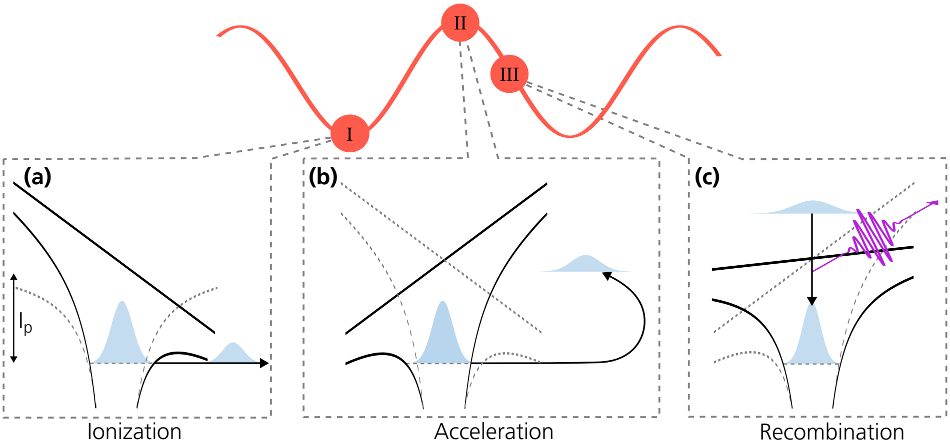

Figure 2.4: Sketch of the semiclassical three step model. (a) Step I occurs every half cycle at the peak amplitude of a strong, low frequency, laser field (red). The atomic potential is maximally bent by the presence of the external field. The effective potential (black solid line) exhibits a potential barrier, through which the electron (blue) can tunnel ionize. (b) In step II the electron is accelerated away from, and then back towards, the parent ion, while gaining kinetic energy and spreading spatially. (c) In step III the electron has a chance to recombine with the parent ion, emitting a high energy photon (purple).

decaying form. Thus, stronger fields, or lower ionization potentials, increase the rate of electrons released in this step.

In step (ii), the electron is accelerated in the presence of the laser field, shown in Fig. 2.4(b). The dynamics are well described by the classical Newton's equations of motion for a charged particle in a time-varying electric field if the interaction with the parent ion is assumed to be weak. The electron is accelerated away from the ion, and as the laser field changes sign, back towards the ion. Again, considering the electron as a wave packet, as it propagates in the presence of the laser field, it also diffuses in space. A longer driving wavelength (*i.e.*, longer cycle length) results in a wave packet which diffuses more before returning.

Finally, in step (iii) shown in Fig. 2.4(c), when the electric field has changed sign and pushed the electron back towards the parent ion, the electron wave packet interferes with the part remaining in the ground state of the atom [47, 48]. This rapid interference results in a dipole oscillation at a frequency corresponding to the difference in energy of the bound and continuum state, emitting light of very high frequency in the process. The diffusion in step (ii) limits the wave function overlap in step (iii), reducing the recombination probability and the final efficiency of XUV generation. Longer driving wavelengths are known to drastically reduce the conversion efficiency [49–52], scaling roughly as $\lambda^{-5.5}$ [53].

The dynamics of step (ii) can be described by solving Newton's equations of motion for a charged particle influenced by the Lorentz force. If the driving laser field is assumed to be linearly polarized[4], $\tilde{\mathcal{E}}_0(t) = \mathrm{Im}\{\tilde{\mathcal{E}}(t)\} = \mathcal{E}_0 \sin(\omega_0 t)$, where $\mathcal{E}_0$ is the field peak amplitude, the motion is limited to a single dimension and described by

$$m_e \frac{\partial^2}{\partial t^2} x(t, t_i) = e\mathcal{E}_0 \sin(\omega_0 t), \tag{2.7}$$

where m_e and e are the electron mass and charge, and t_i is the time of ionization. Integrating twice with respect to time, and assuming that the electron ionizes to the continuum at the origin with zero kinetic energy, $x(t = t_i) = \frac{\partial}{\partial t} x(t = t_i) = 0$, an expression for the displacement of the free electron relative to its parent ion as a function of time and ionization time is obtained,

$$x(t, t_i) = \frac{e\mathcal{E}_0}{m_e \omega_0^2} \left[\sin(\omega_0 t) - \sin(\omega_0 t_i) - \omega_0 (t - t_i) \cos(\omega_0 t_i)\right]. \tag{2.8}$$

For recombination to occur in the third step, the electron must return to its parent ion, assumed stationary at $x = 0$, at some later time defined as the return time t_r. Eq. (2.8) is a transcendental equation and cannot be solved analytically. However, zero-crossings can be found numerically. Three groups of trajectories can be found, which depend on the ionization time, as shown in Fig. 2.5. For ionization times $0 < t < T/4$, where T is the laser period, the electron is accelerated to a too high kinetic energy before the field changes sign, and it will never return to its original position and recombine. Electrons which ionize at times $T/4 < t < T/2$ will recombine at times $T/2 < t < 5T/4$. The excursion times of the returning electrons vary depending on the ionization time, and can in general be divided into two classes of trajectories. These trajectories, henceforth referred to as the *long trajectory* and *short trajectory*, were experimentally verified in 1998 by Bellini *et al.* [57]. The characteristic times of the different trajectories are summarized below.

Trajectory	Tunneling time (T)	Recombination time (T)
Non-returning	$0 < t < 1/4$	–
Long	$1/4 < t < 1/3$	$19/20 < t < 5/4$
Short	$1/3 < t < 1/2$	$1/2 < t < 19/20$

Since the returning electrons ionize at the peak of the absolute value of the field amplitude, the emission process will repeat itself twice per laser cycle, which is also indicated in Fig. 2.5. For an isotropic generation medium the dynamics are identical up to a sign change when

---

[4] HHG from circular polarized driving fields was for a long time believed unfeasible due to the additional transverse momentum acquired by the EWP, prohibiting it from overlapping the ion. Using two counter-rotating circularly-polarized driving fields, generation of bright, circularly polarized harmonics has been demonstrated [54–56].

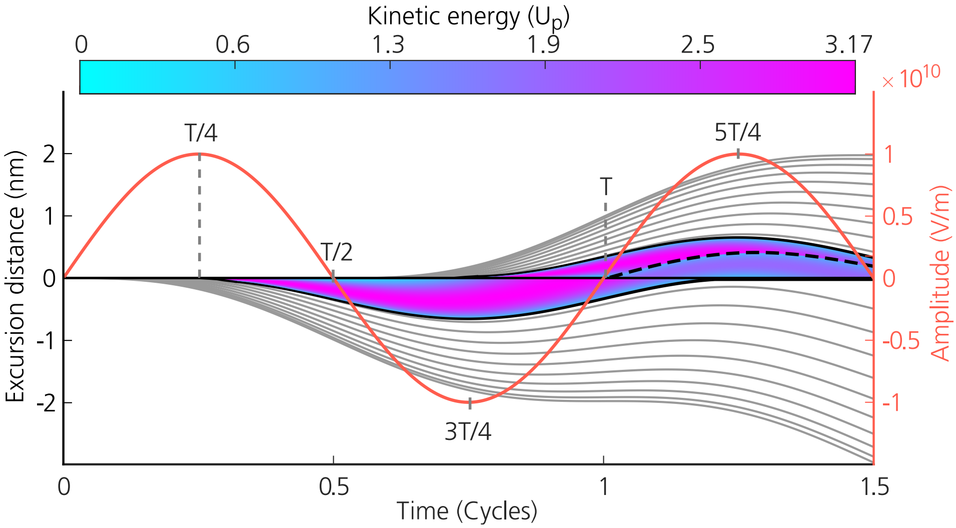

Figure 2.5: Electron trajectories in the TSM. Excursion distance of electrons tunnel ionizing at different times during the driving field cycle. Gray lines indicate electrons which do not return to their parent ion, while the colormap shows the return kinetic energy of those electrons which do return, with long and short trajectories outlined with a black solid line, and the re-scattered long trajectories outlined with a dashed black line. The driving field amplitude is shown in red.

introducing a π phase shift of the driving field. Given a many-cycle driving laser, the $T/2$ repetition rate leads in the frequency domain to odd harmonics of the fundamental[5], spaced by $2\omega_0$. Even longer trajectories are possible [59], indicated in Fig. 2.5 by the colored region with a dashed black border. These originate from electrons which return to the parent ion, rescatter, and subsequently go through additional cycles of acceleration away from, and back to the ion. The maximum return energy for higher order returns is lower, and due to the diffusion of the wave packet the recombination probability is low [60]. Longer trajectories may however noticeably contribute to the final harmonic emission, in particular for longer driving wavelengths [53, 61, 62].

The return kinetic energy E_k of the electron can be shown to be given by

$$E_k(t_i, t_r) = 2U_\mathrm{p} \left[\cos(\omega_0 t_r) - \cos(\omega_0 t_i)\right]^2 , \tag{2.9}$$

where U_p is called the *ponderomotive energy*. It is the cycle-averaged quiver energy of the

---

[5] Using two-color (ω–2ω) driving fields both odd and even harmonics can be generated. Such schemes can also increase the total conversion efficiency of the generation [58].

free electron in the laser field, given by

$$U_\mathrm{p} = \frac{e^2 {\mathcal{E}_0}^2}{4 m_e \omega_0^2} \propto \lambda^2 I, \tag{2.10}$$

where λ is the wavelength of the laser field and I is the field intensity related to the electric field by $I = c\epsilon_0 |\mathcal{E}_0|^2/2$, with c being the speed of light. The ponderomotive energy is proportional to the square of the wavelength, and linearly proportional to the intensity of the driving field.

From Eq. (2.9) the TSM successfully predicts the maximum kinetic energy of electrons at the time of recombination, as approximately $3.17 U_\mathrm{p}$. The recombination leads to emission of photons with energies corresponding to the sum of the ionization energy of the atom and the kinetic energy of the electron. The harmonic cut-off energy is then given by[6]

$$E_\text{cut-off} \approx I_\mathrm{p} + 3.17 U_\mathrm{p}, \tag{2.11}$$

where I_p is the ionization energy. By increasing the intensity, the cut-off energy can be extended [see Eq. (2.10)] since the free electron experiences a stronger acceleration due to the Lorentz force. This scaling is limited both by depletion of the single-atom ground state and, as will be seen in Chapter 3, by macroscopic effects related to the increased ionization of the medium. Increasing the wavelength instead, the length of the electron trajectory also increases, which allows it to gain more kinetic energy. Extension of the cut-off energy in this way is not as fundamentally limited as in the case of intensity scaling. While the previously mentioned increased diffusion of the electron wave packet results in an approximately $\lambda^{-5.5}$ scaling with wavelength of the single atom generation efficiency, this type of wavelength scaling provides a means of generating very high energy photons, reaching into the water window [63, 64], with potential applications in *e.g.* X-ray microscopy [65, 66], or even to harmonics with energies higher than 1 keV [67].

Figure 2.6 shows how the return kinetic energy in Eq. (2.9) varies as a function of t_i and t_r, respectively. Apart from at the cut-off at $3.17 U_\mathrm{p}$, there are two ionization and recombination times corresponding to the same return kinetic energy for every possible energy. These times are associated with the previously mentioned long (red line) and short (yellow line) electron trajectories. Due to the dependence of the recombination energy on the recombination time, the emitted XUV radiation exhibits a nonlinear spectral phase relation. This phase, stemming from the different trajectories in the presence of the laser field, is usually called the intrinsic, or *dipole phase* [68].

For the plateau harmonics, the time-dependent harmonic frequency can be approximated

---

[6] When accounting for the electron not ionizing at the origin the cut-off law reads $E_\text{cut-off} \approx F(I_\mathrm{p}/U_\mathrm{p}) I_\mathrm{p} + 3.17 U_\mathrm{p}$, with $F(I_\mathrm{p}/U_\mathrm{p}) \sim 1.32$ [46].

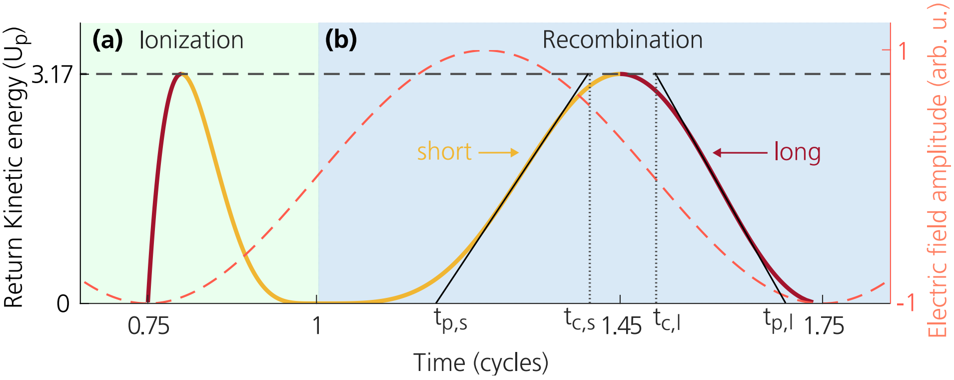

Figure 2.6: Return kinetic energy of electrons. (a) as a function of the ionization time and (b) as a function of the recombination time. The amplitude of the driving laser field is indicated by the dashed red line, and the maximum kinetic energy predicted by the semiclassical TSM is indicated by the dashed black line. Apart from the cut-off at $3.17U_\text{p}$, there are two ionization and recombination times corresponding to the same return kinetic energy for every possible energy. These times are associated with a long (red line) and short (yellow line) electron trajectory. The solid black lines show an approximate linear relation between the recombination time and return kinetic energy.

by a straight line [69], indicated by the black line for the long and short trajectory. Following the derivation in Ref. [70], the linear equation can be inverted and interpreted as the harmonic group delay. Integration with respect to time yields an approximate expression for the spectral phase as

$$\Phi_i(\Omega) \approx \alpha_i I + t_{p,i}\left(\Omega - \Omega_p\right) + \frac{\gamma_i}{I}\left(\Omega - \Omega_p\right)^2 , \tag{2.12}$$

where $i = s, \ell$ for the short and long trajectory, $\Omega = q\omega_0$ and $\Omega_p = I_\text{p}/\hbar$ are the frequencies of the harmonic and the threshold harmonic, respectively, where $\hbar$ is the reduced Planck constant, $\alpha_i I$ is the intensity and trajectory dependent dipole phase of the threshold harmonic, $t_{p,i}$ is the approximate threshold harmonic return time, and γ_i is given by

$$\gamma_i = \frac{\left(t_{c,i} - t_{p,i}\pi c^2 m_e\right)}{3.17\alpha_\text{FS}\lambda^2} \approx \begin{cases} -0.19\frac{cm_e}{\alpha_\text{FS}\lambda}, & i = \ell \\ 0.22\frac{cm_e}{\alpha_\text{FS}\lambda}, & i = s \end{cases} \tag{2.13}$$

where $t_{c,i}$ is the approximate cut-off harmonic return time and α_{FS} is the fine-structure constant. The constant α_i is approximately zero for the short trajectory, reflecting the brief time in the continuum of the shortest short trajectory. For the long trajectory it is given by $\alpha_\ell = -0.16\alpha_{FS}\lambda^3/(c^3 m_e)$. The approximate dipole phase obtained above from the TSM is compared to a quantum mechanical model in the next section, and its effect on the temporal properties of the emitted harmonics is discussed further in Sec. 2.2.3.

2.2.2 The Quantum Mechanical Picture

While providing an intuitive explanation, the semiclassical model above is unable to predict certain important quantum aspects of HHG, such as the dipole amplitude, wave packet diffusion and interference effects [71]. Hence, theories which attempt to solve the full Time-Dependent Schrödinger Equation (TDSE) of the atom and laser field, were developed [44, 46, 72]. In papers **I** and **II**, to simulate harmonic generation including propagation effects, we use the single atom dipole amplitude and phase at harmonic frequencies of the fundamental, multiplied by the atomic number density, as a source term for the harmonic radiation.

The basic assumption in these solutions is to use a Single Active Electron (SAE) approximation, where the active electron interacts with the laser field and the mean field of the remaining nucleus and other electrons. For a linearly polarized driving field in the z-direction, the TDSE takes the form

$$\mathrm{i}\hbar\frac{\partial}{\partial t}\left|\Psi(\boldsymbol{r},t)\right\rangle = \left[-\frac{\hbar^2}{2m_e}\nabla^2 + \hat{V}(\boldsymbol{r}) - e\tilde{\mathcal{E}}_0(t)z\right]\left|\Psi(\boldsymbol{r},t)\right\rangle , \tag{2.14}$$

where $\left|\Psi(\boldsymbol{r},t)\right\rangle$ is the wave function of the active electron, ∇^2 is the Laplacian, $\hat{V}$ is the effective atomic potential and $\tilde{\mathcal{E}}_0(t)$ is a real-valued oscillating electric field.

The time-varying field induces a time-varying dipole, $d(t) = \langle\Psi|\,\hat{z}\,|\Psi\rangle$, from which the single-atom emission spectrum, $|d(\omega)|^2$, can be calculated through the square of the Fourier transform of the time-averaged induced dipole [73, 74],

$$|d(\omega)|^2 = \left|\frac{1}{t-t'}\int_{t'}^{t}\mathrm{d}t''\exp\left[-\mathrm{i}\omega t''\right]d(t'')\right|^2 . \tag{2.15}$$

In practice, the time-varying field is modeled using a sinus modulated slowly varying envelope starting with a ramp function of 5 cycles, followed by a constant amplitude for another 15 cycles [45]. The Fourier transform is performed over the last 5 cycles, at which point any transient excitations have decayed.

In Fig. 2.7(a) the dipole amplitude, in atomic units, as a function of the peak intensity of the driving field is shown for two different harmonics in argon and neon. The intensity dependence in the cut-off region is characterized by a rapid exponential increase (black dashed line), while the exponent for the harmonics in the plateau region, averaged over the interference fringes as discussed below, is considerably smaller, around 2.6 for argon and 5.5 for neon (black solid line)[7]. In argon, intensities larger than 4×10^{14} Wcm^{-2} display

---

[7] These exponents can in principle be used to estimate the dipole amplitude assuming a simple power law $I_q = I^p$, with $p < q$ [75, 76].

a decreasing dipole amplitude due to depletion of the ground state in the first 15 cycles.

To capture the complete picture requires taking into account the many different possible return trajectories, including higher-order returns. The Single Atom Response (SAR) is the interference of the contributions of all such trajectories [71]. Since the phase of these contributions depends strongly on intensity [77], the dipole amplitude and phase of any given harmonic order will exhibit rapid oscillations as a function of the driving field peak intensity (see Fig. 2.7). This intensity dependent interference can, due to the intensity variations over time and space of the driving field, lead to effects such as spatio-spectral fringes in the far-field beam profile of individual harmonics [78, 79].

Shortly after the full TDSE describing the laser-atom system was solved, another quantum mechanical model was suggested. The Lewenstein model [46], or Strong Field Approximation (SFA), attempts to solve the same equation as above, but under the approximations that

i Only the ground state contributes to the evolution of the system
ii Depletion of the ground state is neglected[8]
iii After ionizing, the free electron is assumed to interact with the laser field only, neglecting the influence of the atomic potential $\hat{V}(\boldsymbol{r})$

Condition (iii) assumes that the laser field is strong compared to the potential of the atom, and gives the model its name. From the full TDSE calculation in Fig. 2.7 condition (ii) is seen to clearly be violated in argon above 4×10^{14} Wcm^{-2}.

Solving Eq. (2.14) for a linearly polarized electric field with the above approximations, and making use of a saddle-point method[9], one can show that the equation for the time-dependent dipole becomes [46]

$$d(t) \approx \mathrm{i} \int_0^\infty \mathrm{d}t_r \, \underbrace{d_{\boldsymbol{p}}^*(t)}_{\text{step (iii)}} \, \underbrace{\zeta(t_r) \exp\left[-\mathrm{i}S_{\boldsymbol{p}}(t, t_r)\right]}_{\text{step (ii)}} \, \underbrace{\tilde{\mathcal{E}}_0(t - t_r) d_{\boldsymbol{p}}(t - t_r)}_{\text{step (i)}} + \text{c.c.}, \qquad (2.16)$$

which can be interpreted as a quantum formulation of the semiclassical TSM [82]. Reading right to left, the first step is ionization into a continuum momentum state $\boldsymbol{p}$ at time $t - t_r$, where t_r is the return time, under the influence of the electric field, expressed by the product $\tilde{\mathcal{E}}_0(t-t_r)d_{\boldsymbol{p}}(t-t_r)$. In the second step, the electron wave packet propagates in the external

---

[8] This approximation can in general be relaxed by taking into account the depletion, which is discussed already in the original publication, and is often done today, see Ref. [80] for a review of commonly used methods.

[9] The saddle-point method leads to a qualitatively similar result as the full SFA, but leads to a rescaling of the dipole amplitude which depends on *e.g.* the wavelength, see Ref. [81] for a comparison.

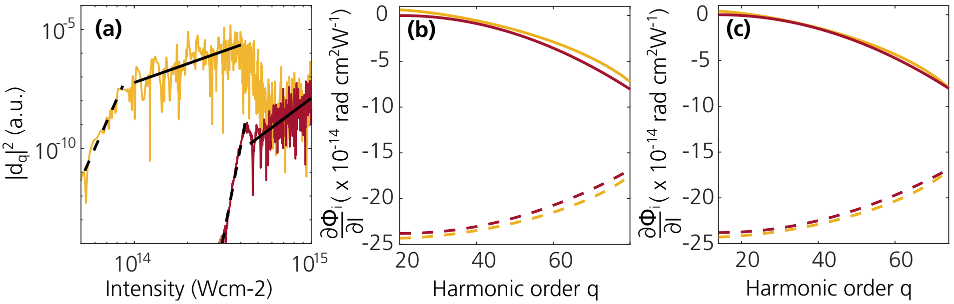

Figure 2.7: Quantum models of high-harmonic generation. (a) Amplitude of dipole strength for the 23rd harmonic in argon (blue) and 69th harmonic in neon (red) as a function of driving field intensity, obtained using full TDSE single atom calculations. (b) Comparison of derivative of spectral phase with respect to intensity obtained using the SFA (yellow) and using Eq. (2.12) (red) in argon, with a driving field intensity of 2.5×10^{14} Wcm^{-2} and (c) in neon using an intensity of 5×10^{14} Wcm^{-2}. Calculations for the short trajectory are shown as solid lines, and long trajectory are shown as dashed lines. Figure adapted from paper **I**.

field, which is described by $\zeta(t_r)\exp\left[-\mathrm{i}S_{\boldsymbol{p}}(t,t_r)\right]$, where $\zeta(t_r)$ is a function taking into account the quantum diffusion of the electron wave packet, and $S_{\boldsymbol{p}}(t,t_r)$ is the quasi-classical action, containing information about the phase accumulated by the electron during its trajectory. The third and final step is recombination at time t, expressed by the conjugate of the transition matrix element $d^*_{\boldsymbol{p}}(t)$.

The usefulness of the SFA when there was already a working quantum mechanical model with fewer approximations was discussed by Lewenstein *et al.* [46]. The full quantum model, *i.e.*, solving the TDSE, is exact within the single-active electron approximation but is computationally much more expensive. In addition, the SFA provides a useful link between the intuitive TSM and the full quantum mechanical model. One advantage of the full TDSE solution, is that it directly provides the dipole amplitude, with no assumption made on relative strengths of intra-atomic forces and electron-laser interactions [45]. For this reason the TDSE is used to calculate the dipole amplitude and phase used in the propagation simulations in Chapter 3.

For the macroscopic effects of HHG introduced in the next chapter, the phase accumulated by electrons during the acceleration in the laser field plays a major role. From the TSM an approximate expression for this phase is given in Eq. (2.12). To validate the use of this equation for our 1-Dimensional (1D) phase-matching model in paper **I** and **II**, we compare $\frac{\partial\Phi_i}{\partial I}$ as a function of harmonic order calculated within the SFA solving the saddle-point equations, with calculations using the approximate expression in Eq. (2.12) in Fig. 2.7(b,c). The good agreement motivates the use of the simple analytic expression for describing the effect of the dipole phase.

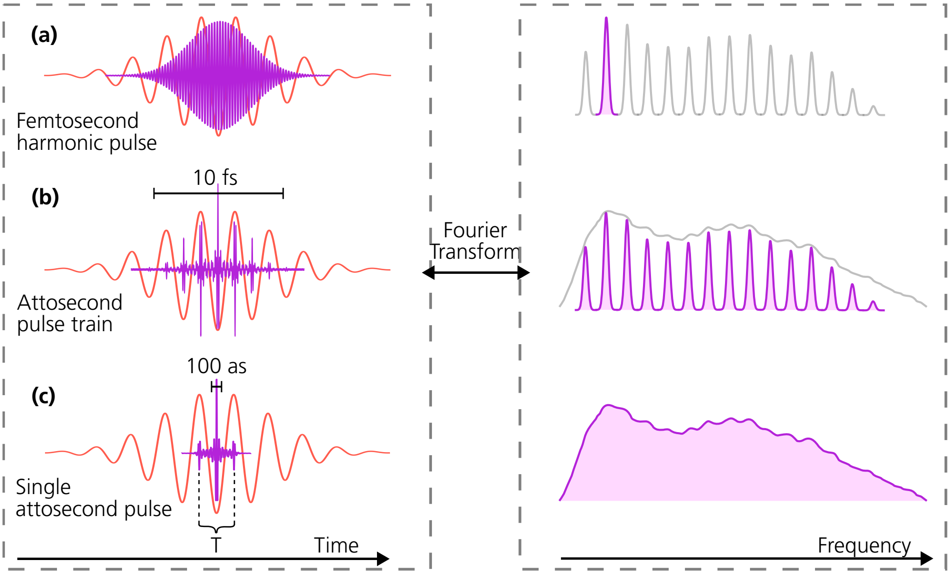

Figure 2.8: Sketch of the time-frequency representation of harmonic radiation. The Fourier transform relates frequency to the reciprocal variable time. (a) A single high harmonic of a femtosecond IR pulse corresponds to a femtosecond XUV pulse. (b) A frequency comb of phase locked harmonics corresponds to a train of attosecond pulses. (c) A broad continuum of frequencies in the high-order harmonic range corresponds to an isolated attosecond pulse.

2.2.3 Time-Frequency Representation of High-order Harmonics

The Heisenberg-Gabor limit already discussed for femtosecond pulses in Sec. 2.1 must also apply to the radiation obtained from the HHG process. After the experimental discovery and theoretical description of HHG, it was realized that if the different harmonics are phase-locked, the extremely broad bandwidth of the harmonic comb would support pulses of attosecond duration [83, 84]. The harmonic comb generated by a multi cycle femtosecond driving field was theoretically shown to represent a train of attosecond pulses, repeating every half cycle of the driving field [85]. This was verified experimentally in 2001 by Paul *et al.* [15].

After the generation of attosecond pulse trains, schemes for the generation of single Isolated Attosecond Pulses (IAPs) were developed [86]. IAPs are in general more challenging to generate than APTs, as they are either achieved by pushing the duration of the driving field towards the single-cycle limit, where control of the Carrier-Envelope-Phase (CEP) becomes important [87, 88], in combination with spectrally or temporally gating the generation [86, 89–91], or by angularly streaking the attosecond pulses in a train [92, 93].

The Fourier transform relation between the harmonic spectra and the temporal structure of the pulses is sketched in Fig. 2.8. In (a) a single harmonic order has been isolated in the frequency domain. Since each harmonic is generated every half cycle of the driving field, the single harmonic in the time domain is of femtosecond duration. In (b), the phase-locked generation and interference of harmonics every half cycle of the driving field results in a comb of odd-order harmonics in the frequency domain, and an APT in the time domain. Finally, in (c), the use of time-gated generation, or few-cycle driving fields, results in an IAP. In the frequency domain it is represented by a broadband continuum spectrum.

The dipole phase in Eq. (2.12) plays a non-negligible role in the temporal structure of the attosecond pulses [68], and as seen in Fig. 2.6, it is inherent to the HHG process. Being of approximately second order in frequency in the plateau, it leads to a chirp of the generated attosecond pulses. Since it is present across a broad frequency range, the effect in the temporal domain is a chirp of the individual attosecond pulses in the APT. This chirp is called the *attochirp* [94]. Using Eq. (2.12) it can be described by the second order derivative of the spectral phase with respect to frequency, as

$$\frac{\partial^2 \Phi_i}{\partial \Omega^2} = \frac{2\gamma_i}{I} \tag{2.17}$$

This chirp is intensity dependent, which is easily understood since the slope in Fig. 2.6 depends on the intensity through U_p. It leads to a stretching in time of the attosecond pulses, but is typically small enough that the pulses are still of attosecond duration.

Another important effect comes from the slowly varying envelope of the driving field, giving rise to a chirp of individual harmonics called the *femtochirp* [94]. As the dipole phase and amplitude depend on the intensity, and the intensity depends on time, the highest order harmonics are generated mostly at the peak of the driving field. This results in spectrally broader harmonics close to the cut-off, and a broadening in time of the attosecond pulses at the wings of the pulse train. These effects become more pronounced for shorter driving pulses, since the intensity variation becomes more rapid in that case.

2.3 The Lund Attosecond Laboratory Beamline

The laser and beamline described below were used in the experiments carried out in paper **IV**, the angle integrated measurements in paper **VI**, and papers **VII** and **IX**. The measurements for paper **V**, and the angle-resolved measurements in paper **VI** were performed before the upgrade of the laser and of the attosecond setup. The previous setup will not be discussed in this thesis.

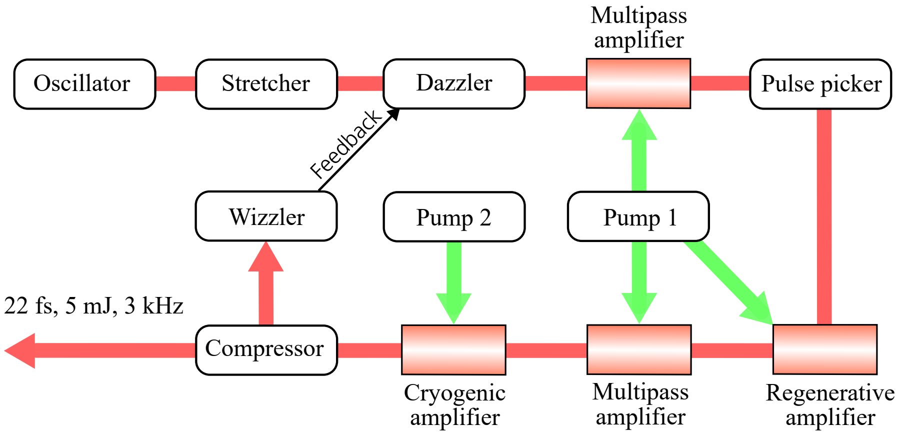

Figure 2.9: Sketch of the most important components of the laser system used in this work.

2.3.1 The Infrared Laser Source

The Lund attosecond laboratory laser system, sketched in Fig. 2.9, is based on a *Laser Quantum venteon^{CEP5}* Kerr-lens modelocked Titanium-Sapphire (Ti:Sa) [95] oscillator with a central wavelength of 800 nm and an output spectrum covering 650 to 950 nm, producing < 6 fs, 3 nJ pulses at a repetition rate of 80 MHz. Amplification is performed using the CPA technique as described in Sec. 2.1.1. Here, stretching is done using a single grating and a retroreflector in an abberation free Öffner triplet configuration [96, 97].

Following the stretcher, the pulses are sent into a *Fastlite Dazzler* [98], or Acousto-Optical Programmable Dispersive Filter (AOPDF), which allows shaping of the spectral amplitude and phase of the pulses. By reducing the bandwidth, the central wavelength of the laser may be tuned from 780 to 820 nm. The Dazzler is also used to compensate for dispersion caused by propagation in air from the laser to the application chambers by adding an additional negative dispersion.

The amplification is done in four stages in Ti:Sa crystals pumped by frequency doubled (527 nm central wavelength) Neodymium-doped Yttrium-Lithium-Fluoride (Nd:YLF) *Continuum Terra* lasers. The first stage is a multipass "*Booster*" amplifier, after which a Pockels cell is used as a pulse picker, selecting pulses at a repetition rate of 1 kHz/3 kHz before the next amplifier. The second stage is a regenerative amplifier containing a second AOPDF, a *Fastlite Mazzler*, to counteract gain narrowing [99]. The Mazzler is programmed for gain equalization by introducing a loss at frequencies in the pulse spectrum or Ti:Sa gain medium with strong peaks, resulting in a flatter, broader output spectrum. The third stage is another multipass amplifier, and the final stage is a three-pass amplifier cryogenically cooled to $-175\,^{\circ}$C to avoid thermal lensing effects and thermal damage [100].

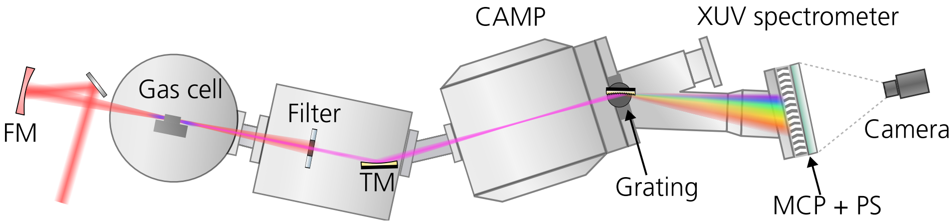

Figure 2.10: The high-order harmonic beamline in the attolab. The IR pulses are focused by a dielectric Focusing Mirror (FM) into a gas cell, where HHG takes place. The remaining infrared is filtered out by a metallic filter. The harmonics are focused by a gold coated Toroidal Mirror (TM) into the interaction region of a Chamber for Atomic and Molecular Physics (CAMP). A gold coated concave grating images the harmonic focus on a MicroChannel Plate (MCP). A Phosphor Screen (PS) is mounted behind the MCP, and a camera behind the PS finally detects the spatially and spectrally resolved harmonic signal.

After the four amplification stages, pulse energies up to 7.5 to 10 mJ are achieved. Compression to near-Fourier transform limited pulses ($\geq$ 22 fs duration) is done using two reflective holographic gratings. Due to the efficiency of the gratings ($\approx$ 65%) the final output pulse energy is reduced to 4.5 to 6.5 mJ[10]. In addition, a weak reflection of the compressed pulse is sent to a *Fastlite Wizzler*, providing single shot measurements of the spectral intensity and phase [102, 103]. The Wizzler is used in a feedback loop together with the Dazzler for optimization of the spectral phase of the compressed output pulses.

2.3.2 The Extreme Ultraviolet Light Source

The output pulses above are used to drive HHG in various targets. A sketch of the XUV beamline used during the course of this work is shown in Fig. 2.10. First, since the distance between the laser compressor and the XUV beamline is several meters, a *TEM Messtechnik Aligna* beam-pointing stabilization system is used to correct for long-term thermal drifts. The pulses are focused by a 50 cm focal length dielectric mirror into a vacuum chamber where high-order harmonics are generated. The HHG takes place in gas cells of 6 to 8 mm length and 500 µm hole diameter, which is placed slightly after the focus to preferentially emit the short trajectory [104] (see Sec. 3.2). The gas is supplied through a *MassSpecpecD AmsterdamPiezoValve* high frequency valve operating at 1 kHz/3 kHz[11] [105]. Various noble gases, such as argon, krypton, xenon and neon are used for generation, with backing pressures varying from 2 to 6 bar. The pressure inside the gas cell is much lower, and can be estimated by interferometric measurements. In optimal phase-matching conditions the

---

[10] Holographic gratings have comparatively low efficiency, but provide superior spatial quality due to not displaying periodic errors typical for ruled gratings, see *e.g.* Ref. [101] for an illustration of this advantage.

[11] The valve supports DC to 5 kHz repetition rate.

pressure inside the cell is estimated to be in the range of 20 to 300 mbar depending on the gas used. These values roughly correspond to the expected phase-matching pressures discussed in Chapter 3. The gas cell is mounted on a 5-axis $XYZ\theta_X\theta_Y$ stage which allows alignment relative to the laser beam in all directions except rotation about the cylindrically symmetric laser propagation axis.

After the generation chamber, a differential pumping hole separates the chamber from the recombination chamber to reduce residual gas reabsorption of the generated harmonics. Various 100 to 200 nm thick metallic filters, such as aluminum and germanium, are used to filter out the remaining IR radiation. Additionally, these filters partly compensate for the attochirp inherent to the HHG process [106], and may be used in combination to select different regions of harmonic orders due to their often sharp transmission windows.

The XUV radiation is refocused into the application chamber (CAMP)[12] by a gold coated toroidal mirror ($f = 30$ cm) at grazing incidence in a 2f-2f configuration. After the application chamber, an in-house built flat-field aberration corrected XUV spectrometer based on a gold coated, grazing incidence type *Hitachi* concave grating is used to characterize the XUV radiation [107]. The grating directs the first diffraction order onto a MicroChannel Plate (MCP), spectrally and spatially resolving the harmonics. A phosphor screen (PS) is placed behind the MCP, and a camera is used to image the response of the PS.

---

[12] Described further in experimental methods (see Sec. 4.4).

Chapter 3

Macroscopic Effects in High-order Harmonic Generation

In the previous chapter, the discussion on HHG and attosecond pulse generation was focused mainly on the microscopic single atom response. To completely understand and explain experimentally observed HHG spectra one must take into account macroscopic aspects of the generation process. These effects include propagation of the fundamental beam in a partially ionized medium, and the collective response of many single atoms emitting harmonic radiation with varying phases, *i.e., phase-matching*. In paper **I** an analytic model for optimization of the conversion efficiency is developed based on these macroscopic effects. This chapter begins with an overview of the numerical methods used in papers **I**, **II** and **III**. The basic underlying principles and limitations of phase-matched HHG are introduced, and the model is compared to numerical calculations from paper **I** and experimental results from paper **II**.

3.1 Wave Propagation in a Dielectric Medium

In order to investigate HHG numerically, the scalar wave equation in a dielectric medium is considered following Ref. [75, 108]. Neglecting the magnetic field and assuming linear polarized light, the inhomogeneous wave equation can be described as

$$\left[\nabla^2 - \frac{1}{c^2}\frac{\partial^2}{\partial t^2}\right]\tilde{\mathcal{E}}(r,t) = \mu_0 \frac{\partial^2}{\partial t^2}\left[\tilde{\mathcal{P}}^{\mathrm{L}}(r,t) + \tilde{\mathcal{P}}^{\mathrm{NL}}(r,t)\right], \tag{3.1}$$

where μ_0 is the vacuum permeability and $\tilde{\mathcal{P}}^{\mathrm{L}} = \epsilon_0(\chi^{(\mathrm{a})} + \chi^{(\mathrm{e})})\tilde{\mathcal{E}}$ is the linear polarization response to the electric field, which depends on the atomic susceptibility[1] $\chi^{(\mathrm{a})}$ and electronic susceptibility $\chi^{(\mathrm{e})}$. The nonlinear correction to the polarization density [see Eq. (2.5)] is denoted $\tilde{\mathcal{P}}^{\mathrm{NL}}$. As will be discussed later, for efficient HHG, the ionization degree in the medium is usually limited to below a few percent, so that the contribution of free currents $\tilde{\mathcal{J}}$ have been neglected in the above equation.

In dispersive media, the wave equation must be solved for every frequency in the pulse. For many-cycle driving pulses, the spectrum of the total electric field in HHG is well represented by a Fourier series of odd orders of the driving field frequency ω_0. Furthermore, The polarization of the medium is mainly driven by the fundamental field, at the same frequency ω_0, so that the electric field and nonlinear polarization can be expanded as

$$\tilde{\mathcal{E}} = \textstyle\sum_{q=1}^{\infty} \mathcal{E}_q \mathrm{e}^{-\mathrm{i}q\omega_0 t}, \tag{3.2a}$$

$$\tilde{\mathcal{P}}^{\mathrm{NL}} = \textstyle\sum_{q=1}^{\infty} \mathcal{P}_q^{\mathrm{NL}} \mathrm{e}^{-\mathrm{i}q\omega_0 t}. \tag{3.2b}$$

Inserting the above equations in Eq. (3.1) yields a system of coupled equations

$$\sum_{q=1}^{\infty}\left[\nabla^2 + k_q^2\right] E_q = \sum_{q=1}^{\infty} -\mu_0\omega_q^2 P_q^{\mathrm{NL}}, \tag{3.3}$$

where $\omega_q = q\omega_0$ is the harmonic frequency, and $k_q = n_q k_{q,0}$ is the harmonic wavenumber, $n_q = \sqrt{1 + \chi_q^{(\mathrm{a})} + \chi_q^{(\mathrm{e})}}$ is the refractive index at frequency $q\omega_0$, and $k_{q,0}$ is the vacuum harmonic wavenumber. For $\hbar\omega > I_{\mathrm{p}}$ the refractive index is complex, with $\mathrm{Re}\{n\}$ describing dispersion, and $\mathrm{Im}\{n\}$ describing absorption in the medium.

The above equation can be further simplified by invoking the paraxial approximation, using either the slowly-varying envelope approximation, or the more rigorous split-operator method. Following the derivation using the split-operator method in [110, 111], each component of Eq. (3.3) can be written as

$$\left[\frac{\partial^2}{\partial z^2} + \nabla_\perp^2 + k_q^2 - \hat{P}_q\right] E_q = 0, \tag{3.4}$$

---

[1] Here, we neglect the contribution from the ions, which can become important for strongly, multiply ionized media [109].

where $\nabla_\perp^2$, refers to double differentiation with respect to the transverse directions x and y. The propagation direction is chosen along z, and $\hat{P}_q$ defines an operator, which when acting on the electric field returns the function $-\mu_0\omega_q^2 P_q^{\mathrm{NL}}$. Defining the operators $\hat{T}$ and $\hat{Q}$ as

$$\hat{T}^2 = \frac{\partial^2}{\partial z^2}, \tag{3.5a}$$

$$\hat{Q}^2 = \nabla_\perp^2 + k_q^2 - \hat{P}_q, \tag{3.5b}$$

and factorizing yields

$$\left\{\left(\hat{T} + \mathrm{i}\hat{Q}\right)\left(\hat{T} - \mathrm{i}\hat{Q}\right) + \mathrm{i}\left[\hat{T}, \hat{Q}\right]\right\} E_q = 0, \tag{3.6}$$

where the commutator $\left[\hat{T}, \hat{Q}\right] \approx 0$ if variations of the refractive index and polarization density along the propagation directions are sufficiently small on length scales on the order of the wavelength[2]. When this approximation holds, couplings between backward and forward propagating waves can be neglected. Considering the forward propagating wave, *i.e.*, the $\hat{T} - \mathrm{i}\hat{Q}$ term above, and performing a Taylor expansion of $\hat{Q}$, results in the paraxial inhomogeneous Helmholtz equation[3]

$$\left(2\mathrm{i}k_{q,0}\frac{\partial}{\partial z} + \nabla_\perp^2 - k_q^2\right)\bar{E}_q = -\mu_0\omega_q^2 \bar{P}_q^{\mathrm{NL}} \mathrm{e}^{-\mathrm{i}\Delta k_q z}, \tag{3.7}$$

where the difference in wavenumber between the generated harmonic field and the polarization induced at frequency $q\omega_0$ is $\Delta k = qk_1 - k_q$. Here, the slowly varying electric field and polarization are given as $E_q = \bar{E}_q \mathrm{e}^{\mathrm{i}k_q z}$ and $P_q^{\mathrm{NL}} = \bar{P}_q^{\mathrm{NL}} \mathrm{e}^{\mathrm{i}qk_1 z}$, respectively.

Note that for the fundamental field, the nonlinear term of the polarization can be assumed to be weak compared to the polarization induced by the propagating fundamental field $[P^{\mathrm{NL}} \ll \epsilon_0(\chi_\mathrm{a} + \chi_\mathrm{e})E_1]$. The equation reduces to the *homogeneous* paraxial Helmholtz equation, of which one solution is the Gaussian beam. In the following, the fundamental beam is always assumed to be a Gaussian beam unless otherwise specified.

In the simulations of HHG in this work, the propagation equation is solved numerically under the above approximations. The propagation is modeled using a finite difference propagation code in cylindrical coordinates, assuming cylindrical symmetry, based on a Crank-Nicholson algorithm [75, 108]. While Eq. (3.7) does not explicitly contain any time variable, time-dependence is included by constructing time slices of a pulse intensity en-

---

[2] This is similar to the slowly-varying envelope approximation, but more rigorous, as it gives explicit conditions on the relation between the slowly varying quantities and the wavelength.

[3] This assumes that the transverse wavenumber is small compared to the total wavenumber, *i.e.* paraxial waves, and that the nonlinear polarization correction is small compared to the electric field.

velope, and propagating them separately, while keeping track of the free electron density in the medium. The generation of harmonics enters through the nonlinear polarization P_q^{NL}, for which intensity dependent single-atom dipole amplitudes and phases, and ionization rates, are calculated by solving the time-dependent 3-dimensional (3D) Schrödinger equation assuming the SAE approximation (as described in Sec. 2.2.2). The accuracy of the model is limited to long pulses due to the assumptions of a slowly varying refractive index and source term. For methods[4] going beyond the slowly-varying approximations see Ref. [113–115].

3.1.1 Scaling Laws

In the decades since HHG was first realized, the diversity in available laser sources, and as a consequence HHG sources, has increased. Today, characteristic parameters of HHG sources, such as peak power and repetition rate, may vary by several orders of magnitude [116]. Efficient generation of high-order harmonics is routinely demonstrated using high-average-power, low pulse energy ($E_p \sim \mu$J) lasers, based on parametric amplification [31, 32, 117], or post-compressed, ytterbium-doped femtosecond lasers [118, 119], or using Ti:Sa lasers with low repetition rate, and pulse energies of up to hundreds of mJ [30, 120–123].

Irrespective of the differences in available laser sources, optimization of HHG has long been explored both experimentally and theoretically by scaling the pulse energy, average power, focal length and medium length [124–126], while reaching similar conversion efficiencies [29, 31]. The apparent invariance of HHG in such vastly different generation conditions was explained and experimentally verified by Heyl *et al.* [33]. The proposed scaling laws describe how the driving pulse focusing, and the characteristics of the generation medium, should be scaled to reach the same CE when the input pulse energy is scaled.

For electromagnetic wave propagation in vacuum, scaling invariance under the transformation $(x, y, z) \rightarrow (\eta x, \eta y, \eta^2 z)$, where η is a scaling parameter, can be easily verified for a general paraxial wave equation,

$$\left[\frac{\partial}{\partial z} - \frac{\mathrm{i}}{2k}\nabla_\perp^2\right]\tilde{E} = 0. \tag{3.8}$$

If the electric field $\tilde{E}(x, y, z, \omega)$ is a solution, then so is $\tilde{E}(\eta x, \eta y, \eta^2 z, \omega)$.

For equations describing paraxial waves in dielectric media, such as Eq. (3.7)[5], the density of the nonlinear medium and the energy of the input pulse must also be scaled appropri-

---

[4] See Ref. [112] for a useful guide to different laser pulse propagation methods.

[5] Note that these scaling laws are valid also for the case of broadband pulses.

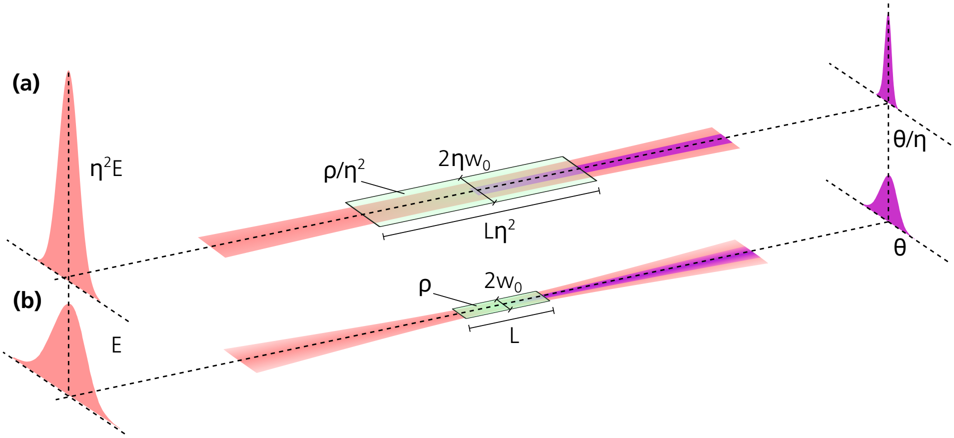

Figure 3.1: Scaling of wave-propagation in nonlinear media. High-order harmonic generation in (a) loose focusing regime and (b) tight focusing regime.

ately [33]. In Eq. (3.7), the third term on the left hand side, and the nonlinear polarization depend linearly on the density[6], requiring that the density is scaled as $\rho \rightarrow \rho/\eta^2$. Nonlinear optical phenomena also depend on the intensity in the medium, which affects the nonlinear polarization P^{NL}. To counteract the change in intensity when scaling the size of the beam requires to also scale the input pulse energy as $E_p \rightarrow \eta^2 E_p$.

Figure 3.1 illustrates the scaling of HHG between loose and tight focusing. Interestingly, because the pulse energy scaling keeps the local intensity invariant, the dipole phase entering phase-matching of HHG remains invariant as well. Furthermore, the constant pressure–length product ensures that reabsorption of the generated harmonics is also invariant, which leads to a harmonic pulse energy scaling following directly the input energy scaling, and thus to scale-invariance of the conversion efficiency. Because of this, a general scale-invariant description will be employed in the following discussion, by scaling relevant parameters by the Rayleigh length z_{R}.

3.2 Phase-matching

In Sec. 2.1 the interference of waves of different frequencies with non-zero phase offsets was shown to result in a lower peak intensity through destructive interference. In phase-matching of HHG, waves of the *same* frequency, generated with different phases and at different positions in a macroscopic medium, interfere. To maximize the constructive interference requires to match the relative phases of the radiation emitted by adjacent atoms,

---

[6] This is true for HHG in gases and many other nonlinear optical phenomena, see Ref. [127].

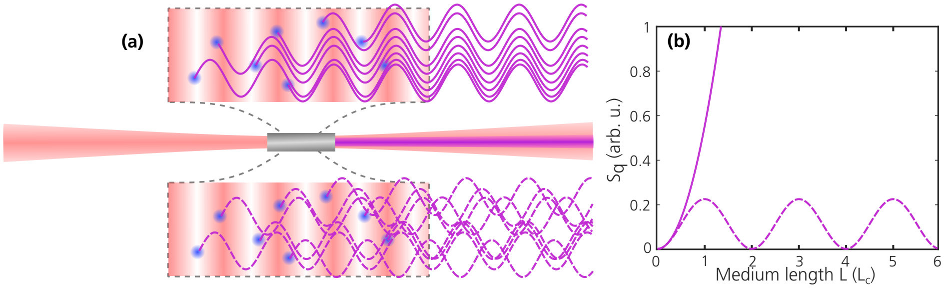

Figure 3.2: Illustration of phase-matching. (a) Sketch of harmonic generation in the case of perfect phase-matching and imperfect phase-matching. (b) Build-up of harmonic signal I_q with the propagation length L for the perfectly (solid) and imperfectly (dashed) phase-matched case.

which is called phase-matching. Phase-matching in HHG is usually described using a k-vector approach. For the long-wavelength, many-cycle pulses considered here, this reduces to a phase velocity mismatch between the harmonic fields and the fundamental driving field. In HHG using few-cycle pulses or short driving wavelengths, the group velocity mismatch or “CEP-slip” can also become significant [128, 129]. The wave vector mismatch between the generated harmonic and the polarization induced at frequency ω_q is given by [*Cf.* Eq. (3.7)]

$$\Delta \boldsymbol{k} = q\boldsymbol{k}_1 - \boldsymbol{k}_q. \tag{3.9}$$

By considering propagation along a certain direction, *e.g.*, z, the wave vector mismatch can be related to the accumulated phase-mismatch by $\Delta k_z = \frac{\partial}{\partial z}\Delta\Phi$. Ignoring off-axis emission and transverse variations of the fundamental, that is, assuming a 1D model, and assuming for now there is no reabsorption (discussed further in Sec. 3.3.4), the harmonic intensity as a function of the propagation length can be written as

$$I_q \propto \left| \int_0^L \mathrm{d}z\, d_q \rho \exp\left[\mathrm{i}\Delta k z\right] \right|^2, \tag{3.10}$$

where $P^{\mathrm{NL}} \propto \rho d_q$ was used, where ρ is the density of the gas medium, d_q is the single atom dipole amplitude from Sec. 2.2.2 and $|\Delta\boldsymbol{k}| = \Delta k$. The above equation represents the coherent addition of all emitters along the propagation length.

If the density is assumed to be constant, and generation in a small volume is considered, such that variations in the dipole amplitude and wave vector mismatch are small, the above equation simplifies to the well known form [130]

$$I_q \propto \rho^2 |d_q|^2 L^2 \mathrm{sinc}^2\left(\frac{\Delta k L}{2\pi}\right), \tag{3.11}$$

which shows that the harmonic signal can be written as a product of a microscopic single atom response and macroscopic phase-matching function as $I_q \propto |d_q|^2 S_q(\Delta k_q, L)$.

Figure 3.2(a) shows a sketch of perfectly and imperfectly phase-matched generation. The total signal as a function of the propagation distance, L, is shown in Fig. 3.2(b). The intensity in the perfectly phase-matched case, where all atoms in the medium emit in phase, corresponding to $\Delta k = 0$, grows as L^2. In the imperfectly phase-matched case, ($\Delta k \neq 0$), the intensity oscillates, as the generated field and induced polarization periodically dephase and rephase. The oscillation is described by $\mathrm{sinc}^2(L/2L_\mathrm{c})$, where $L_\mathrm{c} = \pi/\Delta k$ is the *coherence length*, a measure of the length across which constructive interference occurs. For medium lengths $L < L_c$ the phase-mismatched case grows approximately quadratically.

The above example illustrates the importance of coherence control in HHG [68], which essentially means minimizing the wave vector mismatch. In HHG in gases, the wave vector mismatch can be described by a sum of four terms as [113, 131]

$$\Delta k = \Delta k_\mathrm{at} + \Delta k_\mathrm{fe} + \Delta k_\mathrm{foc} + \Delta k_\mathrm{i}, \tag{3.12}$$

where Δk_at arises from the dispersion in the neutral medium and Δk_fe from the dispersion due to the free electrons present in the medium. Phase variations due to the laser focusing are included in Δk_foc, and finally, Δk_i is the dipole phase, due to the trajectory dependent (short or long) microscopic single atom response [77], described in Sec. 2.2.2. The reason it appears in the macroscopic description of HHG is because of its strong dependence on intensity, which is a macroscopically varying parameter in typical HHG relying on strongly focused lasers pulses. The four contributing terms are expressed in more detail below.

Δk_at The dispersion relation of a neutral dielectric medium leads to a phase-velocity mismatch between the fundamental and harmonic fields, which can be described in a free focusing geometry[7] through the wave vector mismatch

$$\Delta k_\mathrm{at} = (n_1 - n_q)\frac{q\omega_0}{c}, \tag{3.13}$$

where n_1 and n_q are the refractive indices at frequencies ω_0 and $q\omega_0$. At the fundamental frequency, $n_1 > 1$, whereas at the harmonic frequencies above the ionization threshold $n_q < 1$, so that this contribution is positive. The refractive index of the fundamental and harmonic field can be related to the dynamic polarizability, α_q, through

$$n_q = \sqrt{1+\chi} = \sqrt{1 + \frac{\rho\alpha_q}{\epsilon_0}} \approx 1 + \frac{\rho\alpha_q}{2\epsilon_0}, \tag{3.14}$$

---

[7] In propagation in *e.g.* hollow core capillary or other guided geometries, the effect of the mode dispersion in the wave guide should also be taken into account [132].

which leads to an approximate expression for the wave vector mismatch

$$\Delta k_{\mathrm{at}} = \frac{q\omega_0\rho}{2\epsilon_0 c}\left(1-\eta_{\mathrm{fe}}\right)\left(\alpha_1-\alpha_q\right) \approx \frac{q\omega_0\rho}{2\epsilon_0 c}\left(\alpha_0-\alpha_q\right), \tag{3.15}$$

where the factor in the first parentheses takes into account a finite ionization degree, η_{fe}. The polarizability at the fundamental wavelength can be approximated by the static polarizability (α_0, tabulated in for example Ref. [133]), at long wavelengths. The polarizability at harmonic frequencies can be obtained from tabulated refractive index data [134], or when such data is unavailable, be calculated using for example random phase approximation methods (see Ref. [135] and references therein).

Δk_{fe} Similarly to Δk_{at} above, the dispersion due to free electrons can be expressed as

$$\Delta k_{\mathrm{fe}} = (n_1^{\mathrm{e}} - n_q^{\mathrm{e}})\frac{q\omega_0}{c}, \tag{3.16}$$

where n_1^{e} and n_q^{e} are the plasma refractive indices at frequencies ω_0 and $q\omega_0$. These follow the inequality $n_1^{\mathrm{e}} < n_q^{\mathrm{e}} < 1$, so that this contribution is negative.

The plasma refractive index n_q^{e} is given by

$$n_q^{\mathrm{e}} = \sqrt{1-\frac{\rho_{\mathrm{e}}}{\rho_{\mathrm{c}}}}, \tag{3.17}$$

where $\rho_{\mathrm{e}} = \rho\eta_{\mathrm{fe}}$ is the free electron density and $\rho_{\mathrm{c}}(\omega) = \epsilon_0 m_e \omega^2/e^2$ is the critical density, at which the frequency ω equals the plasma frequency and the plasma becomes opaque. The free electron density in gases is typically much lower than the critical density, so that the wave vector mismatch can be expanded as

$$\Delta k_{\mathrm{fe}} = -\frac{q\omega_0\rho}{2\epsilon_0 c}\frac{\eta_{\mathrm{fe}}e^2}{m_e}\left(\frac{1}{\omega_0^2}-\frac{1}{q^2\omega_0^2}\right) \approx -\frac{q\rho}{2\epsilon_0 c}\frac{\eta_{\mathrm{fe}}e^2}{m_e\omega_0}. \tag{3.18}$$

Since ionization is a prerequisite of HHG, the free electron density necessarily varies in time and space during the HHG process. Because the ionization rate is a highly nonlinear function of the driving field intensity, this variation is typically the limiting factor in coherence control of HHG. Several methods for calculating the ionization rate exist, which are discussed in further in Sec. 3.3.1.

Δk_{foc} When a laser beam goes through a focus, there is an additional phase advance compared to plane wave propagation. For a Gaussian beam the phase variation is the *Gouy phase* shift [136]. The on-axis contribution of the Gouy phase is given by $\zeta(z) = -\tan^{-1}(z/z_R)$. Because of the inverse dependence of the Rayleigh length on the wavelength, the contribution of the harmonic Gouy phase is typically an order of magnitude smaller than the fundamental contribution, and it is hence often

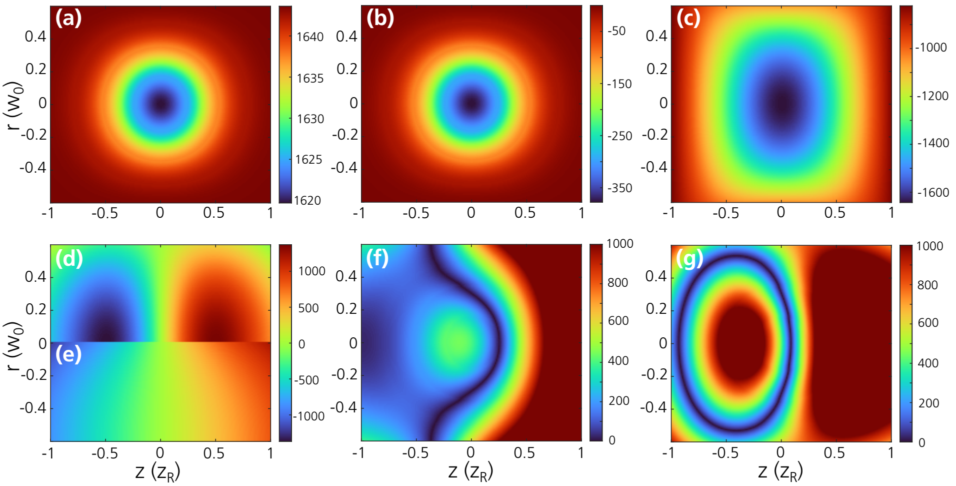

Figure 3.3: Wave vector mismatch. Contributions of the wave vector mismatch across the focus of a Gaussian beam for the 23$^{\text{rd}}$ harmonic in argon (colorscale) due to: (a) Neutral atoms Δk_{at}. (b) Free electrons Δk_{fe}. (c) Gouy phase Δk_{foc}. Dipole phase for (d) the long trajectory Δk_{ℓ} and (e) the short trajectory Δk_{s}. Total (absolute) wave vector mismatch for (f) the short trajectory and (g) the long trajectory. The ionization rate is calculated using the the Perelomov–Popov–Terent'ev (PPT) model [see Sec. 3.3.1], and the ionization degree is taken at the peak of the pulse for a Gaussian pulse of $\tau = 22$ fs FWHM duration, with peak intensity $I_0 = 2 \times 10^{14}$ Wcm^{-2}. The pressure in the medium is constant, at 30 mbar and $z_{\text{R}} = 0.014$ m.

neglected. The wave vector mismatch due to the focusing of a Gaussian beam is then given by

$$\Delta k_{\text{foc}}(r,z) = -q\frac{\partial}{\partial z}\left[\zeta(z) - \frac{kr^2}{2R(z)}\right] \xrightarrow{r,z\to 0} = -\frac{q}{z_R}, \tag{3.19}$$

where the second term in the brackets is an off-axis component due to the radius of curvature of the wavefronts at z, with $R(z) = z(1 + z_{\text{R}}^2/z^2)$. This contribution is negative. For a guided geometry Δk_{foc} is equal to zero.

Δk_{i} The dipole contribution arises from the phase accumulated by the electron as it accelerates in the continuum in the presence of a laser field (step (ii) of the TSM). An approximate expression for this dipole phase was given in Eq. (2.12) [70]. The dependence of Φ_{i} with intensity, and therefore with z, leads to a wave vector mismatch

$$\Delta k_{\text{i}} = \frac{\partial \Phi_{\text{i}}}{\partial I}\frac{\partial I}{\partial z}. \tag{3.20}$$

The derivative of the phase with respect to intensity becomes

$$\frac{\partial \Phi_\mathrm{i}}{\partial I} = \alpha_\mathrm{i} - \gamma_\mathrm{i} \left(q\omega_0 - \frac{I_\mathrm{p}}{\hbar} \right)^2 \frac{1}{I^2}, \tag{3.21}$$

with the variables defined as in Eq. (2.12). For a Gaussian beam Eq. (3.20) becomes

$$\Delta k_\mathrm{i} = -\frac{2z\beta_\mathrm{i}(z)}{z^2 + z_\mathrm{R}^2}, \tag{3.22}$$

where

$$\beta_\mathrm{i}(z) = \alpha_\mathrm{i} I(z) - \frac{\gamma_\mathrm{i}}{I(z)} \left(q\omega_0 - \frac{I_\mathrm{p}}{\hbar} \right)^2 < 0, \tag{3.23}$$

and $I(z)$ describes the intensity variation of a Gaussian beam along its propagation direction. The sign of Δk_i changes across the focus, being negative when $z < 0$ and positive when $z > 0$. Close to the focus the contribution is negligible.

Based on the signs of the contributions above, phase-matching at or before the focus of the fundamental beam is accomplished by compensating the negative contribution of the free electrons, the dipole phase, and the fundamental Gouy phase by the positive contribution from the neutral medium, $\Delta k_\mathrm{at} = |\Delta k_\mathrm{fe}| + |\Delta k_\mathrm{foc}| + |\Delta k_\mathrm{i}|$. When generating after the focus, where the dipole phase is positive, phase-matching is instead achieved when $\Delta k_\mathrm{at} + \Delta k_\mathrm{i} = |\Delta k_\mathrm{fe}| + |\Delta k_\mathrm{foc}|$. As discussed in connection to the free electron contribution, the wave vector mismatch is a function of both the time and the spatial coordinates, which is true also for the dipole contribution and atomic dispersion (except under the assumption that $\eta_\mathrm{fe} \sim 0$). Meanwhile, the focusing term is a function of the spatial coordinate, and is time-independent if reshaping of the fundamental beam is kept small. Based on this, it is clear that fulfilling the condition $\Delta k = 0$ across the entire generation volume for the duration of the driving field is not trivial, or even possible, and phase-matching in practice is limited to minimizing Δk across a small volume for a limited duration of time. To illustrate this, Fig. 3.3 shows how the different terms, and the total wave vector mismatch, vary across the focus assuming a medium of constant density, for both the long and short trajectory. Note that even here, this is just a snapshot in time, corresponding to the peak of a 22 fs pulse with peak intensity $I_0 = 2 \times 10^{14}\,\mathrm{W\,cm^{-2}}$. At the given moment, the ionization degree in the medium varies from roughly 0 to 6%. The small variation in the neutral atom contribution is seen in Fig. 3.3(a), and the rather large difference in the dipole contribution for the two trajectories is clear when comparing Fig. 3.3(d) and (e). Another important effect, which comes from the difference in dipole phase and can be observed by comparing the total wave vector mismatch of the short and long trajectory, is that the two trajectories can be selectively phase-matched by changing the generation position. The short trajectory, which can be selected by generating after the focus, is often preferred due to its better spatial qualities [68].

3.2.1 Pressure-induced Phase-matching

In the above example in Fig. 3.3, two important tuning parameters for minimizing the wave vector mismatch were mentioned: the pressure[8], and the ionization degree, which is controlled through the intensity. These are also the parameters which are often most easily tuned in experiments.

The approximately linear dependence of both the refractive index and plasma refractive index on density [see Eq. (3.15) and Eq. (3.18)], allows the definitions $\Delta\kappa_{\mathrm{at}} = \Delta k_{\mathrm{at}}/\rho$ and $\Delta\kappa_{\mathrm{fe}} = \Delta k_{\mathrm{fe}}/(\rho\eta_{\mathrm{fe}})$ to be made. Isolating the density from the total wave vector mismatch under the assumption of perfect phase-matching $\Delta k = 0$ yields [29, 137]

$$\rho_{\mathrm{match}} = -\frac{\Delta k_{\mathrm{foc}} + \Delta k_{\mathrm{i}}}{\Delta\kappa_{\mathrm{at}} + \eta_{\mathrm{fe}}\Delta\kappa_{\mathrm{fe}}}, \tag{3.24}$$

which defines a phase-matching density as a function of the ionization degree. This equation states that, given some ionization degree, perfect phase-matching can be obtained if the density of the neutral medium is chosen appropriately [138]. The equation diverges when the ionization degree increases and the denominator approaches zero, which defines a critical ionization degree[9], above which perfect phase-matching on axis is not possible. The critical ionization degree is given by [132, 139]

$$\eta_{\mathrm{fe}}^{\mathrm{mac}} = -\frac{\Delta\kappa_{\mathrm{at}}}{\Delta\kappa_{\mathrm{fe}}} = \frac{m_{\mathrm{e}}\omega_0^2}{e^2}\left(\alpha_0 - \alpha_q\right). \tag{3.25}$$

Using Eq. (3.25) and the ideal gas law, where k_{B} is the Boltzmann constant and T is the temperature, the phase-matching pressure becomes

$$p_{\mathrm{match}}(z) z_{\mathrm{R}} = \frac{2 m_{\mathrm{e}}\omega_0\epsilon_0 c k_{\mathrm{B}} T f_{\mathrm{i}}(z)}{e^2(\eta_{\mathrm{fe}}^{\mathrm{mac}} - \eta_{\mathrm{fe}})}, \tag{3.26}$$

where

$$f_{\mathrm{i}}(z) = \frac{z_{\mathrm{R}}^2}{z^2 + z_{\mathrm{R}}^2}\left(1 + \frac{2z\beta_{\mathrm{i}}(z)}{q z_{\mathrm{R}}}\right), \tag{3.27}$$

is a geometric factor originating from the Gouy phase and dipole phase and hence depends on the trajectory. At the focus $f_i = 1$, resulting in the same phase-matching pressure for both trajectories. The phase-matching pressure variation with the ionization degree is shown for a few harmonics in argon and neon in Fig. 3.4(a,b) assuming a medium position

---

[8] The pressure and density will be used interchangeably in the following, by assuming a constant temperature and that the ideal gas law holds.

[9] The critical ionization degree depends on harmonic order and the atomic species, but is typically a few percent. It is around 6% for the 23rd harmonic in argon, and 1.1% for the 69th harmonic in neon.

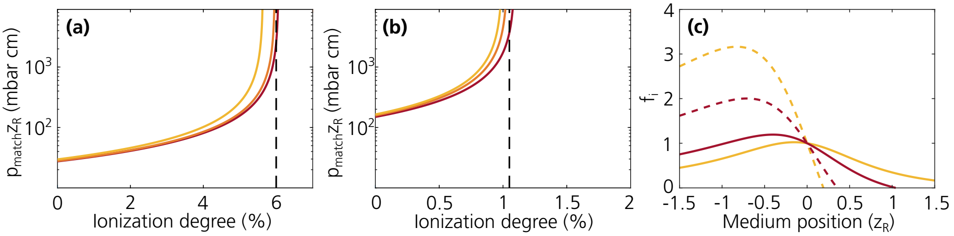

Figure 3.4: Pressure induced phase-matching. Phase-matching pressure (a) for harmonic 19 (red), 23 (orange) and 27 (yellow) in argon and (b) for harmonic 63 (red), 69 (orange) and 75 (yellow) in neon. (c) Factor f_i for the 23rd harmonic in argon (red) and 69th harmonic in neon (yellow) for the short (solid) and long (dashed) trajectory. The intensity at the center of the medium is $I = 2.5 \times 10^{14}\,\text{W}\,\text{cm}^{-2}$, and $I = 5 \times 10^{14}\,\text{W}\,\text{cm}^{-2}$, for argon and neon, respectively. Figure adapted from paper **I**.

at the laser focus. As the medium position is changed, the factor f_i leads to a separation in phase-matching pressure between the long and short trajectory, as shown in Fig. 3.4(c). When the medium is positioned after the focus, f_i becomes negative for the long trajectory, reflecting the well-known fact that this trajectory in general is not possible to phase-match after the focus [85]. Based on the scaling laws discussed previously, the pressure is multiplied by the Rayleigh length and the medium length is expressed in units of the Rayleigh length, which provides a description that is independent of the focusing geometry of the driving laser.

From the phase-matching pressure curves some interesting predictions can be made. At low ionization degrees relative to $\eta_{\text{fe}}^{\text{mac}}$ the pressure variation is rather small and takes a similar value for all harmonic orders, which indicates that broadband phase-matching can occur simultaneously over a rather large volume and time in the generation medium. On the other hand, at high pressures, phase-matching is possible for a very narrow range of ionization degrees for a given harmonic order. Efficient generation is then limited to short time intervals and small volumes, similar to ionization gating [140]. While transient phase-matching results in spectrally broad harmonics, the harmonic order dependent critical ionization means phase-matched generation takes place at different times for different harmonic orders. This in turn could affect the attosecond pulse-train, limiting the bandwidth of individual attosecond pulses in the train.

3.3 Limitations

In the previous sections, phase-matching was described in a mostly idealized manner. Minimizing the wave vector mismatch is clearly limited by ionization, however the ionization degree can also lead to reshaping of the fundamental beam, and act as a limiting factor for the range of pulse lengths and intensities for which efficient HHG is possible. Furthermore, reabsorption of the generated XUV, which is the inverse of the ionization process, also limits the conversion efficiency. This section introduces ionization models used in this work, and discusses the above limitations due to ionization and propagation in the partially ionized medium.

3.3.1 Ionization

In Sec. 2.2.1 strong field ionization, being the first step in the TSM, was shown to be a prerequisite for HHG. The low probability of recombination with the parent ion in the third step leads to a build-up of free electrons in the medium. In the previous section, these free electrons were shown to be a limiting factor in macroscopic phase-matching of HHG. Understanding of the relationship between intensity and the variation of the electron density is thus important to know under what conditions efficient HHG can be realized. In part of this work, the Perelomov–Popov–Terent'ev (PPT) model [141], outlined below, has been used to provide an analytical complement to solving the full 3D TDSE.

Strong field ionization of atoms is often divided into two limiting cases:

i Tunnel ionization, which is assumed for HHG described by the TSM. In this non-perturbative regime, the field must be strong enough to bend the atomic potential to a point where the tunneling probability is sufficiently high, and the frequency of the field must be low enough that the electron has time to tunnel out of the barrier.

ii Multi-photon ionization, valid when the applied laser field can be regarded as a perturbation to the atomic potential. In this regime the field is weak, and/or the frequency of the field is high enough that no quasistatic barrier is formed. When more photons are absorbed than required to overcome the ionization potential this type of ionization is called *Above-Threshold Ionization* (ATI).

Ionization in these two limits was described by Keldysh [142][10], who also formulated a useful quantity to determine which regime applies in a specific case. The *Keldysh parameter* depends on the frequency, ionization potential and electric field strength as

$$\gamma \equiv \frac{\omega_0 \sqrt{2I_\mathrm{p}}}{\mathcal{E}_0}, \tag{3.28}$$

with tunnel ionization valid if $\gamma < 1$, and multi-photon ionization takes place when $\gamma \gg 1$. In the limit $\gamma \ll 1$ the barrier is suppressed below the ground state energy level of the

---

[10] Keldysh's paper is famously difficult to read, which has recently motivated the publication of a rederivation of his work [143].

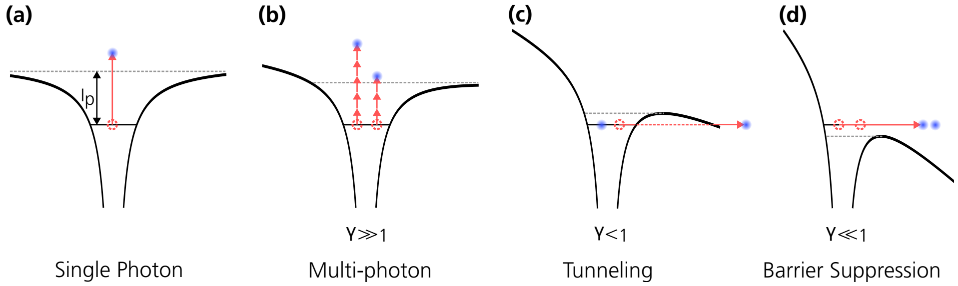

Figure 3.5: Photoionization in different regimes. (a) Single photon ionization. (b) Above threshold ionization and multi-photon ionization. (c) Tunneling ionization. (d) Barrier suppression ionization. The ionization potential is indicated by the dashed gray line.

atom, leading to all atoms immediately ionizing and to both a single-atom response and macroscopic phase-matching response which are essentially zero. The different ionization regimes are illustrated in Fig. 3.5.

Often, the parameters of the driving laser and target atom in HHG places the Keldysh parameter in the intermediate ($\gamma \sim 1$) regime[11]. In this intermediate regime, the PPT model can be successfully applied to calculate ionization rates. The discussion of the PPT model here will be confined to linear polarization, however it is valid also for the case of elliptical polarization. The field is assumed to be turned on adiabatically at $t_0 \to -\infty$, and the wavelength is much larger than the radius of the atom, so the electric field is treated as uniform. The method is valid for driving fields where the photon energy is small compared to the characteristic electron excitation energy, in this case the ionization potential $\hbar\omega_0 \ll I_\mathrm{p}$.

The ionization rate $\Gamma^{\mathrm{PPT}}_{\ell m}(\mathcal{E}, \omega_0)$ from a level with binding energy I_p, orbital ℓ and magnetic m quantum number, with the quantization axis chosen parallel to the field polarization, is given (atomic units are used: $\hbar = m_e = e = 1$) by

$$\begin{aligned}\Gamma^{\mathrm{PPT}}_{\ell m}(\mathcal{E}_0, \omega_0) = &\sqrt{\frac{3}{2\pi}} |C_{n^*,\ell^*}|^2 f_{\ell,m} I_\mathrm{p} \left[\frac{2(2I_\mathrm{p})^{3/2}}{\mathcal{E}_0\sqrt{\gamma^2+1}}\right]^{2n^*-|m|-3/2} \\ &\times A_m(\gamma,\omega_0) \exp\left[-2(2I_\mathrm{p})^{3/2}\frac{g(\gamma)}{3\mathcal{E}_0}\right]\end{aligned} \tag{3.29}$$

where $\mathcal{E}_0$ is the peak electric field, $n^* = Z/\sqrt{2I_\mathrm{p}}$ and $\ell^* = n^* - 1$ are the effective principal and orbital quantum numbers and C_{n^*,ℓ^*}, $f_{\ell,m}$, $A_m(\gamma,\omega_0)$ and $g(\gamma)$ are functions defined in Appendix A. Most importantly, $A_m(\gamma,\omega_0)$ contains a sum over many-photon processes

---

[11] As an example, in the calculation of ionization degree for Fig. 3.3 the range of the Keldysh parameter is approximately $0.8 < \gamma < 1.2$.

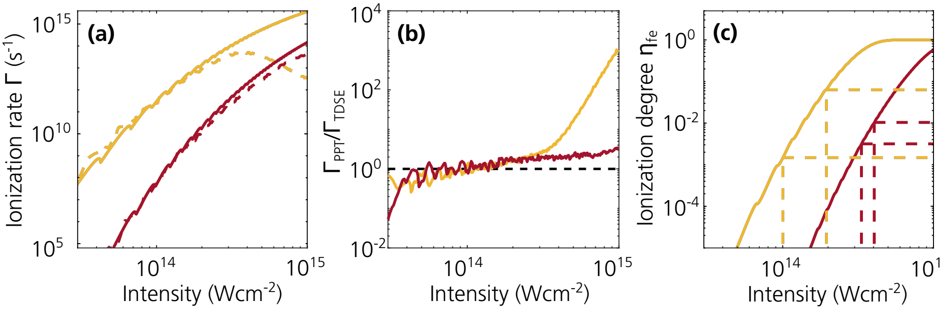

Figure 3.6: Strong field ionization rates. (a) Ionization rates in argon (yellow) and neon (red) obtained using (PPT) (solid) and solving the TDSE (dashed). (b) PPT ionization rate divided by the TDSE ionization rate in argon (yellow) and neon (red). (c) Ionization degree at the peak of a 22 fs FWHM pulse in argon (yellow) and neon (red) assuming the PPT ionization rate. The vertical dashed lines indicate the intensities I_{mic} and I_{mac}, and the horizontal dashed lines indicate the corresponding ionization degrees $\eta_{\mathrm{fe}}^{\mathrm{mic}}$ and $\eta_{\mathrm{fe}}^{\mathrm{mac}}$. Figure adapted from paper **I**.

of different orders, corresponding to the probability of absorption of increasing number of photons.

The ionization rate as a function of the driving field intensities calculated using the PPT model is shown in Fig. 3.6(a) and compared to the results from solving the 3D TDSE, in both argon and neon. The steps visible in the calculations using the PPT approximation are due to channel closings, which occur when the increase of the ionization energy due to the additional quiver energy of an electron in strong laser fields exactly matches the energy of an additional photon [144]. This leads to a slight reduction in ionization rate as the intensity is increased. The deviation between PPT and TDSE at high intensity visible for argon corresponds to depletion, which is not included in PPT. The ratio $\Gamma_{\mathrm{PPT}}/\Gamma_{\mathrm{TDSE}}$ is shown in Fig. 3.6(b), and compared to unity (black dashed line), showing that for a wide range of intensities, particularly those applied in HHG, the PPT model gives satisfactory results.

In the low frequency limit (tunneling regime), the PPT model reduces to the significantly simpler Ammosov–Delone–Krainov (ADK) approximation [145]. The ionization rates calculated with ADK deviate more than PPT from the TDSE results, for a comparison see Ref. [146]. As the driving laser pulse length approaches the single-cycle limit, where sub-cycle dynamics become important [128, 147–149], models which describe sub-cycle ionization rate are required. One such model which extends the (cycle averaged) PPT is the Yudin–Ivanov ionization model [150].

Based on the ionization rates in Fig. 3.6(a), the ionization degree, required to calculate Δk, can be obtained. The ionization degree at the peak of the pulse, assumed centered at $t = 0$, is given by

$$\eta_{\text{fe}} = 1 - \exp\left[-\int_{-\infty}^{0} \mathrm{d}t\, \Gamma[I(t)]\right]. \tag{3.30}$$

Intensity dependent ionization degrees are shown in Fig. 3.6(c) at the peak of a Gaussian pulse with 22 fs FWHM pulse duration. These calculations are used to define intensity windows for efficient HHG in the next section.

3.3.2 Intensity Windows for Efficient Generation

For efficient HHG it is not enough just to have perfect phase-matching, which is evident when writing the harmonic signal as a product [see Eq. (3.11)]

$$I_q \propto |d_q|^2 S_q(\Delta k_q, L), \tag{3.31}$$

where both the microscopic response $|d_q|$ and the phase-matching function S_q depend nonlinearly on the driving field intensity. The interplay between intensity, SAR and ionization dependent wave vector mismatch leads to intensity intervals within which efficient generation is possible.

The lower bound on usable intensities is defined by the *microscopic* cut-off energy [Eq. (2.11) and Fig. 2.7], beyond which the dipole amplitude decreases rapidly. The minimum intensity is

$$I_{\text{mic}} = \frac{m_e \omega_0^2}{3.17 \times 2\pi\alpha}\left(q\omega_0 - \frac{I_{\text{p}}}{\hbar}\right). \tag{3.32}$$

with the index "mic" indicating a quantity limited by the microscopic single atom response. From the relationship between intensity and ionization degree, a corresponding ionization degree $\eta_{\text{fe}}^{\text{mic}}$ can be defined.

The upper bound is defined by the *macroscopic* critical ionization degree [Eq. (3.25) and Fig. 3.4] above which perfect phase-matching is not possible. Because the dipole amplitude increases with intensity, phase-matching close to the peak of the pulse should in general be optimal. The upper intensity bound, I_{mac}, with the index "mac" indicating it is limited by macroscopic phase-matching, is therefore defined by reaching the critical ionization degree at the moment of the peak of the pulse. The microscopic and macroscopic intensities and ionization degrees are indicated by the dashed lines in Fig. 3.6(c). Calculating I_{mac} for a given pulse duration is done by repeated numerical integration of Eq. (3.30) for increasing values of the peak pulse intensity, until the intensity which yields $\eta_{\text{fe}}^{\text{mac}}$ at the peak of the pulse is found. Recently, analytic expressions for I_{mac} based on ADK and PPT were proposed by Minneker *et al.* [151].

The dependence of the intensity bounds with harmonic order and pulse duration is also im-

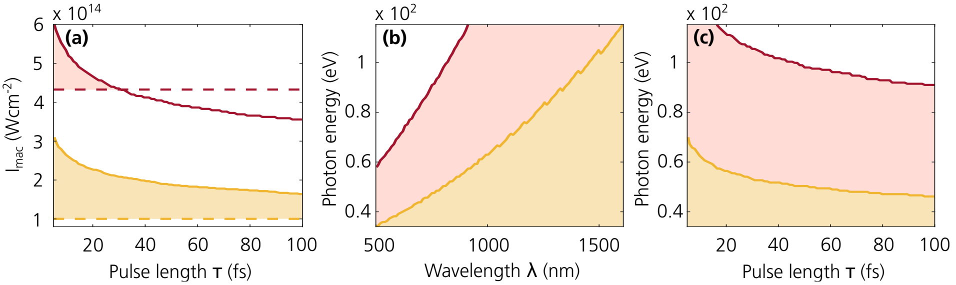

Figure 3.7: Phase-matching windows. (a) Intensity window of efficient generation for the 23rd harmonic in argon and 69th harmonic in neon indicated by the yellow and red shaded areas, respectively. The solid line shows the variation of I_{mac} and the dashed line corresponds to I_{mic}. Variation of the phase-matching cut-off in argon (yellow) and neon (red) with (b) the driving field wavelength and (c) the driving pulse FWHM duration. Figure adapted from paper **I**.

portant. For higher harmonic orders, I_{mac} generally decreases, and I_{mic} increases, reducing the intensity window for efficient HHG. Similarly, increasing the pulse duration, the ionization degree which is obtained at the peak of a pulse increases, which reduces I_{mac}, while I_{mic} remains unchanged. As a result, for longer pulses or higher harmonic orders, at some point $I_{\text{mac}} = I_{\text{mic}}$, as shown in Fig. 3.7(a). This equality defines a cut-off harmonic [152], above which efficient HHG is not achievable. By using shorter driving pulses [153, 154], the phase-matching cut-off can be extended, while simultaneously allowing for higher intensities to be used, increasing the SAR. These limitations have also partly been responsible for a shift towards longer driving wavelengths[12] [67, 76, 152], where both the cut-off energy and ionization rate scale favorably, making available harmonic energies in the soft X-ray region. Figure 3.7(b,c) displays how the phase-matching cut-off harmonic energy scales with driving wavelength and pulse duration.

3.3.3 Plasma Effects

The time-dependent ionization degree in the generation medium leads to potentially adverse effects also for the propagating fundamental beam. For a beam with a transverse intensity variation, such as a Gaussian beam, the free electron density in the partially ionized medium will also display transverse variations. A radially decreasing electron density, and hence radially increasing refractive index, leads to plasma induced defocusing and reshaping of the fundamental beam [156]. The defocusing mainly limits the peak intensity in the medium and leads to an effective focus position which is located before the focus in absence of a medium.

---

[12] For long wavelengths (> 3 μm), the often assumed dipole approximation may break down [155].

For very high laser intensities ($I_0 > 10^{15}\,\mathrm{Wcm}^{-2}$), in what is sometimes called the overdriven regime, reshaping of the fundamental beam can lead to new, efficient phase-matching regimes in HHG. In this regime, contributions from the nonlinear refractive index play a non-negligible role. In particular, self-guiding of the driving field can lead to a spatio-temporally constant fundamental intensity, which leads to smaller variations of the wave vector mismatch across the medium [157–159], increasing efficiency. Strong defocusing can also lead to much higher spatial derivatives of the fundamental intensity, which affect the dipole contribution Δk_{i} and can extend the phase-matching cut-off [160]. In general, HHG in the overdriven regime has been shown to lead to high conversion efficiencies, but the generated radiation partly or fully loses its harmonic structure, resembling more a continuum [158, 161–164], making it unsuitable for the RABBIT experiments which are discussed in the following chapters.

In this work, since we are concerned with conventional phase-matching at ionization degrees below $\eta_{\mathrm{fe}}^{\mathrm{mac}}$, defocusing is expected to be small. The degree of defocusing can be estimated with the defocusing length, L_{D} [165–167] as

$$L_{\mathrm{D}} = \frac{\pi c \epsilon_0 m_e \omega_0 k_{\mathrm{B}} T}{p \eta_{\mathrm{fe}} e^2} = \frac{\pi c \epsilon_0 m_e \omega_0 \sigma_{\mathrm{abs}}}{\eta_{\mathrm{fe}} e^2} L_{\mathrm{abs}}, \tag{3.33}$$

where L_{abs} is the *absorption length*, treated in the next section. The defocusing length describes the propagation distance at which the diffraction limited beam divergence has increased by a factor of two. For phase-matched HHG at the laser focus, and below the critical ionization, $L_{\mathrm{D}} > 17 L_{\mathrm{abs}}$ for the 23rd harmonic in argon and $> 26 L_{\mathrm{abs}}$ for the 69th harmonic in neon, given an 800 nm fundamental wavelength. As will be shown in the next section, the medium length is typically much shorter than the above *minimum* defocusing lengths. For longer driving wavelengths plasma defocusing is stronger and is more likely to limit the efficiency in HHG.

3.3.4 Absorption Limited High-order Harmonic Generation

The description of pulse propagation in a dielectric medium [Eq. (3.7)] permits complex wave vectors when the photon energy of the propagating light is larger than the ionization potential. In this case, the imaginary part, denoted here as κ_q, describes the reabsorption of the XUV light in the medium. Including these effects in Eq. (3.10) gives a modified phase-matching function so that Eq. (3.11) becomes [168, 169]

$$I_q \propto \rho^2 |d_q|^2 \mathrm{e}^{-\frac{L}{2L_{\mathrm{abs}}}} \frac{\cosh\left(\frac{L}{2L_{\mathrm{abs}}}\right) - \cos\left(\frac{\pi L}{L_{\mathrm{c}}}\right)}{\frac{\pi^2}{L_{\mathrm{c}}^2} + \frac{1}{4L_{\mathrm{abs}}^2}}, \tag{3.34}$$

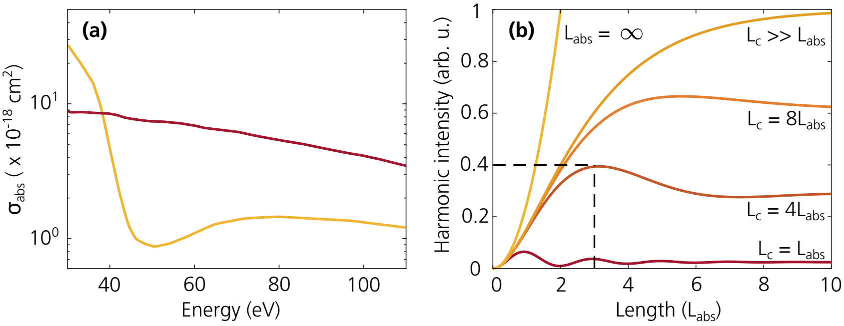

Figure 3.8: Absorption limit in HHG. (a) Absorption cross section in argon (yellow) and neon (red). (b) Variation of the harmonic intensity with the medium length for different coherence lengths. The dashed black lines indicate the optimal medium length, $L \approx 3L_{\text{abs}}$, given a coherence length $L_{\text{c}} = 4L_{\text{abs}}$. Figure adapted from paper **I**.

where $L_{\text{abs}} = 1/2\kappa_q = 1/\rho\sigma_{\text{abs}}$ denotes the absorption length, and σ_{abs} is the absorption cross section at frequency $q\omega_0$, shown in Fig. 3.8(a) for argon and neon at typical XUV energies obtained from HHG using near-infrared drivers.

Reabsorption acts to strongly limit the highest harmonic signal which can be obtained, as is evident from Fig. 3.8(b). For a finite absorption length, indefinite quadratic growth is not possible even for infinite coherence lengths, as an equilibrium is reached between the generated and reabsorbed signal. Shorter coherence lengths shifts the point of equilibrium to shorter medium lengths and consequently lower peak harmonic intensities.

In Ref. [168], Constant *et al.* define conditions for ensuring a high yield as

$$L_{\text{med}} > 3L_{\text{abs}}, \tag{3.35a}$$
$$L_{\text{c}} > 5L_{\text{abs}}, \tag{3.35b}$$

which corresponds to the top right part in Fig. 3.8(b). These limits loosely define whether the generation can be considered absorption-limited or coherence-limited. It should be noted that absorption-limited HHG is not always possible. For harmonics generated close to the Cooper minimum[13] in argon, the absorption length becomes very long, while the phase-matching pressure and wave vector mismatch only change slightly. Even if the coherence length could be extended, the role of plasma defocusing of the fundamental may no longer be negligible.

The model by Constant *et al.* [Eq. (3.34)] can be extended to include the effects of linear density gradients at the beginning and end of the generating medium [171], indicating that steep pressure gradients at the edges of the medium are preferable for CE optimization.

---

[13] The rapid variation of the cross section in Ar is due to a Cooper minimum at 52 eV [170].

3.4 Optimization of High-order Harmonic Generation

The scaling laws by Heyl *et al.* [33] show how the focusing geometry, medium length and gas density can be scaled to reach a similar CE when scaling the input pulse energy, but do not say *how* these parameters should be chosen to optimize the CE. In current experimental HHG setups a large variety of medium geometries is used, even for similar laser parameters. These include generation in high-pressure gas jets [15], low-pressure cells [63], semi-infinite cells [172] and capillaries [132]. Analytic expressions based on absorption-limited HHG [168, 173, 174], and to some extent experimental [175] observations suggest that optimal CE should occur for a constant pressure–length product, *i.e.*, along a pressure–length hyperbola.

From Eq. (3.34) [see also Fig. 3.8(b)], for a given coherence length, expressed by the ratio $L_\mathrm{c}/L_\mathrm{abs} = \zeta$, where ζ is a constant[14], an optimal medium length can be determined. We express it as a constant multiplied by the absorption length, $L_\mathrm{med}^\mathrm{opt} = \varsigma L_\mathrm{abs}$. In Fig. 3.8(b) the dashed black lines exemplify this relation for $\zeta = 4$, $\varsigma \approx 3$. The constant ς can be determined from Eq. (3.34) by first rewriting it as

$$I_q \propto \mathrm{e}^{-\frac{L}{2L_\mathrm{abs}}} \left[\cosh\left(\frac{L}{2L_\mathrm{abs}}\right) - \cos\left(\frac{\pi L}{\zeta L_\mathrm{abs}}\right)\right]. \tag{3.36}$$

The first (nonzero) solution to the derivative of Eq. (3.36) with respect to L/L_abs corresponds to the optimal medium length, and gives the value of $\varsigma = L_\mathrm{med}^\mathrm{opt}/L_\mathrm{abs}$ as the solution to the transcendental equation,

$$\mathrm{e}^{\frac{\varsigma}{2}} \left[2\pi \sin\left(\frac{\pi\varsigma}{\zeta}\right) + \zeta \cos\left(\frac{\pi\varsigma}{\zeta}\right)\right] = \zeta, \tag{3.37}$$

for which a few values is given in the table below.

ζ	1	2	3	4	5	6	7	8
ς	0.92	1.72	2.45	3.14	3.78	4.40	4.99	5.57

Using the definition of L_abs, the optimal medium length can then be written as

$$L_\mathrm{med}^\mathrm{opt} = \varsigma L_\mathrm{abs} = \frac{\varsigma k_\mathrm{B} T}{p \sigma_\mathrm{abs}}, \tag{3.38}$$

which defines a hyperbolic relationship between pressure and the optimal medium length. For optimal (phase-matched) HHG, the pressure should be close to $p_\mathrm{match}(z) \geq p_0(z)$ [see

---

[14] This assumes that both quantities are proportional to the pressure in the following discussion.

Eq.(3.26)], where $p_0(z)$ is the minimum phase-matching pressure, obtained from Eq. (3.26) for $\eta_{\text{fe}} = 0$, and is given by

$$p_0(z)z_{\text{R}} = \frac{2\epsilon_0 c k_{\text{B}} T f_{\text{i}}(z)}{\omega_0(\alpha_0 - \alpha_q)}. \tag{3.39}$$

The hyperbolic relationship in Eq. (3.38) can then be reformulated as

$$(p_{\text{match}} - p_0)L = \frac{\varsigma k_{\text{B}} T f_{\text{i}}(z)}{\sigma_{\text{abs}}}, \tag{3.40}$$

where we have included the dependence on medium position on the r.h.s. by redefining the phase-matching pressure relative to the pressure at the laser focus ($p_{\text{match}} = p_{\text{match}}(z)/f_{\text{i}}(z)$ and $p_0 = p_0(z)/f_{\text{i}}(z)$).

The hyperbolic equation should be invariant to a high degree under scaling of the focusing conditions or pulse lengths. In extreme cases, at very high intensities and pressures, where avalanche ionization must be taken into account, the scaling laws in Sec. 3.1.1 may break down [127]. In such conditions phase-matching is likely already limited by ionization or other high pressure effects, including clustering or loss of coherence in the single atom response due to electron excursion lengths approaching the mean free path in the continuum [31, 176].

3.4.1 Simulation Results

In this section Eq. (3.40) is compared with simulation results based on the method discussed in Sec. 3.1. Simulations of the CE of the 23rd harmonic in argon, as a function of the medium length and pressure, are shown in Fig. 3.9(a-c) for three different peak intensities of the driving field for a medium centered around the laser focus.

The peak driving field intensities which lead to the highest CE in the simulations are larger than those described by I_{mac}, which can be explained by volume arguments. In defining I_{mac} the peak intensity on axis was assumed, however to reach a high CE requires efficient generation also at transverse coordinates in the pulse. By using intensities between $2I_{\text{mic}}$ to $2I_{\text{mac}}$, efficient generation across a large volume and time is ensured.

The simulations display a region of high CE which follows a pressure–length hyperbola. The position of the hyperbola is to a large extent independent of the intensity, and agrees well with the model, indicated by the dashed white line, given a constant $\varsigma = 3$. It should be noted that ς is a fitting parameter which depends on harmonic order and absorption cross section, and it describes a time- and volume-averaged coherence length relative to absorption length. For higher order harmonics in argon, close to the Cooper minimum,

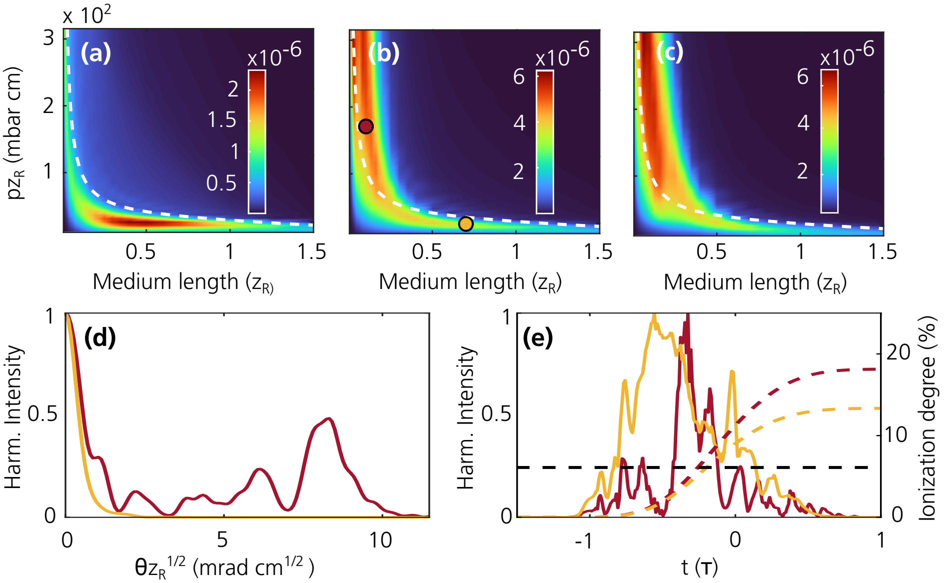

Figure 3.9: The two phase-matching regimes. Simulated conversion efficiency (colorscale) of the 23rd harmonic in argon for a peak intensity of (a) 1.5×10^{14} Wcm^{-2} (b) 2.5×10^{14} Wcm^{-2} (c) 4.5×10^{14} Wcm^{-2} for a medium centered at the laser focus. The dashed white line indicates the model prediction [Eq. (3.40)]. (d) Far-field beam profile and (e) temporal shape of the harmonic in the high-pressure (red) and low pressure (yellow) regime. The pressure and length used in the two cases is indicated by the circles in (b). The dashed red and yellow lines in (e) indicate the average on-axis ionization degree and the dashed black line corresponds to $\eta_{\text{fe}}^{\text{mac}}$. Figure adapted from paper **I**.

a lower value of ς can be expected due to the much lower absorption cross section, hence longer L_{abs} [this effect is illustrated in Fig. 4 of paper **II**].

From the hyperbolic model and pressure-induced phase-matching curves in Fig. 3.4 and Sec. 3.2, two phase-matching regimes, which are connected to the horizontal and vertical branches of the hyperbola, can be identified:

i In the horizontal branch, the ionization degree is low ($\Delta k_{\text{fe}} \approx 0$), and phase-matching happens close to $p = p_0$ when $\Delta k_{\text{at}} + \Delta k_{\text{foc}} + \Delta k_{\text{i}} = 0$. Due to the pressure dependence of Δk_{at}, phase-matching is limited to a narrow range of pressures[15]. As a result of the low pressure, the absorption length is long, and a long medium is required for a high CE.

---

[15] This range can become very narrow for higher orders due to a linear dependence of the wave vector mismatch with harmonic order, $\Delta k_q \propto q$, for pressures $p \neq p_{\text{match}}$.

ii In the vertical branch, the ionization degree is high ($\eta_{\mathrm{fe}} \approx \eta_{\mathrm{fe}}^{\mathrm{mac}}$), and phase-matching requires very high pressures. Consequently, the absorption length is short, and a short medium must be used. The dipole and focusing contributions to the wave vector mismatch become small relative to the pressure-dependent atomic and free electron contributions. Phase-matching happens when $\Delta k_{\mathrm{at}} + \Delta k_{\mathrm{fe}} \approx 0$, and becomes close to pressure-independent.

For the lowest intensity [Fig. 3.9(a)] the high-pressure region displays a comparatively low CE. This can be explained by the above phase-matching regimes. When the intensity is low, ionization degrees close to $\eta_{\mathrm{fe}}^{\mathrm{mac}}$ are either never reached, or not reached until late in the pulse when the dipole amplitude is small, resulting in a low CE.

While the CE is comparable between the two branches of the hyperbola, the generated harmonics are not. Both spatial and temporal variations between the two branches can be rather large, as shown in Fig. 3.9(d,e). Contrary to the well-collimated emission in the horizontal branch, the vertical branch is associated with strong off-axis emission. This emission is attributed to off-axis phase-matching of the long trajectory [104, 177], which is known to result in ring-like structures in the near-field spatial profile of the emission [68]. The temporal shape of the emitted generation shown in Fig. 3.9(e) confirms the predictions made in Sec. 3.2.1, of a more transient phase-matching at high pressures when $\eta_{\mathrm{fe}} \sim \eta_{\mathrm{fe}}^{\mathrm{mac}}$.

The slight difference in CE between the two branches is due to several factors. First, in the horizontal branch, the larger generation volume means that the variations in Δk_{foc} and Δk_{i} are more pronounced, which can decrease the overall degree of coherence. Secondly, the pulse duration in the above simulations may favor the vertical branch, simply because $\eta_{\mathrm{fe}}^{\mathrm{mac}}$ is reached closer to the peak of the pulse. In a shorter pulse, if the intensity is not simultaneously increased, phase-matching of the vertical branch can occur *after* the peak of the pulse, resulting in a lower CE. The CE is predicted to scale as τ^{-1} from recent analytical predictions [129], however the exact scaling may depend on which branch is considered.

As was shown in Fig. 3.4(c), the model predicts a trajectory-dependent phase-matching pressure which varies with the relative position of the medium and the fundamental beam focus. The position of the medium is known to affect the conversion efficiency, especially for the long trajectory [68, 178], and the position of the harmonic focus [179–181]. The simulated CE as a function of the medium length is shown in Fig. 3.10(a) for a medium centered at $-1z_{\mathrm{R}}$, and as a function of the medium position for a medium length of $0.2z_{\mathrm{R}}$ in Fig. 3.10(b). The model correctly describes the splitting in phase-matching pressure of the two trajectories. In Fig. 3.10(a) there is a discrepancy between the model and region of high CE for the long trajectory, possibly due to defocusing changing the contributions of Δk_{i} and Δk_{foc}, and/or off-axis phase-matching, leading to an effective phase-matching pressure which is lower than the prediction. A maximum CE is observed around $z = -0.6z_{\mathrm{R}}$ for the short and $z = -1.1z_{\mathrm{R}}$ for the long trajectory. We believe that at these positions, the dipole

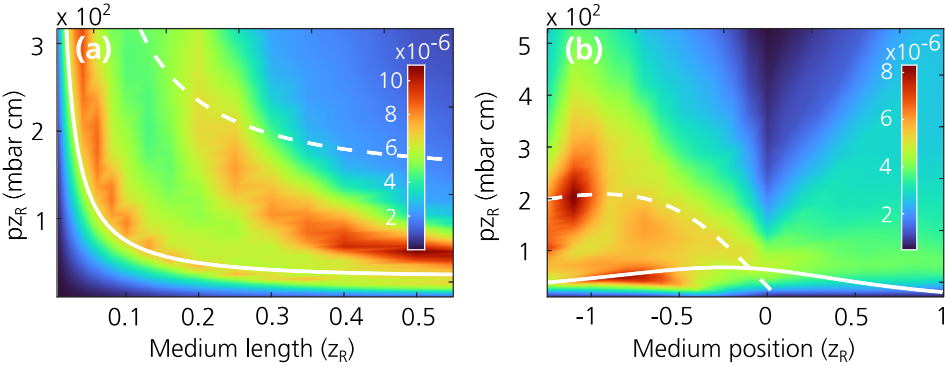

Figure 3.10: Position of the medium. Simulated conversion efficiency (colorscale) of the 23rd harmonic in argon for (a) a medium centered at $-1z_\mathrm{R}$ and (b) a medium of length of $0.2z_\mathrm{R}$. The white solid (dashed) line indicates the model prediction [Eq. (3.40)] for the short (long) trajectory.

phase-induced wave front cancels the focusing-induced wave front of the laser [179, 180], leading to optimized generation across the transverse direction. Because the dipole phase contribution is larger for the long trajectory, this position is located further from the focus than for the short trajectory.

3.4.2 Measuring the Hyperbola

Experimental optimization studies have often been performed in very limited pressure–length regions [32, 175, 182, 183], and many times the pressure is simply given as the backing pressure of the gas supply. In paper **II** our model is verified experimentally by systematically scanning a broad range of generation conditions, including the pressure (while measuring the pressure *inside* the gas cell), medium length, pulse energy and harmonic order. The results, shown in Fig. 3.11, were obtained at the gas HHG Sylos Long Beamline at ELI-ALPS [30, 184], and the Intense XUV Beamline at the Lund Laser Centre [137, 185].

Results from the pulse energy scan indicated in Fig. 3.11(a) confirm the position of the optimal pressure–length hyperbola and its independence with driving field intensity. In Fig. 3.11(b), a large pressure range is observed to yield a high CE for a short medium, while the long medium is much more sensitive to pressure changes. Finally, the spatial quality of the far-field beam profile is compared to simulations in Fig. 3.11(c), where the high-pressure regime has larger off-axis contributions. In general, the appearance of the off-axis radiation depends strongly on the generation conditions and harmonic order [discussed further in paper **II**].

To conclude, the hyperbolic model is shown through simulations and experiments to re-

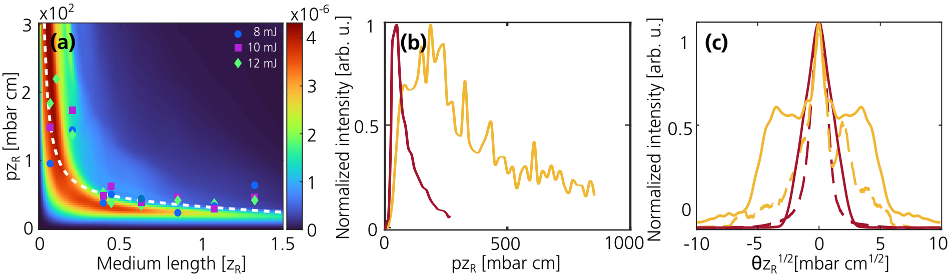

Figure 3.11: Experimental verification of hyperbola. (a) Simulated conversion efficiency (colorscale) of the 23rd harmonic in argon. Markers show the measured pressure corresponding to the highest yield for different medium lengths and pulse energies: $8\,$mJ (circles), $10\,$mJ (squares) and $12\,$mJ (diamonds). The model is indicated by the dashed line. (b) Intensity of the 19th harmonic as a function of medium pressure for a short $0.06\,z_\mathrm{R}$ (yellow) and long $0.85\,z_\mathrm{R}$ (red) medium. (c) Simulated (solid) and measured (dashed) far-field profile of the 23rd harmonic for a medium length of $0.06\,z_\mathrm{R}$ (yellow) and $1.33\,z_\mathrm{R}$ (red). The data have been acquired at the gas HHG Sylos Long beamline. Figure adapted from paper **II**.

main true for a wide range of focusing conditions, pressures, medium lengths, harmonic orders, intensities and gas species. The final choice of pressure and medium length depends on the requirements on spatio-temporal quality of the radiation for a specific application. In the next chapters, which concern measurements of attosecond photoionization dynamics using attosecond pulse trains obtained from HHG, a superior spatial and temporal quality is preferred. The generation of high-order harmonics is thus performed in the horizontal branch, with a medium length of approximately $0.5z_\mathrm{R}$ and pressures close to p_0.

Chapter 4

Attosecond Photoelectron Interferometry

As mentioned in Chapter 1, the ultrafast temporal dynamics of photoionization processes is encoded in the spectral phase of the complex amplitude of the EWP. Experimentally, the observable is the modulus squared of the complex amplitude, hence phase information is lost in a direct measurement of photoelectrons. In this work we use the RABBIT and KRAKEN photoelectron interferometry techniques. These techniques rely on path-interference induced by two-photon two-colour transitions to retrieve the spectral phase and amplitude of the wave function, or in the case of KRAKEN, that of the density matrix. The first part of this chapter briefly introduces the theoretical background of two-photon transitions. The following sections describe the theory of RABBIT and KRAKEN, in the case of both broadband excitation of a comb of harmonics, and narrowband excitation when a harmonic is tuned to an atomic resonance. Lastly, the experimental implementation of these techniques, as used in this thesis, is discussed.

4.1 Two-photon Transitions

Photoionization was already discussed in Sec. 3.3.1 when driven by strong fields. In the following treatment and in the RABBIT and KRAKEN experiments performed here, only one- and two-photon ionization is considered. The field intensities are thus kept low ($I_{\mathrm{IR}} \approx 10^{11}\,\mathrm{W\,cm^{-2}}$). Ionization is initiated by a bound electron absorbing a high energy XUV photon ($\hbar\Omega > I_{\mathrm{p}}$, where Ω is the harmonic photon angular frequency) after which it

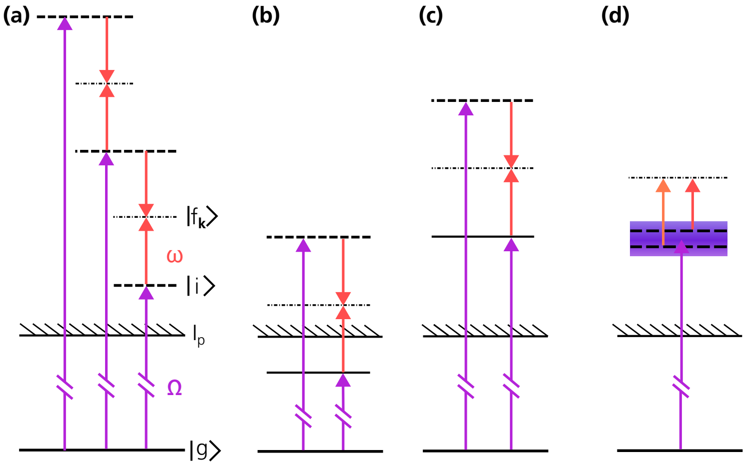

Figure 4.1: Two-photon transitions. Energy diagrams of two-photon ionization schemes studied in this thesis. (a) Broadband RABBIT used for extracting time delays in paper **V**. (b) Narrowband resonant energy-resolved below-threshold RABBIT used in paper **VI**. (c) Narrowband resonant energy-resolved RABBIT used to study Fano resonances in paper **VII**. (d) Ionization by a broad, single harmonic, as used in the KRAKEN protocol in papers **VIII** and **IX**. Purple (red) arrows denote XUV (IR) absorption. Bound and quasi-bound states are represented by solid black lines, while dashed and dot-dashed lines represent continuum states.

absorbs or emits an additional IR photon[1]. In the following the XUV photon is assumed to always be absorbed first. The reverse is possible, but the corresponding cross section is very small since the IR photon excites virtual states far from any resonance [186].

Both the XUV and IR fields are assumed to be linearly polarized along $\hat{z}$. Based on second order perturbation theory the two-photon transition matrix element going from an initial bound state $|g\rangle$ to a final continuum state $|f_{\mathbf{k}}\rangle$, characterized by a momentum $\mathbf{k}$, is [16]

$$M^{(\pm)}_{g\to f_{\mathbf{k}}}(\Omega) \propto \lim_{\epsilon\to 0^+} \sum\!\!\!\!\!\!\int_i \frac{\langle f_{\mathbf{k}}|\,\hat{z}\,|i\rangle\,\langle i|\,\hat{z}\,|g\rangle}{E_g - E_i + \hbar\Omega + \mathrm{i}\epsilon}, \tag{4.1}$$

where the energies of the initial and intermediate states are E_g and E_i, respectively, and the integral sum runs over all continuum and discrete intermediate states $|i\rangle$. The $\pm$ denotes that the IR transition can occur through either absorption $(+)$ or stimulated emission $(-)$. Energy diagrams of the two-photon pathways for the different cases studied in this thesis are shown in Fig. 4.1, and discussed in more detail in the following sections.

---

[1] In the resonant below threshold RABBIT ($\hbar\Omega < I_\mathrm{p}$) in Sec. 4.2.3 the ionization is initiated by the absorption of an additional IR photon.

The final two-photon transition amplitude depends on the amplitudes of the XUV and IR fields. For ultrashort pulses, the finite duration, and hence broad bandwidth of the XUV and IR fields means that every final state energy can be reached by several pairs of XUV and IR photon energies. The possible pairs must fulfill the energy conservation relation $\hbar\Omega + \hbar\omega_0 = E_{f_\mathbf{k}} - E_g = \hbar\Omega_{f_\mathbf{k}g}$. This leads to a convolution over the XUV and IR bandwidths, so that the transition amplitude is given by [187, 188]

$$A^{(\pm)}_{g\to f_\mathbf{k}}(\Omega_{f_\mathbf{k}g},\tau) = -\frac{\mathrm{i}e^2}{\hbar}\int_0^\infty \mathrm{d}\Omega\, E_\mathrm{IR}(\Omega_{f_\mathbf{k}g}-\Omega)\mathrm{e}^{\mathrm{i}(\Omega_{f_\mathbf{k}g}-\Omega)\tau}E_\mathrm{XUV}(\Omega)M^{(\pm)}_{g\to f_\mathbf{k}}(\Omega). \quad (4.2)$$

Note that the amplitude depends on the delay between the XUV and IR fields, since changing the delay alters the phase relation between the different contributions to the final state transition amplitude. The effect of the convolution of XUV and IR bandwidths on the transition amplitude and phase is explored experimentally in paper **VII**, and discussed further in Sec. 5.3.

4.2 Reconstruction of Attosecond Beating By Interference of Two-photon transitions (RABBIT)

In the RABBIT technique [15], an attosecond XUV pulse train consisting of odd-order harmonics of an IR field of frequency ω_0 leads to a PhotoElectron Spectrum (PES) with peaks spaced by $2\hbar\omega_0$. A weak, phase-locked copy of the IR field is spatially and temporally overlapped with the APT, leading to two-photon transitions and additional peaks in the PES called *SideBands* (SBs). The SBs are reached by two possible paths, absorption of harmonic HH_{q-1} plus absorption of an IR photon, or absorption of harmonic HH_{q+1} plus stimulated emission of an IR photon, as shown in Fig. 4.2(a). The interference of the two quantum pathways is sensitive to phase variations in the XUV and IR fields. By tuning the relative delay of the XUV and IR fields the intensity of SB_q oscillates as [189]

$$I_q = \left|A^{(+)}_{q-1}\right|^2 + \left|A^{(-)}_{q+1}\right|^2 + \left|A^{(+)}_{q-1}\right|\left|A^{(-)}_{q+1}\right|\cos(2\omega_0\tau - \Delta\Phi), \quad (4.3)$$

where $A^{(\pm)}_{q\mp1}$ are two-photon transition amplitudes for absorption of harmonic $q\mp1$ and the superscript $(\pm)$ indicates that an additional IR photon is absorbed (+) and emitted (-). An example of a RABBIT delay scan is shown in Fig. 4.2(b). The SB phase is given by $\Delta\Phi = \Delta\Phi_\mathrm{XUV} + \Delta\Phi_\mathrm{A}$, where the former is related to the XUV group delay τ_XUV, *i.e.*, the spectral integral of the attochirp in Eq. (2.17), given by

$$\Delta\Phi_\mathrm{XUV} = \arg\left[E_\mathrm{XUV}(\Omega_{q+1})\right] - \arg\left[E_\mathrm{XUV}(\Omega_{q-1})\right] \approx 2\omega_0\tau_\mathrm{XUV}, \quad (4.4)$$

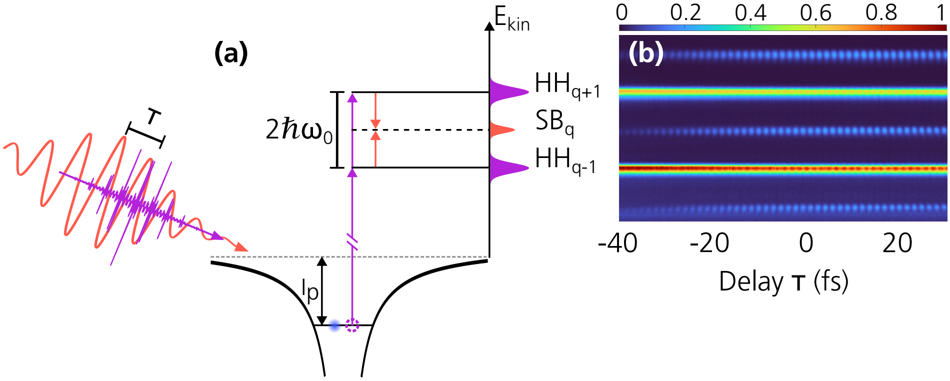

Figure 4.2: Principle of RABBIT. (a) Temporally overlapping XUV APT (purple) and femtosecond IR pulse (red) ionize electrons by two-photon transitions. The odd high-order harmonic (HH) comb leads to a photoelectron spectrum with peaks spaced by $2\hbar\omega_0$. Absorption or emission of an additional IR photon leads to formation of sidebands (SB). (b) RABBIT trace showing photoelectron peaks at the harmonic and SB energies, oscillating as a function of the XUV–IR delay τ.

and the latter is the atomic phase difference

$$\Delta\Phi_{\mathrm{A}} = \arg\left[M^{(-)}_{g\to f_{\boldsymbol{k}}}(\Omega_{q+1})\right] - \arg\left[M^{(+)}_{g\to f_{\boldsymbol{k}}}(\Omega_{q-1})\right], \tag{4.5}$$

which contains information about the electron dynamics of the ionization process.

By fitting the SB oscillations visible in Fig. 4.2(b) to the form given in Eq. (4.3) it is then possible to determine the relative phase of the different quantum paths. If the atomic phase is assumed small, which is a good approximation in a featureless continuum, the XUV group delay can be extracted, and the average temporal profile of the pulses in an APT can be reconstructed as demonstrated by Paul *et al.* in 2001 [15]. On the other hand, if the XUV phase is well known, ionization dynamics can be inferred from the spectral variation of the atomic phase. This has been the main application of the RABBIT technique in the past two decades.

4.2.1 Measuring Photoionization Time Delays using RABBIT

The theory of photoionization time delays has been studied extensively, in for example Ref. [190–192], and will not be covered in detail here. Instead, the basic idea is presented below.

When a bound electron is ionized by a broadband pulse, such as an XUV harmonic comb as shown in Fig. 4.1(a), a broad EWP is emitted. As the EWP propagates away from its

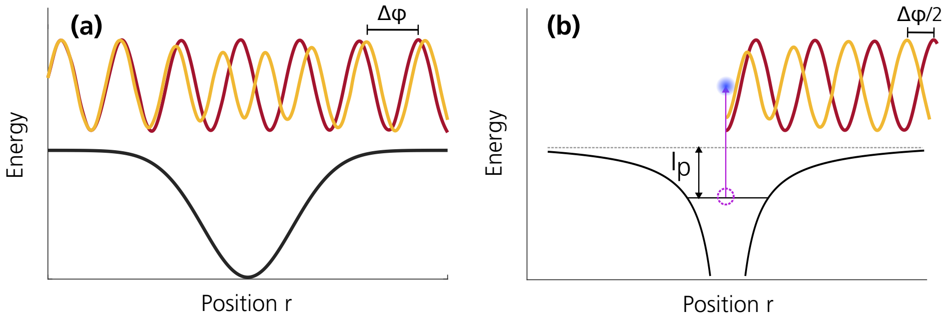

Figure 4.3: Scattering time delays. (a) Comparison of propagation of a free electron wave (yellow) to a wave scattering off an attractive potential (red). (b) Photoionization of an electron corresponding to a half-scattering event. The potential is shown in black. The phase of the scattering electron varies more rapidly close to the potential, leading to a phase advance, $\Delta\Phi$, compared to the free electron.

parent ion, it is affected by the radially varying attractive ionic potential, leading to an energy-dependent phase shift and a group delay of the EWP. The theory of such phase shifts was first developed for scattering processes by Eisenbud, Wigner and Smith [193]. It has since been extended to the case of photoionization [22], which can be regarded as a half-scattering process as illustrated in Fig. 4.3, with half the phase shift, since the electron in the case of ionization propagates starting from $r = 0$.

In the case of ionization to a single continuum channel, the atomic phase difference appearing in the SB oscillation in Eq. (4.3) can be related to a Wigner-like scattering time delay, τ_{W}, by decomposing it as $\Delta\Phi_{\mathrm{A}} = \Delta\eta + \Delta\Phi_{\mathrm{cc}}$, where $\Delta\eta \approx 2\omega_0\tau_{\mathrm{W}}$ is the difference in scattering phase between the absorption and emission path, and $\Delta\Phi_{\mathrm{cc}} \approx 2\omega_0\tau_{\mathrm{cc}}$ is an additional "continuum-continuum" phase difference due to the interaction with an additional IR photon. Inserting these expressions in the expression for I_q in Eq. (4.3), the oscillating term becomes proportional to $\cos\left[2\omega_0(\tau - \tau_{\mathrm{W}} - \tau_{\mathrm{cc}} - \tau_{\mathrm{XUV}})\right]$.

A relative Wigner time delay can then be extracted from a RABBIT spectrogram given the elimination, or prior knowledge, of τ_{cc} and τ_{XUV}. In practice this can be achieved by comparing two simultaneous measurements in, *e.g.*, different gases [194, 195], or from different ionization processes [16, 22], where one of the measurements acts as a phase reference. Furthermore, if one of the two measured processes is known to high accuracy from theoretical calculations, an approximate absolute time delay of the other process can be extracted [196]. In paper **V** we measure absolute ionization time delays in xenon by using neon as a reference.

4.2.2 Rainbow RABBIT

In the original application of the RABBIT technique to the reconstruction of the temporal profile of attosecond pulses, and in the measurements of ionization time delays, the spectral phase is assumed to take a single value for each SB. This is equivalent to integrating the photoelectron signal across the spectral width of each SB. Using high-resolution photoelectron detectors the spectral phase across a SB can be resolved, and a cosine fit can be made to each energy bin in a SB. This technique, dubbed "rainbow" RABBIT was introduced by Gruson *et al.* [19]. It can be particularly useful to study sharp spectral features appearing within a SB due to resonances in the intermediate state in the two-photon transition.

4.2.3 Resonant RABBIT

In the section on time delays, creation of an EWP through photoionization was considered in the case with no bound states, or *resonances*, in the intermediate and final continua. In that context, ionization time delays are well defined. In conditions when there is a sharp resonance which is coupled to the final continuum, the resulting rapid variation in spectral phase can lead to strong reshaping of the EWP. In such conditions the Wigner-like delay is no longer well defined [197]. Nevertheless, valuable information about electron correlations and even the full temporal build-up of the EWP through the resonance can still be extracted [19].

If the phase induced by the resonance is dominant, it can be extracted from interference with a non-resonant quantum path, as shown for two different RABBIT schemes in Fig. 4.1(b,c). The attochirp and the non-resonant path scattering phases entering $\Delta\Phi$ are approximately constant across the narrow spectral widths considered [19], however the femtochirp must sometimes be taken into account. In particular when harmonics have been generated in the presence of plasma blue-shifting [198], or, as will be shown in the discussion of KRAKEN measurements in Sec. 5.4, when the probe IR frequency differs from the central IR frequency in the HHG process.

The first example of resonant RABBIT in Fig. 4.1(b), called "below-threshold RABBIT", corresponds to the case when the energy of the harmonic in the absorption path is below the ionization threshold, and tuned to be resonant with a Rydberg state of the atom. The presence of the dressing IR field leads to ionization by absorption of an additional IR photon. The theory of below-threshold RABBIT is described in detail in paper **VI**. The experiment consists in measuring the π-phase jumps when the denominator in Eq. (4.1) goes to zero at resonance, and when the numerator changes sign in between two Rydberg states. In the second example, illustrated in Fig. 4.1(c), the resonance is located above the first ionization threshold and can decay by autoionization to the continuum. This case is investigated in paper **VII** and treated in detail below.

4.2.4 Fano Resonances

When the ionizing photon energy is tuned to a quasibound state which is coupled to an open ionization channel, the excited bound state can decay through autoionization to the continuum. This leads to two possible quantum paths to the same final energy, as sketched in Fig. 4.4(a). The resulting interference of the autoionizing and direct ionization channels can be observed as a characteristic asymmetric *Fano lineshape*, named after Ugo Fano who described it theoretically [199].

Following the Fano formalism [199], the eigenstates of the one-photon interaction can be partitioned into a sum of the bound state $|\alpha\rangle$ and continuum states $|\beta\rangle$ as

$$|\Psi_E\rangle = \alpha\,|\alpha\rangle + \int \mathrm{d}E'\,\beta_{E'}\,|\beta_{E'}\rangle\,, \tag{4.6}$$

The one photon dipole transition amplitude from a ground state $|g\rangle$ to the eigenstate $|\Psi_E\rangle$ can then be expressed as

$$\langle\Psi_E|\,\hat{z}\,|g\rangle = \langle\beta_E|\,\hat{z}\,|g\rangle\,\frac{q+\epsilon}{\epsilon+\mathrm{i}}, \tag{4.7}$$

where $\epsilon = 2(E - E_\alpha)/\Gamma$ is the reduced energy, E_α is the resonance energy, $\Gamma = 2\pi|V_E|^2$ is the width of the resonance and V_E describes the configuration interaction between the bound and continuum states. The Fano q-parameter is a real number which depends on the relative strength of the resonant excitation and direct ionization paths and is given by

$$q = \frac{\langle\alpha|\,\hat{z}\,|g\rangle}{\pi V_E^*\,\langle\beta_E|\,\hat{z}\,|g\rangle}. \tag{4.8}$$

The fraction on the right hand side in Eq. (4.7) is called the resonance factor, $R(\epsilon) = (q+\epsilon)/(\epsilon+\mathrm{i})$, and defines the amplitude and phase variation across the resonance assuming that the other quantities vary slowly with the energy. In the presence of a Fano resonance the non-resonant absorption cross section σ_0 is modified by the absolute square of the resonance factor resulting in the Fano profile,

$$\sigma(\epsilon) = \sigma_0\frac{(q+\epsilon)^2}{\epsilon^2+1}. \tag{4.9}$$

To extract information about temporal dynamics also requires the phase to be measured.

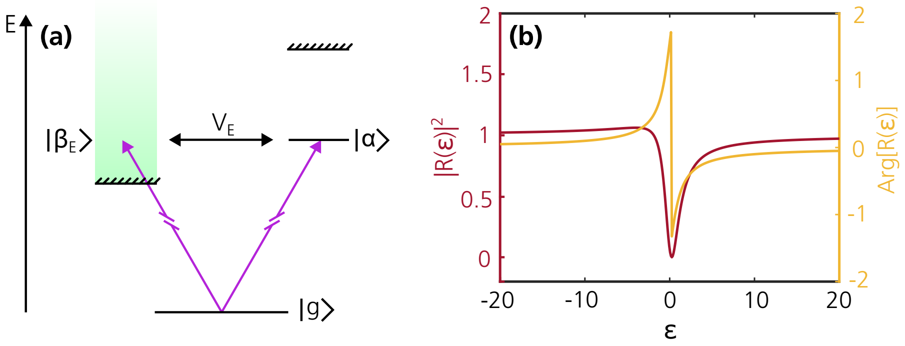

Figure 4.4: Fano resonances. (a) Energy diagram of a quasi-bound state $|\alpha\rangle$ embedded in the continuum $|\beta_E\rangle$. A high energy photon (purple) prepares the system in a superposition of discrete and continuum states, which are coupled through the configuration interaction V. (b) Squared amplitude (red) and phase (yellow) of the Fano resonance factor $R(\epsilon)$ for $q = -0.25$ and $\Gamma = 76$ meV.

The phase of the resonance factor is

$$\arg[R(\epsilon)] = \frac{\pi}{2} + \arctan\epsilon - \pi\Theta(\epsilon + q), \tag{4.10}$$

where Θ is the Heaviside function. The absorption cross section and phase of the resonance factor are shown in Fig. 4.4(b) for $q = -0.25$ and $\Gamma = 76\,\mathrm{meV}$, representing the $3\mathrm{s}^1 3\mathrm{p}^6 4\mathrm{p}$ (denoted $3\mathrm{s}^{-1}4\mathrm{p}$ in the following) Fano resonance in argon. The resonance is a window resonance, with a cross section which drops to zero at $\epsilon = -q$. The phase slowly increases from zero, until $\epsilon = -q$, at which point it displays a sharp $-\pi$ phase jump, followed by a slow increase back to zero.

In the above, a single interacting continuum is assumed. In paper **VII**, we study the $3\mathrm{s}^{-1}4\mathrm{p}$ Fano resonance in argon, which is characterized by autoionization into two continua, an s- and a d-channel. In that case, it is possible to describe the continuum states in Eq. (4.6) as a sum of an interacting and a non-interacting continuum. The two-photon transition matrix element going from the ground state to a resonant sideband [*Cf.* Fig. 4.1(c)] then takes the form [18, 199]

$$M_{g\to f_{\mathbf{k}}} = M^{(\mathrm{i})}_{g\to f_{\mathbf{k}}} \frac{q+\epsilon}{\epsilon + \mathrm{i}} + M^{(\text{n-i})}_{g\to f_{\mathbf{k}}}, \tag{4.11}$$

where the first term multiplied by the resonance factor describes the interacting part and the second term adds a background. The phase variation is contained in the first term, as the background term phase is flat.

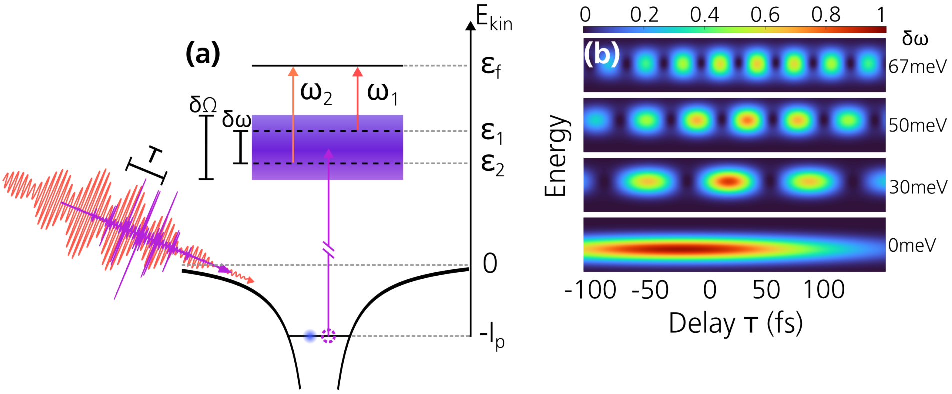

Figure 4.5: Principle of KRAKEN. (a) An EWP is created by a fs XUV pulse of width $\delta\Omega$. A bichromatic probe of frequencies ω_1 and ω_2 spaced by $\delta\omega$ interferes the EWP with itself. (b) Simulated photoelectron spectra for different values of $\delta\omega$ as a function of the XUV–IR delay. Figure adapted from paper **VIII**.

4.3 Quantum State Tomography of Attosecond Electron Wave Packets

In the previous examples of applications of the RABBIT technique, a single channel was assumed when expressing phase variations. However, when multiple channels are present and cannot be disentangled, the PES is the result of an incoherent sum of the different channels. In that case, the measured phase cannot be related to individual channels, unless one channel is dominant [200–202]. In the above, the first case corresponds to an EWP described by a *pure* quantum state, while the second case describes a *mixed* state. Mixed quantum states can result from decoherence processes such as interactions with the environment, or from measurements which by design do not measure all degrees of freedom. On the atto- and femtosecond timescales considered here, couplings to the environment are typically small. However, in a photoionization event, if the ion is not measured and ionic and electronic degrees of freedom are entangled, the measured reduced system of the photoelectron is described by a mixed state.

The reliance of the RABBIT technique on a wave function description generally makes it insufficient for mixed states, where a density matrix formalism of the quantum state is needed. To reconstruct the density matrix of a mixed state requires Quantum State Tomography (QST) techniques. Such techniques have recently been developed and applied in attosecond science [26, 27, 203]. In paper **VIII** a continuous variable QST protocol for photoelectrons is developed. This protocol, called KRAKEN, is summarized in this section.

The KRAKEN scheme, illustrated in Fig 4.5(a), is conceptually similar to RABBIT (*Cf.*

Fig. 4.2). Instead of interfering two consecutive harmonics in a sideband, a femtosecond XUV pulse from a single harmonic is temporally and spatially overlapped with a bichromatic IR probe. The broadband XUV creates an EWP with spectral width $\delta\Omega$ and the bichromatic probe, consisting of two narrow peaks with central frequencies ω_1 and ω_2 (where $\delta\omega = \omega_2 - \omega_1$), leads to two quantum paths to the same final state $|\epsilon_f\rangle$. Information about the coherences of the EWP is contained in the delay sensitive oscillations, induced by quantum path interference, of the photoelectron signal. The photoelectron signal oscillates with the frequency $\delta\omega$ when the delay τ between the bichromatic probe and XUV pulse is changed, as shown in Fig. 4.5(b).

In density matrix notation the signal at a final energy ϵ_f following a two-photon XUV+IR transition is expressed as $S(\epsilon_f, \tau, \delta\omega) = \langle\epsilon_f|\,\hat{\rho}_{\text{XUV+IR}}(\tau, \delta\omega)\,|\epsilon_f\rangle$, where $\hat{\rho}_{\text{XUV+IR}}$ is the photoelectron density operator after absorbing an additional IR photon. In general, we are interested in the density matrix after absorption of just the XUV. It can be shown (a detailed derivation is given in paper **VIII**) that the signal can be approximated in terms of the single-photon XUV density matrix as

$$\begin{aligned}S(\epsilon_f, \tau, \delta\omega) \approx \left|M_{\epsilon_f,\epsilon_1}\right|^2 \rho_{\text{XUV}}(\epsilon_1, \epsilon_1) &+ \left|M_{\epsilon_f,\epsilon_2}\right|^2 \rho_{\text{XUV}}(\epsilon_2, \epsilon_2)\\ &+\mathrm{e}^{\mathrm{i}\delta\omega\tau} M_{\epsilon_f,\epsilon_1} M^*_{\epsilon_f,\epsilon_2} \rho_{\text{XUV}}(\epsilon_1, \epsilon_2)\\ &+\mathrm{e}^{-\mathrm{i}\delta\omega\tau} M_{\epsilon_f,\epsilon_2} M^*_{\epsilon_f,\epsilon_1} \rho_{\text{XUV}}(\epsilon_2, \epsilon_1),\end{aligned} \tag{4.12}$$

where $M_{\epsilon_f,\epsilon_i}$ $(i = 1, 2)$ are dipole transition matrix elements between $|\epsilon_i\rangle$ and $|\epsilon_f\rangle$. The first two terms correspond to diagonal elements of the density matrix, *i.e.* populations, and the last two terms are off-axis elements corresponding to the coherences. The exponential term which multiplies the coherences represents an oscillation at frequency $\delta\omega$ when the XUV–IR delay is changed. The coherences can then be isolated by performing a Fourier transform along the delay axis and selecting components at $\pm\delta\omega$. By repeating delay scans for multiple values of $0 < \delta\omega < \delta\Omega$ the full density matrix can be reconstructed.

The results of the KRAKEN protocol are compared to direct calculations of the density matrix around the $3s^{-1}4p$ Fano resonance in argon in Fig. 4.6(a-d). Destructive interference from the resonance is observed as a cross in the amplitude and phase, and the presence of two spin–orbit (S–O) split continua ($^2P_{1/2}$ and $^2P_{3/2}$) produces two shifted copies of the Fano resonance in the density matrix.

In the above case of argon the two S–O split final ionic states leads to entanglement between the photoelectron and photoion. Because the ion is not measured, and the ionic state is entangled with the photoelectron, the reduced density matrix of the photoelectron describes a mixed state. The electron density matrix is $\rho_{\text{electron}} = p_{1/2}\rho_{1/2} + p_{3/2}\rho_{3/2}$, with p_i the probability amplitudes of the S–O components ($p_{1/2} = 1/3$ and $p_{3/2} = 2/3$). To quantify to what extent a state is mixed the measure of *purity* is often used. The purity of the S–O

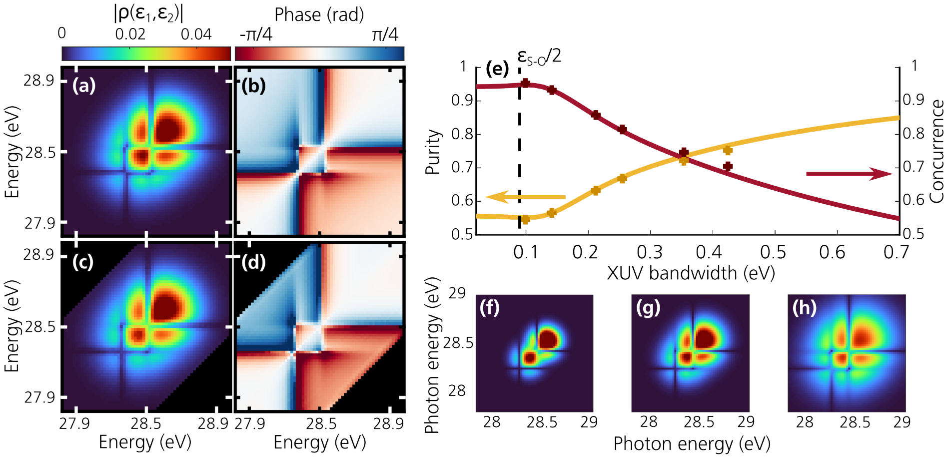

Figure 4.6: Density matrix reconstruction and ion-electron entanglement. Amplitude and phase of the density matrix of the $3s^{-1}4p$ Fano resonances in argon from (a,b) direct calculations and (c,d) KRAKEN. (e) Purity (yellow) and concurrence (red) from direct calculations (lines) and from KRAKEN (crosses). (f-h) Amplitude of the density matrix for XUV bandwidths $0.14\,\mathrm{eV}$ $0.21\,\mathrm{eV}$ and $0.35\,\mathrm{eV}$. Figure adapted from paper **VIII**.

split state is

$$\gamma = \mathrm{tr}[\rho^2_{\mathrm{electron}}] = p^2_{1/2} + p^2_{3/2} + 2p_{1/2}p_{3/2}\mathrm{tr}[\rho_{1/2}\rho_{3/2}], \tag{4.13}$$

where the last term depends on the spectral overlap integral of the two S–O components. This overlap depends on the bandwidth of the XUV pulse and on the S–O splitting, which in argon is relatively small ($\Delta\epsilon_{\mathrm{S–O}} = 177\,\mathrm{meV}$). For a bipartite system, if all other sources of decoherence are negligible, the purity is related to a quantity called the *concurrence* [204]

$$\mathcal{C} = \sqrt{2(1 - \mathrm{tr}[\rho^2_{\mathrm{XUV}}])}, \tag{4.14}$$

which is a measure of the degree of entanglement. By changing the XUV bandwidth the degree of purity, or equivalently entanglement, can then be controlled, which is shown in Fig. 4.6(e). In Fig. 4.6(f-h) the density matrix amplitude for three XUV bandwidths is shown. When the bandwidth is small, there is no spectral overlap between S–O components, and the coherences decay rapidly on the diagonal. This corresponds to a maximally entangled state. The KRAKEN protocol is implemented experimentally in paper **IX** and covered further in Sec. 5.4.

4.4 Experimental Methods

Measuring a RABBIT trace experimentally requires the PES to be recorded for many different values of the pump–probe delay τ using an optical interferometer. The $2\omega_0$ oscillation period of the sideband signal for an 800 nm fundamental wavelength is roughly 1.33 fs. To resolve the oscillations and collect enough data requires fine control of the pump–probe delay on the attosecond timescale, corresponding to a relative path length difference on the nanometer scale, often for several hours. Both collinear [205, 206] and noncollinear [207, 208] interferometer designs have been successfully implemented with attosecond stability. Collinear interferometers, such as the one implemented in paper **III**, are intrinsically stable because the pump and probe share the same propagation path. Noncollinear interferometers can be more versatile, and offer longer delay scan ranges, but are prone to delay jitter due to vibrations and drifts which negatively affects the RABBIT measurements [209]. This problem is solved by active stabilization of the path length difference of the interferometer arms.

During the scope of this work, the laser and XUV beamline (disscused in Sec. 2.3) were upgraded from 1 kHz to 3 kHz. In parallel with this, a new interferometer design was also implemented, to provide better long-term stability of the setup. The setup was used for the high-resolution RABBIT measurements in papers **VI** and **VII** and the KRAKEN measurements in paper **IX**. Below follows a description of the new setup. A detailed characterization is presented in paper **IV**. The old setup, described further in Ref. [210], was used in paper **V** and for the angle-resolved measurements in paper **VI**.

4.4.1 Setup: RABBIT

A sketch of the new optical interferometer and photon and electron detectors is shown in Fig. 4.7. The setup is based on a Mach-Zehnder interferometer, starting with a Beam Splitter (BS) which transmits 60% of the energy to the probe arm, and reflects 40% to the pump arm. The pump arm contains a Motorized Stage (MS) for coarse delay adjustment on the femtosecond timescale. A holey mirror removes the central part of the beam. The outer part is focused ($f = 50$ cm) into a gas cell in the generation chamber to drive HHG[2], as described in Sec. 2.3.2. The probe is focused by a 50 cm focal length mirror to match the wavefront of the pump arm at the common refocusing optic, a gold coated toroidal mirror ($f = 30$ cm), which focuses both the probe and XUV beams, in a $2f$-$2f$ configuration, into the interaction region of a photoelectron detector, here a Magnetic Bottle Electron Spectrometer (MBES). The focusing mirror in the probe arm is mounted on a piezoelectric stage (AS) for control of the pump-probe delay with attosecond precision.

---

[2] Conditions correspond to the horizontal branch of HHG, with $L_{\mathrm{med}} \approx 0.5 z_{\mathrm{R}}$ and pressures close to p_0.

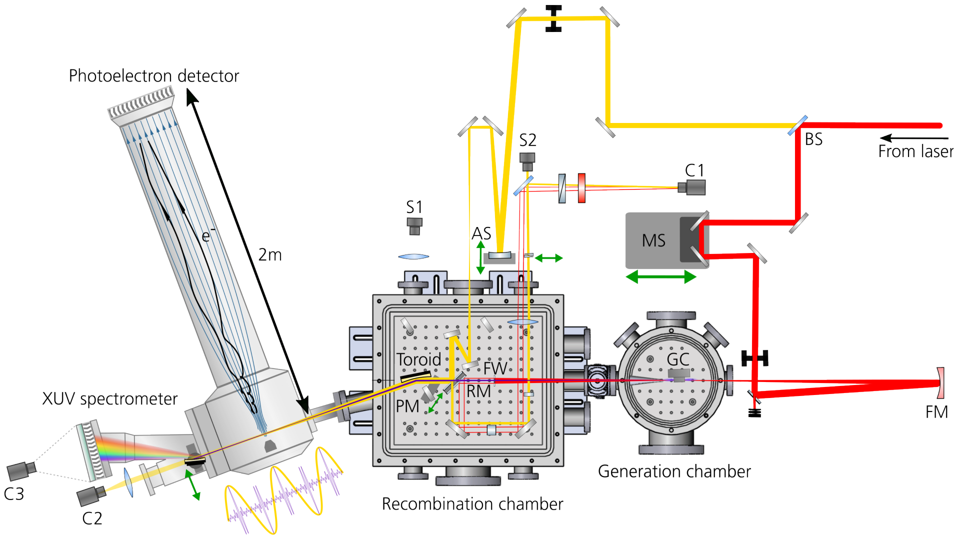

Figure 4.7: Schematic of the experimental setup used in RABBIT measurements. A beam splitter (BS) transmits 60% to the probe (yellow) and reflects 40% to the pump (red) arms. The XUV is shown in purple. MS, femtosecond scale motorized delay stage; AS, attosecond scale piezoelectric stage; GC, gas cell; FW, filter wheel; RM, recombination mirror; PM, pick-up mirror; C1, C2, C3 cameras; S1, S2, IR spectrometers. Some elements of the active stabilization scheme are presented in more detail in Fig. 4.8. Figure adapted from paper **IV**.

A detailed view of the recombination step and active stabilization scheme is presented in Fig. 4.8(a). In the pump arm, the remaining central part of the IR, not cut by the holey mirror, is blocked by a metallic foil mounted on a holey fused silica plate in a *Smaract* rotation wheel [Fig. 4.8(b)]. The outer part of the pump IR pulse is transmitted through the fused silica plate while the XUV pulse train is transmitted through the metallic foil, inducing an optical path length difference, indicated by the delay $\Delta\tau_1$. The pump and probe IR pulses and the XUV pulse train are recombined on a Recombination Mirror (RM) mounted in a *Polaris* mirror mount with piezoelectric adjusters. When the metallic foil is rotated out, the central part of the pump and outer part of the probe can either be reflected onto a spectrometer (S1) by inserting a pick-up mirror (PM), or be allowed to propagate through the interaction chamber and be focused onto a camera (C2) when the concave grating used for the XUV spectrometer, is moved out of the beam path. In the first case, using the coarse motorized stage, the resulting spectral interference fringes can be used to find the temporal overlap ($\tau = 0$) in the application chamber[3]. In the latter case, the spatial overlap of the pump and probe beam foci in the interaction region are monitored

---

[3] Down to an error of ~ 100 as resulting from the optical path length difference between XUV propagating through the metallic foil and in vacuum. In practice a quick delay scan is then used to find the $\tau = 0$.

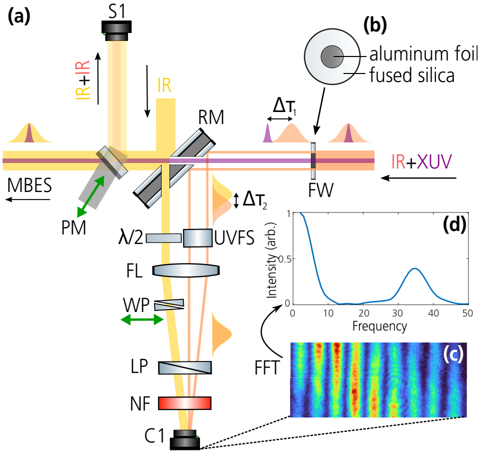

Figure 4.8: Detailed sketch of the active stabilization of the Mach-Zehnder interferometer. (a) Optical setup with pump and probe IR beams shown in red and yellow, respectively. The XUV is shown in purple. FW, filter wheel; RM, recombination mirror; UVFS, UV fused silica block; $\lambda/2$, half-waveplate; FL, focusing lens; WP, wedge pair; LP, linear polarizer; NF, narrowband filter; PM, pick-up mirror; C1, camera; S1, spectrometer. (b) Sketch of metallic filter mounted on holey fused silica plate. (c) Spatial fringes recorded on C1. (d) FFT of spatial fringes. Figure adapted from paper **IV**.

on C2 and fine-tuned using the piezoelectric adjusters of the RM[4].

The part of the pump which is reflected by the RM, and the transmitted part of the probe, are then used to actively stabilize the interferometer. The thickness of the RM, L_{RM}, results in an additional path length difference between the pump and probe beams in the stabilization arm, equal to $2\sqrt{2}L_{\mathrm{RM}}$ and consequently a delay $\Delta\tau_2$. This delay, and the delay from the fused silica plate, are compensated by a block of UV fused silica in the pump beam and a wedge pair in the probe beam. Furthermore, the filter wheel consists of two separate rotation stages, and by tuning the wedge pair thickness the final delay can be tuned to account for either one or two filters being used. After the RM, the pump and probe beams are shifted transversely, so that when they are focused by a lens (FL) onto a camera (C1), they give rise to spatial fringes, as shown in Fig. 4.8(c). To optimize the fringe contrast, the probe beam polarization is rotated by a $\lambda/2$-plate, and a Wollaston prism (LP) is used to control the relative intensity of the pump and probe. The spatial frequency and phase is identified through a fast Fourier transform [Fig. 4.8(d)], and a PID-controller is used to feedback an error signal, *i.e.* the difference in the measured phase and the desired phase, to the piezoelectric translation stage (AS in Fig. 4.7). The stability of the interferometer has been measured to around 13 as Root-Mean-Square (RMS) error over several hours. Finally,

---

[4] In reality it is of course the XUV, rather than the pump IR, one would like to overlap with the probe. With proper alignment the XUV and pump IR beams are, however, propagating collinearly.

a 10 nm narrowband filter (NF) is used to extend the pulse overlap duration, which gives a delay scan range of up to 400 fs.

By stabilizing directly to the phase relation of the pump and probe femtosecond laser pulses, as opposed to using a copropagating CW HeNe laser [208], the above scheme is more versatile. In resonant RABBIT experiments, such as those performed in paper **VII**, an additional 10 nm narrowband filter is placed in the probe arm before the focusing mirror. The narrow bandwidth of the probe leads to a reduction of mixing of different spectral components in the sideband signal, greatly improving the spectral phase resolution in rainbow RABBIT measurements [202].

4.4.2 Photoelectron Detectors

The XUV pulse train and IR probe pulse are focused into a gas target, where one- and two-photon ionization events occur. Detection of the resulting photoelectrons is done using photoelectron spectrometers. In this work, two types of photoelectron spectrometers are used, a magnetic bottle electron spectrometer [211], and a Velocity Map Imaging Spectrometer (VMIS) [212]. These detector types have different, complementary, strengths and weaknesses. The MBES provides a high signal and superior energy resolution at the cost of loss of angular information of the photoionization event, while the VMIS has much worse energy resolution, but is able to angularly resolve the photoelectron emission. Here, a brief description of these two detectors is provided.

Magnetic Bottle Electron Spectrometer

An MBES is a Time-of-Flight (ToF) spectrometer, relying on measuring the time it takes for electrons to travel a certain distance. A schematic of the MBES used in this work is shown in Fig. 4.9(a). Photoionization occurs in a continuous effusive gas jet in the overlap region of the XUV and IR probe foci. Photoelectrons are guided into a flight tube by a combination of strong and weak magnetic fields. A conically shaped NdFeB magnet placed close to the gas jet generates a strong, inhomogenous, magnetic field (100 to 1000 mT) in the interaction region, acting as a magnetic mirror, reflecting electrons and parallelizing their trajectories towards the flight tube and provides 4π sr collection efficiency. A solenoid wrapped around the flight tube produces a weak, homogenous, magnetic field (0.1 to 10 mT depending on the application) along the length of the 2 m long tube. The combined fields force the electrons into helical trajectories around the magnetic field lines, which run parallel to the flight tube, thus guiding the electrons to the MCP detector. A mu-metal casing around the flight tube shields the electrons from disturbances caused by the earth's magnetic field.

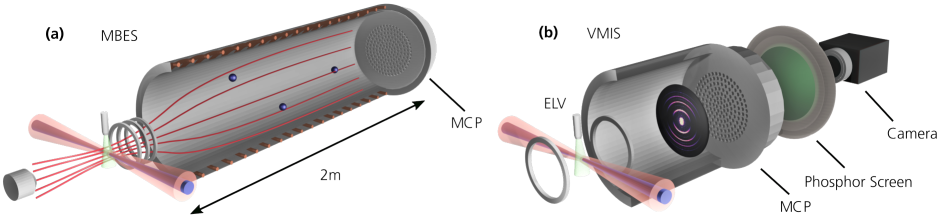

Figure 4.9: Sketch of the photoelectron spectrometers used in this work. (a) Magnetic Bottle Electron Spectrometer (MBES), used in papers **IV**, **V**, **VI**, **VII**, **IX**. (b) Velocity Map Imaging spectrometer (VMIS), used in paper **VI**. Figure adapted from paper **VI**.

To measure the ToF, a photodiode at the laser output generates a start signal. When an electron hits the MCP detector, it is multiplied through a cascade of collisions. The resulting signal, sent to a data acquisition card, acts as the stop signal, and the time difference gives the ToF[5]. Since XUV radiation generated through HHG is typically well below the keV range[6], electrons ionized by APTs can be treated classically. The flight time of an electron can then be used to extract the kinetic energy, E_k, through

$$E_\mathrm{k} = \frac{m_e}{2}\left(\frac{L+\gamma}{t_\mathrm{ToF}}\right)^2, \tag{4.15}$$

where L is the length of the flight tube, γ is a calibration parameter and t_ToF is the time-of-flight. The sampling rate of the data acquisition card, $f_\mathrm{DAQ} = 1/\delta t$, sets a lower limit on the time difference between two electrons impacting the detector which can be measured separately. This in turn leads to a limit of the energy resolution of the MBES, which can be expressed as $\delta E \propto L^2 t_\mathrm{tof}^{-3}\delta t$. From this expression, it is clear that a longer flight tube increases the energy resolution, and that the resolution varies with the ToF, and hence with E_k. A common measure of the resolution of an MBES is given by $\delta E/E \propto \delta t/t_\mathrm{TOF}$, which describes how the resolution varies with the kinetic energy. Since the resolution is higher for lower kinetic energies, a variable retarding potential is applied along the flight tube, to slow down fast electrons. The MBES used in this work has a resolution of $\delta E/E \approx 2\,\%$ at 1 to 2 eV, at which point the integration of electrons ionized from a finite interaction volume starts to limit the resolution. At higher energies, the resolution is further limited by the interaction of the electrons with the strong magnetic field in the interaction region. Two electrons ionized with the same kinetic energy, with one traveling in the direction of the tube, and one in the opposite direction, towards the magnet, result in a significant

---

[5] After accounting for any additional electronic signal delays.

[6] Recent work has however demonstrated up to 5 keV harmonics generated from multiply ionized plasmas [213],

flight time difference due to the extra time it takes for the latter electron to be repelled by the magnet and guided into the flight tube. This leads to an apparent spread of electron kinetic energies, which becomes larger for higher kinetic energies. These limiting effects are collectively described by the Point Spread Function (PSF) of the detector.

Velocity Map Imaging Spectrometer

The collection and parallelization of electrons in the flight tube of an MBES necessarily leads to integration over all angular degrees of freedom. To fully characterize photoelectron emission, including the angular momentum channel interferences [201], requires the angular channels to be resolved. This can be achieved by using a VMIS. A schematic of a VMIS used in paper **VI** is shown in Fig. 4.9(b), where gas is supplied through an Even Lavie valve positioned between two electrodes (a repeller and extractor). The electrodes push electrons from the interaction region towards an MCP detector at the end of a short flight tube ($\approx$ 35 cm). Contrary to the MBES, the voltages on the electrodes in a VMIS allow the Photoelectron Angular Distribution (PAD) to expand freely in space, so that the 3-dimensional momentum distribution is projected on the 2-dimensional (2D) phosphor screen placed behind the MCP. The 2D image on the phosphor screen is then imaged by a CCD camera.

Because of the free expansion, photoelectrons with kinetic energy E_k form a disk of radius

$$r = \sqrt{\frac{L^2 E_\mathrm{k}}{eV}}, \tag{4.16}$$

where L is the length of the flight tube and V is the difference in voltage between the electrodes. To retrieve the 3D PAD requires to use an inverse Abel transform algorithm. In paper **VI** the cylindrical symmetry of the PAD around the polarization axis allows for a method known as pBASEX [214] to be used. The pBASEX method exploits the property that any cylindrically symmetric angular distribution can be decomposed as a sum of Legendre polynomials as

$$\frac{\mathrm{d}\sigma}{\mathrm{d}\Omega} = \frac{\sigma_0}{4\pi}\left[1 + \sum_{i=1}^{\infty} \beta_i P_i(\cos\theta)\right], \tag{4.17}$$

where σ is the photoelectron differential cross section, Ω is the solid angle, σ_0 is the total cross section, β_i are the asymmetry parameters, P_i is the i^{th} order Legendre polynomial and θ is the polar angle.

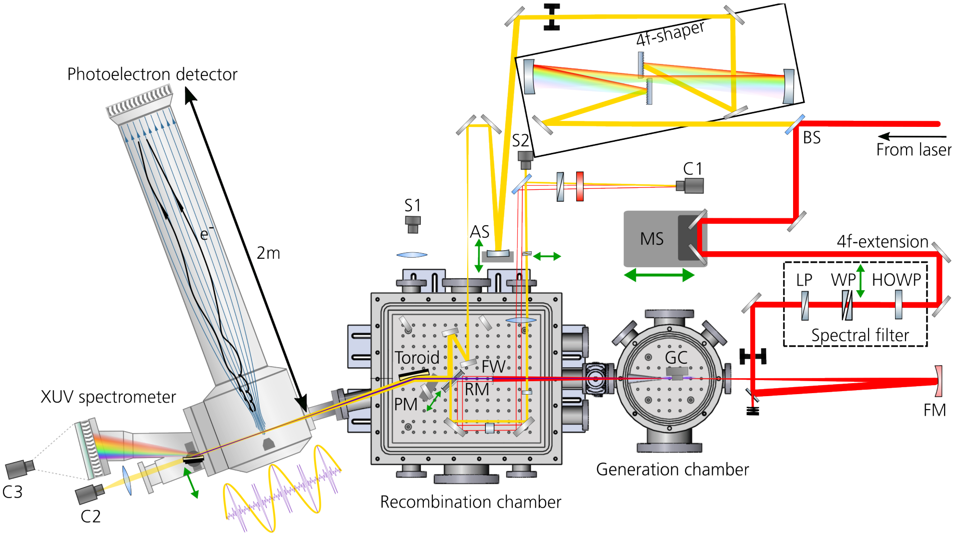

Figure 4.10: Sketch of the experimental setup used in KRAKEN measurements. A beam splitter (BS) transmits 60% to the probe (yellow) and reflects 40% to the pump (red) arms. The XUV is shown in purple. MS, femtosecond scale motorized delay stage; AS, attosecond scale piezoelectric stage; GC, gas cell; FW, filter wheel; RM, recombination mirror; PM, pick-up mirror; C1, C2, C3 cameras; S1, S2, IR spectrometers; HOWP, high-order waveplate; WP, wedge pair; LP, linear polarizer. Some elements of the active stabilization scheme are presented in more detail in Fig. 4.8. Figure adapted from paper **IV**.

4.4.3 Setup: KRAKEN

The setup used for the KRAKEN measurements in paper **IX** is to a large extent the same as that described in the previous sections. The notable difference is the requirement to be able to separately shape the spectrum of the pump and probe beams. In the probe beam, a bichromatic narrowband spectrum, tunable over a large bandwidth, is crucial to extract the full density matrix. In the pump beam, control of the central wavelength and bandwidth is important for the same reasons as in the RABBIT scheme, namely to tune the wavelength to hit, and resolve, narrow resonances.

The KRAKEN setup is shown in Fig. 4.10. Two pairs of mirrors on flip-mounts (not shown) allows us to change from the RABBIT to the KRAKEN scheme. In the KRAKEN scheme, the flip mirrors direct the probe and pump beams to two separate spectral shapers. In the probe arm, a $4f$-shaper is used, consisting of flat in- and out-coupling mirrors, two *Spectrogon* 1200 lines/mm reflective diffraction gratings and two 50 cm focal length spherical mirrors. After the first grating diffracts the beam, it is focused by the spherical mirror on

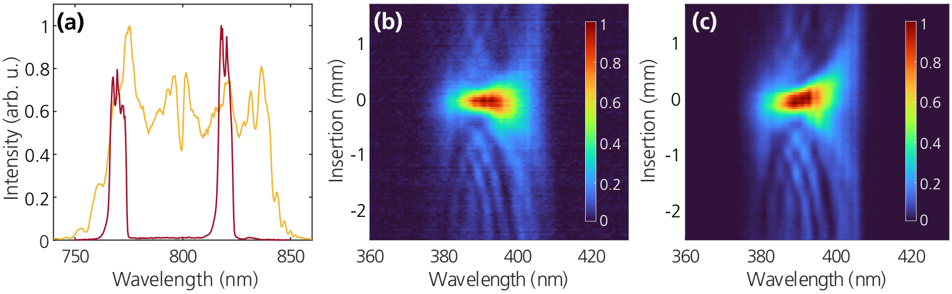

Figure 4.11: Characterization of the 4f-shaper (a) Spectrum of the probe beam before the 4f-shaper (yellow) and example spectrum after the 4f-shaper with two 3 mm slits placed in the Fourier plane (red). Measured d-scan trace, based on second harmonic generation, (b) before and (c) after the 4f-shaper. Figure adapted from paper **IV**.

a line where two 3 mm wide slits are mounted on linear translation stages. The two slits select the narrowband (approximately 8 nm FWHM) bichromatic probe components, as shown in Fig. 4.11(a). By tuning the position of the slits along the Fourier plane, different bichromatic probe spectra are obtained. After the Fourier plane, the diverging beam is collimated and compressed by the second spherical mirror and grating. Figure 4.11(b,c) show dispersion-scan (d-scan [215, 216]) measurements of the beam before and after the $4f$-shaper, respectively. The d-scan traces, recorded with no slits present in the Fourier plane, show that the pulses are to a large degree recompressed after the $4f$-shaper, apart from a small increase of third order dispersion indicated by the tilt above 400 nm.

In the pump arm, a $4f$-extension is included to match the path length increase due to the $4f$-shaper in the probe arm. In the $4f$-extension a spectral filter capable of tuning both the central wavelength and bandwidth is included. The filter, which is similar to a Lyot filter, consists of a high-order waveplate (HOWP) at a 45° angle to the incoming polarization, and a linear polarizer. The wavelength dependent phase retardation imparted to the beam by the waveplate, in combination with the linear polarizer, leads to a sinusoidal transmission spectrum. Tuning of the central wavelength and width of the sinusoidal peaks is achieved by varying the insertion of a pair of anti-reflection coated quartz wedges. The combined wedge pair and HOWP allows tuning of the waveplate order from approximately 5 to 15.

Chapter 5

Photoionization Studies

This chapter presents recent results of time-resolved photoionization experiments performed at the Lund Attosecond Laboratory. The results are based on papers **V**, **VI**, **VII** and **IX** and cover the topics of the previous chapter, *i.e.*, attosecond photoionization time delays, angle-integrated and angle-resolved resonant photoionization, and quantum state tomography of photoelectron wave packets.

5.1 Giant Dipole Resonance in Xenon

Photoionization from the 4d inner shell in xenon is studied in paper **V** in the 70 to 100 eV photon energy range. This energy range is characterized by several interesting phenomena. Dynamical electron correlations in the 4d shell lead to a collective oscillation, which presents itself as a spectrally broad enhancement in the photoabsorption cross section, called a *giant dipole* resonance [217–219], with a maximum around 100 eV. Photoionization of core electrons can also result in a process known as *Auger decay*, illustrated in Fig. 5.1(b). In Auger decay, the core hole left after ionization is filled by an outer electron, and the excess energy can be transferred to another electron which ionizes, forming Xe^{2+} ions[1]. Finally, relativistic effects can be quite strong in the threshold region (70 to 75 eV), with the two spin–orbit split $^2\mathrm{D}_{3/2}$ and $^2\mathrm{D}_{5/2}$ final ionic states displaying anomalous branching ratios due to jj–LS coupling changes [220].

The combination of spin–orbit split ionic states separated by 2 eV and Auger decay from the $5s$ and $5p$ shells leads to a complex, congested PES. To resolve it, and to be able to

---

[1] Fluorescence is also possible, and becomes the dominant relaxation process in heavy atoms.

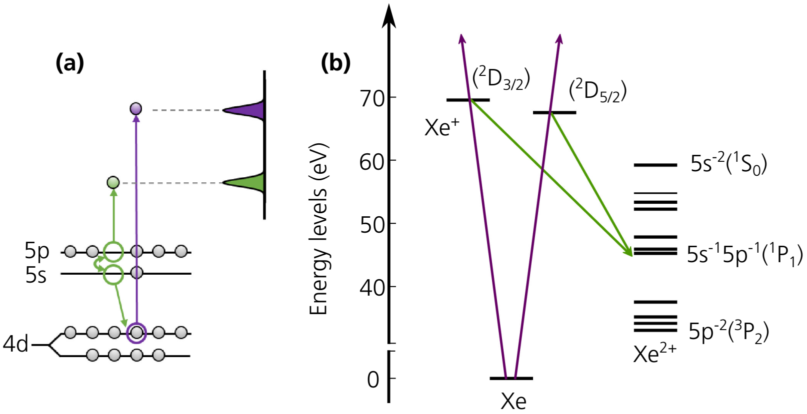

Figure 5.1: Xenon 4d ionization scheme. (a) XUV photoionization (purple) and Auger decay (green) of xenon 4d. (b) Energy diagram of Xe and intermediate Xe$^+$ and final Xe^{2+} states. Figure adapted from paper **V**.

correlate Auger electrons with the respective 4d ionization event, RABBIT measurements are performed using *coincidence spectroscopy* of photoelectrons detected with an MBES. In the coincidence technique, the XUV photon flux and target gas density are reduced to the point where less than one ionization event occurs per shot. In such conditions, double electron detection events can be assumed, to high accuracy, to originate from the same ionization event, and in the spectral range investigated, originate from Auger decay following single photoionization.

A two-electron coincidence map is shown in Fig. 5.2(a) for ionization in the presence of only the XUV field. In general photoelectrons from the 4d shell have higher energies than Auger electrons. These two classes of electrons are henceforth denoted fast electrons and slow electrons, respectively. Furthermore, the fixed energy differences between the outer and inner shells involved in the Auger decay means that the Auger electron kinetic energy is independent of the photon energy of the ionizing radiation. Projecting the spectrum on the fast electron energy axis within an energy interval (*e.g.* 10 to 10.4 eV) then allows us to isolate the photoelectron spectrum measured in coincidence with $4\mathrm{d}^{-1}(^2\mathrm{D}_{3/2}) \rightarrow 5\mathrm{s}^{-2}(^1\mathrm{S}_0)$ Auger decay, as shown in Fig. 5.2(c). Similarly, projection on the slow electron energy axis shows how Auger decay from different Xe$^+$ states can be disentangled. The case when both XUV and IR are overlapped in the target is shown in Fig. 5.2(b,e), where sidebands are visible between the harmonic peaks. Comparing the projections on the slow electron energy axis for the XUV only and the XUV+IR case reveals a small difference in spectral intensity from Auger electrons which absorb or emit an additional IR photon.

By fitting the sideband oscillations in different electron energy regions the time delays of

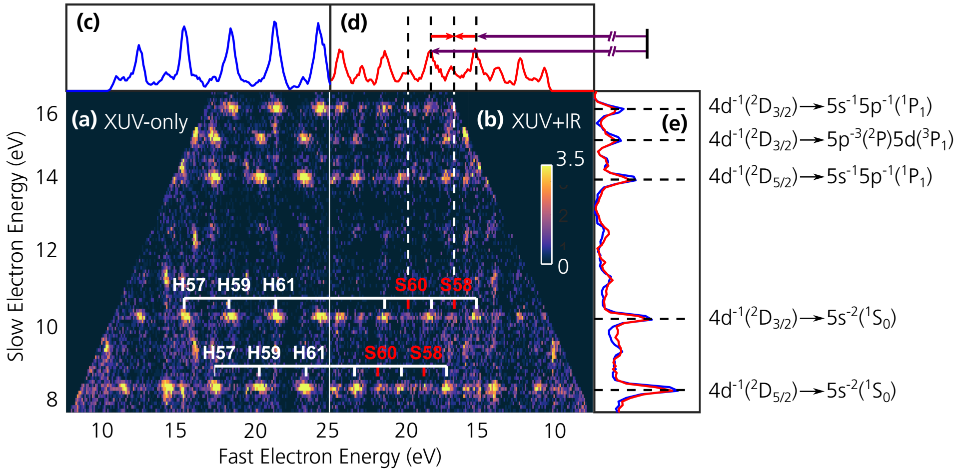

Figure 5.2: Two-electron coincidence spectra. Two-electron coincidence amplitude (colorscale) obtained from (a) XUV only and (b) XUV+IR. Projection of the fast electron energy axis (c) without and (d) with IR present. The projection is the sum over energies 10 to 10.4 eV corresponding to photoelectrons measured in coincidence with the $4d^{-1}(^2D_{3/2}) \rightarrow 5s^{-2}(^1S_0)$ Auger electron. (e) Projection of the slow electron energy axis with (red) and without (blue) IR field. Figure adapted from paper **V**.

different ionization channels can be determined, as discussed in Sec. 4.2.1. Different Auger decay channels are observed to have no effect on the oscillation phase, so that the signal can be averaged over these channels. To take into account the influence of the XUV group delay τ_{XUV} and isolate the interesting atomic delay τ_A, alternating measurements in xenon and neon are performed, and the time delay difference is calculated. By using neon 2p as a reference, absolute time delays in xenon can be inferred with reasonable accuracy. This is because neon 2p time delays are very small in the energy region of interest, and can be calculated with high accuracy [222].

The difference in time delays between xenon and neon, corresponding to absolute time delays of $\mathrm{Xe}(4\mathrm{d}_{3/2})$ and $\mathrm{Xe}(4\mathrm{d}_{5/2})$, are shown in Fig. 5.3(a,b) as a function of photon energy. Their difference $\tau_A[\mathrm{Xe}(4\mathrm{d}_{3/2})] - \tau_A[\mathrm{Xe}(4\mathrm{d}_{5/2})]$ is shown in Fig. 5.3(c). For high energies (80 to 100 eV) the time delay measured for the two final ionic states is similar, around 40 as, with a slight decrease for higher energies. For low energies (< 80 eV) there is a rapid change in time delay in opposite direction for the two channels. The difference between the two reaches almost 100 as at 75 eV. Theoretical calculations based on Relativistic Random Phase Approximation (RRPA) agree quantitatively for both ionic states at high energy, and qualitatively close to threshold. Below 75 eV, time delays could not be extracted from experimental data due to spectral overlap with double Auger decay. Furthermore, the branching ratios calculated within the RRPA model are shown in Fig. 5.3(d),

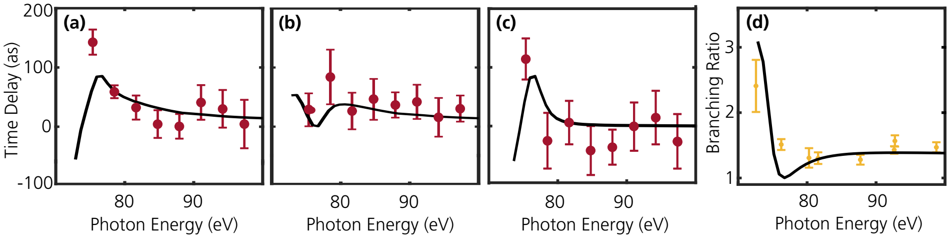

Figure 5.3: Channel resolved time delays. Absolute time delays (a) $\tau_A[\mathrm{Xe}(4\mathrm{d}_{3/2})] - \tau_A[\mathrm{Ne}(2\mathrm{p})]$ (b) $\tau_A[\mathrm{Xe}(4\mathrm{d}_{5/2})] - \tau_A[\mathrm{Ne}(2\mathrm{p})]$. (c) Difference between the two, $\tau_A[\mathrm{Xe}(4\mathrm{d}_{3/2})] - \tau_A[\mathrm{Xe}(4\mathrm{d}_{5/2})]$. Experimental data are in red. (d) Branching ratios of photoabsorption cross section (yellow) from Ref. [221]. Black lines indicate theoretical calculations using RRPA. Figure adapted from paper **V**.

showing excellent agreement with previous experiments [221].

By studying the RRPA transition matrix elements closer, we note that photoionization is dominated by the 4d→ ϵf transition, which includes contributions mainly from $4\mathrm{d}_{3/2} \to \epsilon\mathrm{f}_{5/2}$ and $4\mathrm{d}_{5/2} \to \epsilon\mathrm{f}_{7/2}$ at high energies. At low energies the $4\mathrm{d}_{5/2} \to \epsilon\mathrm{f}_{5/2}$ channel which implies a spin-flip also contributes, indicating the importance of the relativistic effects close to threshold. In the low energy region rapid oscillations in the energy-dependent time delays of the three channels are observed. These oscillations are due to quantum interference between the pure dipole transitions and the additional spin–orbit enabled non-dipole transition, explaining the anomalous branching ratio in Fig. 5.3(d).

5.2 Rydberg States in Helium

In paper **VI** we study two-photon resonant ionization of helium from the $1sn\mathrm{p}\,{}^1\mathrm{P}_1$ Rydberg series ($n = 3$ to 5) using the rainbow RABBIT technique [223, 224]. By tuning the wavelength of the driving field used for HHG, the 15th harmonic resonantly excites either the 1s3p, 1s4p, or a coherent superposition of 1s4p and 1s5p states. The excited states are then ionized by the overlapping IR probe field, referred to as “below-threshold RABBIT”. Figure 5.4 presents the excitation and ionization scheme, including the different angular momenta involved. The additional IR photon can bring the photoelectron into either an s or p angular momentum state with the same final energy, but with different angular probability distributions, which are indicated in the figure.

As mentioned before, in angular integrated measurements this leads to an incoherent sum of the different ionization channels. In some cases, like in xenon, a dominant channel can be identified, however this is not the case here. Furthermore, previous angle-resolved measurements have shown that the phase may not only change with the energy, but also

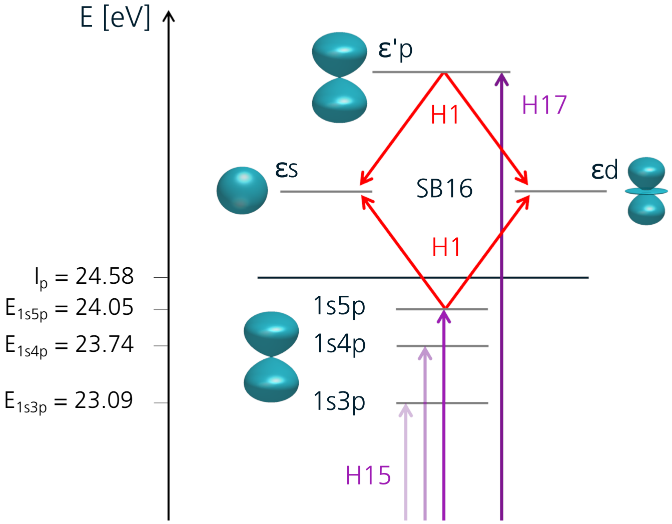

Figure 5.4: Resonant two-photon ionization of helium. Energy level diagram and RABBIT ionization scheme of the helium 1snp Rydberg series. Figure adapted from paper **VI**.

with the emission angle, and that ionization time delays can vary strongly with the angle of emission [225, 226]. This behavior is the result of interference of the different contributing angular channels. To disentangle the different channels we perform angle-resolved photoelectron measurements using a VMIS spectrometer.

The delay and angle dependent sideband oscillations are modeled using a partial wave expansion, taking into account finite-pulse effects and an ionization-induced broadening of the resonance. Two-photon matrix elements are calculated using the Random Phase Approximation with Exchange (RPAE) [227], which takes into account electron correlation effects. We extend the RABBIT scheme to below-threshold RABBIT for both the case of angle-integrated and angle-resolved measurements, and show that in the former, incoherent addition of the s and d channel leads to an ambiguous phase measurement off-resonance due to multiple channels contributing, but a well defined phase jump on-resonance. For the angle-resolved case we show that the measured phase of a sideband at a given angle can be determined unambiguously, and we derive conditions for angles where phase jumps should occur.

The results of the angle-resolved measurements around the 4p resonance are presented in Fig. 5.5(a). The right panel of the figure displays the phase of the photoelectron angular distribution, and the left panel shows the corresponding theoretical result. Within the limited region of high signal-to-noise ratio in the experimental data, delimited by the dashed black line, the similarity with theory is rather high. To understand the phase variations better,

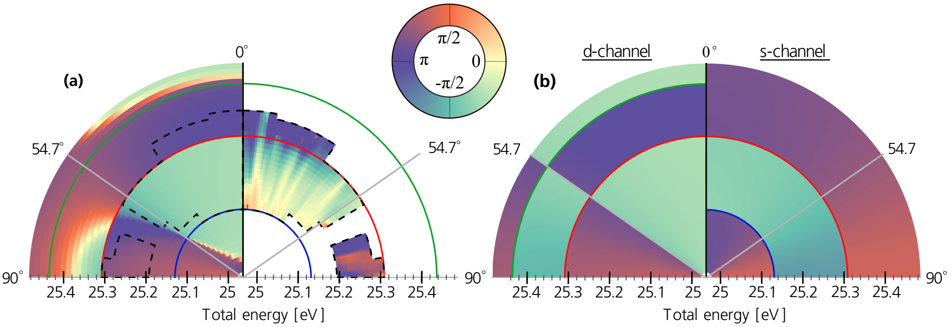

Figure 5.5: Angle-and-energy-resolved phase of the 4p resonance. (a) Angle- and energy-resolved phase of sideband 16 (colorscale) calculated using RPAE (left) and measured (right). The measured region with high signal-to-noise ratio is indicated on both sides by the dashed black line. (b) Channel resolve theoretical phase for the d contribution (left) and s contribution (right). Angles are defined with respect to the polarization axis of the (parallel) XUV and IR fields. Figure adapted from paper **VI**.

the calculated channel-resolved phases of the s and d partial waves are shown in Fig. 5.5(b).

Close to the 4p resonance, indicated by the red line, both channels present a sharp π rad phase jump, confirming the above statement that on-resonance, an angle-integrated measurement is sufficient to capture the phase variation. In the d-channel an additional sharp phase jump can be seen around 25.44 eV, indicated by the green line. In this region, the phase variation is not due to a resonance, but due to the amplitude of the matrix element going through a zero and changing sign, called an *anti-resonance*. In the left part of Fig. 5.5(a) showing the total phase, this anti-resonance can be seen as a strongly angle-dependent phase jump, taking place above 25.44 eV for angles smaller than $54.7°$, and below 25.44 eV for angles larger than $54.7°$. The phase jumps are a result of the change in relative strengths of the s and d channels in this region. Finally, in the energy range 25 to 25.3 eV a sharp phase jump is seen close to the *magic angle* (the angle at where $Y_{20} \propto P_2(\cos\theta) = 0$, which is $\theta \approx 54.7°$). At the place where the amplitude of the matrix element of the absorption path to the s-state is zero, indicated by the blue circle, this phase jump exactly corresponds to the magic angle. At slightly higher/lower energies, the phase jump depends on the relative strengths of the s- and d-channels.

These results indicate that angle-resolved measurements are of significant importance to completely characterize photoionization of even such simple systems as helium, signifying its indispensable use in more complex systems like molecules. Furthermore, angle-resolved measurements can provide a lot of information about not just the position of, and phase behavior at resonance, but also the relative strengths of different partial waves, and energy- and angle-resolved positions of sign changes in the matrix element amplitudes.

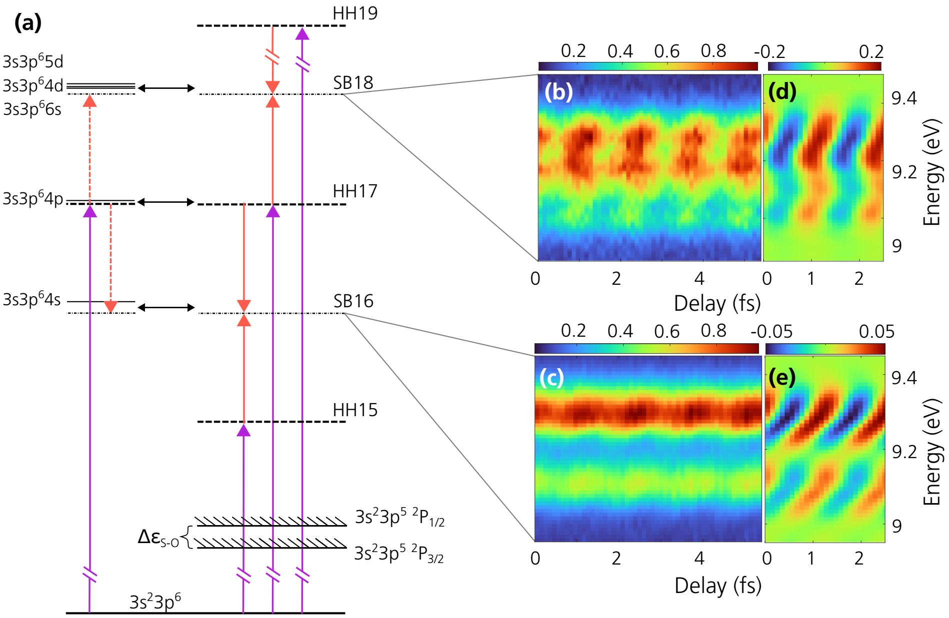

Figure 5.6: Argon Fano resonance. (a) Energy level diagram and excitation scheme of the $3s^{-1}4p$ Fano resonance. The resonant path and additional resonances near the final states are shown on the left. The direct ionization path is shown on the right. Black arrows indicate the Coulomb interaction. (b,c) Spin–orbit resolved RABBIT spectrogram around SB18 and SB16. (d,e) Oscillation amplitude of the $2\omega_0$ component around SB18 and SB16. Figure adapted from paper **VII**.

5.3 Fano Resonance in Argon

In paper **VII** we study the spectral amplitude and phase in vicinity of the $3s^{-1}4p$ Fano resonance in argon using the rainbow RABBIT technique. An energy levels diagram of the ionization scheme is shown in Fig. 5.6(a). With the upgraded setup described in Sec. 4.4 we improve on previous studies of this resonance [18, 228]. In particular, the improved experimental conditions allows us to completely resolve the two spin–orbit components ($\Delta\epsilon_{S\text{–}O} = 177$ meV) and resolve the Fano window resonance.

RABBIT spectrograms around the resonant SB18 and SB16 are shown in Fig. 5.6(b,c), where the S–O components are clearly visible. To isolate the interesting $2\omega_0$ signal, the amplitudes after Fourier filtering at $2\omega_0$ are shown in Fig. 5.6(d,e). A clear asymmetry in the oscillation across the resonance is visible when comparing the absorption and emission paths. The extracted spectral phase and amplitude of the $2\omega_0$ component across the resonance are shown in Fig. 5.7(a,b) for a probe bandwidth of 10 nm. In each sideband, the

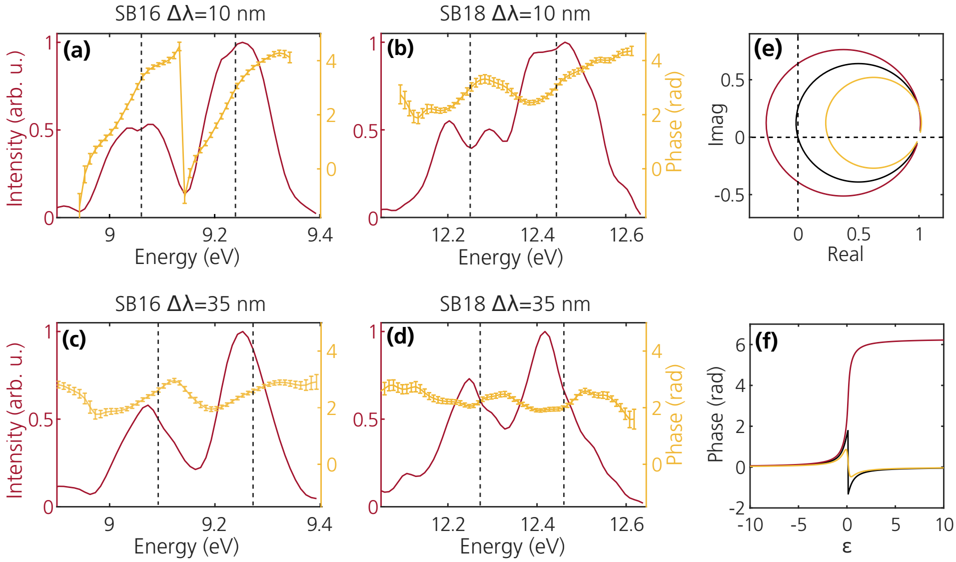

Figure 5.7: Influence of probe bandwidth. Measured spectral phase (yellow) and amplitude (red) across the $3s^{-1}4p$ Fano resonance in (a) SB16 and (b) SB18 using a probe bandwidth of 10 nm, and using a probe bandwidth of 35 nm in (c) SB16 and (d) SB18. (e) Complex plane representation of the resonance factor $R(\epsilon)$ for the cases $q = -0.25$ (black), $q = -0.25 - 0.25\mathrm{i}$ (red) and $q = -0.25 + 0.25\mathrm{i}$ (yellow) and (f) the corresponding phase as a function of the reduced energy ϵ. Figure adapted from paper **VII**.

phase variation across the two S–O components is similar, confirming the conclusion in previous work that the signal can be written as a sum of two identical distributions [228], shifted by $\Delta\epsilon_{\text{S–O}}$ and scaled according to the sum rule, $S_{\text{tot}}(\epsilon) = S(\epsilon) + 2S(\epsilon - \Delta\epsilon_{\text{S–O}})$.

The phase in SB16 shows a variation of almost 2π rad across each S–O component, while the phase variation in SB18 is approximately 1.4 rad. We also perform measurements using a broad 35 nm probe bandwidth. The spectral phase and amplitude in that case are shown in Fig. 5.7(c,d) for SB16 and SB18. The phase jump in SB16 is considerably smaller than for the narrowband probe, and the phase reproduces that observed in previous works [18, 228].

This large asymmetry, and the appearance of a phase jump larger than the π-variation predicted by Eq. (4.10), are possible if the q-parameter is allowed to take complex values. In the context of RABBIT measurements, this happens because the probing IR field couples the discrete quasi-bound state with the final sideband continuum states [229, 230] through absorption/emission of an additional IR photon, indicated by the dashed red arrows in Fig. 5.6(a), and Coulomb interaction, indicated by the black arrows. This coupling leads to a broadening of the resonant state, which we include phenomenologically by modifying the reduced energy

$$\epsilon = \frac{2(E - E_\alpha)}{\Gamma} \rightarrow \frac{2(E - E_\alpha \pm \mathrm{i}\gamma)}{\Gamma}, \tag{5.1}$$

where ± refers to either absorption or stimulated emission followed by Coulomb interaction. Assuming $\gamma \ll \Gamma$, this leads to a complex q given by

$$q \rightarrow q_{\mathrm{eff}}^{\pm} \approx q \mp 2\,(1 - \mathrm{i})\,\frac{\gamma}{\Gamma}. \tag{5.2}$$

This expression is similar to that of Refs. [18, 188, 228], where the broadening γ is replaced by a variable describing the relative coupling strength between the IR-induced path from the discrete state to the final continuum state, and the path representing decay to the intermediate continuum followed by absorption/emission of an IR photon.

Our experimental observations can be explained by a complex Fano parameter in combination with finite-pulse effects in the two-photon transition matrix element in Eq. (4.2). This is qualitatively illustrated in Fig. 5.7(e), which shows the complex plane representation of $R(\epsilon)$ when including the complex $q_{\mathrm{eff}}^{\pm}$, and in Fig. 5.7(f) showing the corresponding spectral phase $\arg[R(\epsilon)]$. First, for the case of no imaginary part ($\gamma \rightarrow 0$), the complex trajectory of the resonance factor intersects the origin, leading to a sharp $-\pi$ phase jump. With the addition of a small negative or positive imaginary part, which corresponds to the emission and absorption path, the amplitude of the complex trajectory is increased or decreased. In the emission path, the origin is enclosed by the complex trajectory, leading to a 2π phase jump, while in the absorption path the trajectory no longer intersects the origin, resulting in a smaller, smoothed out phase jump.

Secondly, the convolution over bandwidths in Eq. (4.2) due to finite-pulse effects leads to a smaller matrix element amplitude for short pulses, contracting the circular trajectory, and conversely a larger amplitude for long pulses, expanding the trajectory. This explains the abrupt disappearance of the 2π phase jump when increasing the probe bandwidth.

Finally, the strength of the radiative coupling from the discrete state is strongly dependent on resonances in the final state of the two-photon transition. In argon, strong coupling to a broad $3\mathrm{s}^{-1}4\mathrm{s}$ resonance in the emission path and a range of resonances in the absorption path allows us to observe this asymmetry. In other atoms or final state energies, where the radiative coupling may be weaker, even small finite-pulse effects are enough to shift $R(\epsilon)$ to the positive half-plane, so that no 2π phase jump is visible [198].

In conclusion, this points to a potentially large observer effect in RABBIT measurements, where the act of probing the system alters the result. However, using narrowband probes the RABBIT technique may in that case also be used as a very sensitive tool to probe optically dipole-forbidden resonances like the $3\mathrm{s}^{-1}4\mathrm{s}$ resonance.

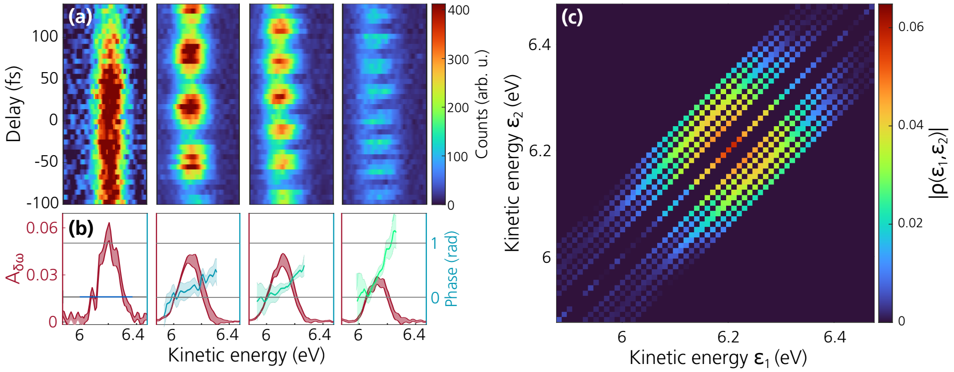

Figure 5.8: Experimental KRAKEN in helium. (a) Photoelectron spectrograms for $\delta\omega = 0, 61, 98, 134$ meV. (b) Energy-resolved $\delta\omega$-amplitude (red) and -phase (cyan) of the spectrograms, obtained by a cosine-fit. (c) Sparse density matrix constructed from seven photoelectron spectrograms with $\delta\omega = 0$ to 134 meV. Figure adapted from paper **IX**.

5.4 Measuring the Quantum State of Photoelectrons

In paper **IX** we experimentally reconstruct photoelectron quantum states in helium and argon using the KRAKEN technique. We generate harmonics in argon and photoionize helium and argon atoms with the 19th harmonic into a flat continuum. The EWP is probed by absorption of a bichromatic IR field with one wavelength fixed at 770 nm and the other varying from 770 to 840 nm in steps of 10 nm. To isolate the absorption path of HH19 from the emission path of HH21, a combined germanium-aluminum filter is used, with a sharp transmission drop above HH19.

Figure 5.8(a) shows measured spectrograms for different values of the bichromatic probe splitting $\delta\omega$ in helium, where the beating is clearly visible and increases in frequency for larger $\delta\omega$. The spectrograms match well with those calculated from theory in Fig. 4.5(b). For each spectrogram, oscillations at $\delta\omega$ are extracted for each energy bin from a cosine-fit with a Gaussian envelope along the XUV–IR delay. The extracted amplitudes and phases are shown in Fig. 5.8(b). The amplitude can be seen to decrease for larger $\delta\omega$, indicating a lower degree of coherence. Note that to draw this conclusion, the amplitudes are normalized as

$$\rho_{\text{norm}}(\epsilon, \epsilon + \delta\omega) = \frac{\rho_{\text{raw}}(\epsilon, \epsilon + \delta\omega)}{I_{\text{XUV}}\sqrt{S_{\omega_1} I_{\omega_1} S_{\omega_2} I_{\omega_2}}}, \tag{5.3}$$

where I_{XUV} and I_{ω_i} are the spectral intensities of the XUV and IR fields, and S_{ω_i} is the spectrometer[2] response function at the wavelength of the IR probe components. In the phases shown in Fig. 5.8(b), a linear phase variation which increases with $\delta\omega$ can be seen,

---

[2] Measured by S2 in Fig. 4.10.

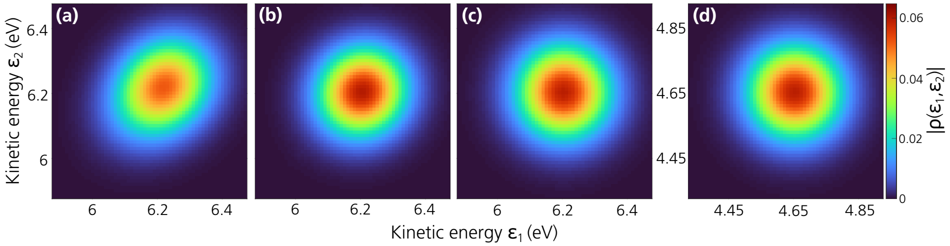

Figure 5.9: Helium photoelectron quantum state. Density matrix from (a) experiment, reconstructed using KRAKEN, (b) experiment, reconstructed using KRAKEN, compensating for the spectrometer PSF, (c) theory, retrieved using KRAKEN and (d) direct theoretical calculation of one-photon ionization. Figure adapted from paper **IX**.

which is due to the harmonic femtochirp discussed in Sec. 2.2.3.

The $\delta\omega$-amplitudes are then placed as subdiagonals in a sparse density matrix, shown in Fig. 5.8(c). Here, the acquired data is mirrored in the anti-diagonal, since the density matrix is Hermitian. The sparse density matrix is close to circular, which indicates that the measured state is highly coherent. To obtain the full continuous density matrix from sparsely acquired data we use a Bayesian estimate based on a Hamiltonian Monte-Carlo method. The reconstructed continuous density matrix is shown in Fig. 5.9(a), where a slightly elliptic shape is evident. The ellipticity can be attributed to the long, low-energy tail in the point-spread-function of the MBES, which induces experimental decoherence [26], lowering the purity. To eliminate the influence of the MBES, we measure the PSF and correct for it in the Bayesian optimization algorithm. The result is a more circular density matrix, displayed in Fig. 5.9(b).

We compare the experimental results to a theoretical KRAKEN scheme based on two-photon calculations obtained using relativistic RPAE in Fig. 5.9(c) [231], and to direct calculations of the one-photon (XUV only) density matrix, shown in Fig. 5.9(d). The comparison shows excellent qualitative and quantitative agreement with the experimental density matrix corrected for the MBES response function.

The above described measurements, data analysis and calculations are also performed in argon in identical conditions to test whether the spin–orbit splitting leads to a faster decay of the coherences, as discussed in Sec. 4.3. The argon density matrix displays a strong ellipticity, similar to that in Fig. 4.6(g)[3].

Finally, we calculate the purity in both helium and argon using Eq. (4.13) and compare it to the purity obtained from single-photon relativistic RPAE. In helium we obtain an experimental purity of $\gamma = 0.94 \pm 0.06$, while the theory gives a fully pure state $\gamma = 1.00$.

---

[3] Excluding the effect of the Fano resonance.

In argon the experimental purity is $\gamma = 0.64 \pm 0.02$, and theory gives $\gamma = 0.61$. The good agreement for helium indicates that the degree of experimental decoherence is very low, which validates the experimental KRAKEN technique, and allows us to conclude that the lower purity obtained in argon is due to decoherence induced by the spin–orbit splitting.

Chapter 6

Summary and Outlook

This thesis treats generation of extreme ultraviolet attosecond pulses and their application to photoelectron interferometry. Scaling invariant rules for efficiency optimization of high-order harmonic generation in gases are investigated, with an emphasis on phase-matching. The attosecond pulse trains obtained from high-order harmonic generation are used to study photoionization dynamics on the femto- and attosecond timescales using a variety of pump-probe photoelectron interferometry techniques, including angle-resolved and angle-integrated high-resolution "rainbow" RABBIT, coincidence spectroscopy in combination with RABBIT, and a new quantum state tomography protocol, KRAKEN.

Optimization of High-order Harmonic Generation

In paper **I** optimization of the conversion efficiency in high-order harmonic generation in gases is explored numerically. Two phase-matching regimes yielding similar conversion efficiency, but different temporal and spatial characteristics of the generated radiation, are identified: a high pressure, short medium regime, and a low pressure, long medium regime. The two regimes correspond to asymptotes of a medium pressure–length hyperbola, which is successfully predicted by a 1D analytic model. In paper **II** the model and simulations are tested experimentally using two beamlines in different focusing conditions. The hyperbolic relationship is verified for different harmonic orders, focusing conditions and peak intensities, and the difference in spatial quality of the generated radiation is confirmed. In paper **III** the beam divergence of high-order harmonics generated from long, low pressure gas cells and short, high pressure gas jets is investigated experimentally and numerically. In the high pressure regime, harmonics are emitted with a larger divergence. These studies, in combination with previously formulated scaling laws [33], and recent detailed models of the effect of linear density gradients on the conversion efficiency [171], can provide valuable design guidance for future HHG sources.

So far, a systematic study of the pulse duration effect on conversion efficiency has not been done. The continuous development of new laser sources, and improvements in control of output pulse duration by post-compression techniques [232], motivates further work in this direction. The underlying physics of the two phase-matching regimes suggest, however, that a multi-parameter scan of, *e.g.*, the medium length and density, and pulse peak intensity should be performed in conjunction with a pulse duration scan. Several other potentially important parameters for finding a global conversion efficiency optimum exists, such as the position of the medium relative to the laser focus. Studying the effect of the medium position on the conversion efficiency and refocusability of the generated harmonics may be particularly interesting for experiments demanding high XUV intensity on target [179, 181].

Improving the Experimental Setup

An important part of the work has been to build a new, versatile, ultra-stable setup for attosecond pump-probe photoelectron interferometry, which is described in paper **IV**. By actively and directly stabilizing to the phase relation of the pump and probe femtosecond laser pulses, independent spectral shaping of the pump and probe pulses and seamless switching between RABBIT and KRAKEN experiments, while maintaining a temporal stability as small as 13 as RMS over several hours, is possible.

The final initially planned upgrade to the setup is the implementation of a faster data acquisition card, which can further improve the spectral resolution. Additionally, the issue of isolating density matrices from the absorption and emission paths in the new KRAKEN technique demands a more versatile solution than using combinations of metallic filters. Potential candidates include generating harmonics with a frequency doubled pump, or spectrally broadening the IR spectrum to probe with frequencies far from the pump central frequency. Lastly, to reduce the time it takes to run a KRAKEN scan (currently each subdiagonal of the density matrix takes roughly one hour), a set of more than two probe wavelengths can be used, if chosen cleverly. By using frequencies with a frequency spacing modeled after a *Golomb ruler*, a set of unique beating frequencies can be obtained simultaneously.

High Resolution RABBIT Experiments

In papers **V**, **VI** and **VII** we study electron correlation effects in photoionization using the RABBIT technique. In paper **V**, broadband RABBIT measurements are used together with coincidence spectroscopy to study photoionization time delays from the 4d shell in xenon. With the help of theory, we disentangle the contributions of a short-lived giant dipole resonance and a slowly decaying spin–orbit enabled narrow resonance. In paper **VI**, we use the energy-resolved "rainbow" RABBIT technique to study resonant two-photon ionization of Rydberg states in helium. Combining angle-resolving and high-resolution angle-integrating photoelectron spectrometers with theoretical calculations we explain the phase jumps occurring as a function of energy and angle. In paper **VII** we measure the spectral phase and amplitude across the $3s^1 3p^6 4p$ Fano resonance in argon. By using the rainbow RABBIT technique we resolve the close-lying spin–orbit components. When using a narrow 10 nm probe bandwidth, a strong asymmetry is observed between the absorption and emission paths in the spectral phase, with a close to 2π phase jump in the emission path. The results are explained by finite pulse effects and strong radiative couplings of the intermediate quasi-bound state and final continuum, due to final state resonances.

These measurements demonstrate the importance of a high spectral resolution to resolve complex ionization dynamics, the results of which can ultimately be used to test theoretical models of electron correlations. With our improved repetition rate, spectral resolution and long-term stability, studying more complex atoms and small molecules is now possible. In combination with a long delay scan range, observations of spectral phase variations as a function of pump–probe delay may reveal interesting dynamics in resonance build-up [224, 233, 234], or beatings of different spectrally overlapping decay channels [235].

Quantum Light and Attosecond Science

In paper **VIII** and **IX** we extend photoelectron interferometry to complete characterization of mixed states by reconstructing the density matrices of photoelectrons using KRAKEN. In paper **VIII** the KRAKEN protocol is developed theoretically. Density matrices in helium and argon are reconstructed by applying the KRAKEN protocol to simulated data, and are validated by comparing to direct calculations of the density matrices. Using the KRAKEN protocol we also show it is possible to measure the degree of ion-photoelectron entanglement due to spin–orbit split ionic states. In paper **IX** the KRAKEN protocol is verified experimentally by reconstructing the density matrices of electrons ionized from helium and argon. A reduced purity, in agreement with theory, is measured in argon due to the entanglement of ion and photoelectron, combined with an incomplete measurement.

Recently, increasing effort is being devoted towards bridging the gap between quantum-optics and -information with strong-field attosecond science [25, 236]. Development of new quantum state tomography techniques for continuum electrons [203, 237], like the KRAKEN protocol discussed here, is driven by the need to fully characterize mixed states. Intense laser-atom interactions have also been shown to generate non-classical light states [238], and the theory of high-order harmonic generation has been extended to the case of a quantized light field [239], with generation of harmonics by quantum states of light leading to a theoretical enhancement of the cut-off energy [240]. Much like RABBIT was initially used to retrieve the phase relation of harmonics generated from classical light, the KRAKEN protocol may provide an experimental tool to characterize high-order harmonic generation driven by quantum light states.

Appendix A

PPT Ionization Rate

The functions entering the PPT ionizaiton rate introduced in Sec 3.3.1 are summarized below [141]. The ionization rate $\Gamma^{\mathrm{PPT}}_{\ell m}(\mathcal{E},\omega_0)$ from a level with binding energy I_p, orbital ℓ and magnetic m quantum number, with the quantization axis chosen parallel to the field polarization, is given (atomic units are used: $\hbar = m_e = e = 1$) by

$$\begin{aligned}\Gamma^{\mathrm{PPT}}_{\ell m}(\mathcal{E}_0,\omega_0) =& \sqrt{\frac{3}{2\pi}}|C_{n^*\ell^*}|^2 f_{\ell m} I_p \left[\frac{2(2I_p)^{3/2}}{\mathcal{E}_0\sqrt{\gamma^2+1}}\right]^{2n^*-|m|-3/2} \\ &\times A_m(\gamma,\omega_0)\exp\left[-2(2I_p)^{3/2}\frac{g(\gamma)}{3\mathcal{E}_0}\right]\end{aligned} \tag{6.1}$$

where $\mathcal{E}_0$ is the peak electric field, $n^* = Z/\sqrt{2I_p}$ and $\ell^* = n^* - 1$ is the effective principal and orbital quantum numbers and

$$C_{n\ell} = \frac{2^{2n}}{n\Gamma(n+\ell+1)(n-\ell)}, \tag{6.2a}$$

$$f_{\ell m} = \frac{(2\ell+1)(\ell+|m|)!}{2^m|m|!(\ell-|m|)!}, \tag{6.2b}$$

where $\Gamma(z)$ is the gamma function extending the factorial function to the complex numbers. The function $g(gamma)$ is given by

$$g(\gamma) = \frac{3}{2\gamma}\left[\left(1+\frac{1}{2\gamma^2}\right)\sinh^{-1}\gamma - \frac{(1+\gamma^2)^{1/2}}{2\gamma}\right], \tag{6.3}$$

which is $1-\gamma^2/10+9\gamma^4/280$ when $\gamma \ll 1$ and $3/(2\gamma)(\ln 2\gamma - 1/2)$ when $\gamma \gg 1$.

The sum over different order multi-photon ionization rates in the PPT model, which also leads to the characteristic channel closings in Fig. 3.6, is included in A_m,

$$A_m(\gamma,\omega_0) = \frac{4\gamma^2}{\sqrt{3\pi}|m|!(1+\gamma^2)} \times \sum_{n\geqslant\nu}^{\infty} \mathrm{e}^{-\alpha(n-\nu)w_m\left(\sqrt{\beta(n-\nu)}\right)}, \tag{6.4}$$

which in turn depends on $\beta = 2\gamma(1+\gamma^2)-1/2$ and

$$\alpha = 2\left[\sinh^{-1}\gamma - \frac{\gamma}{(1+\gamma^2)^{1/2}}\right], \tag{6.5}$$

which can be approximated as $2\gamma^3/3$ for $\gamma \ll 1$ and $2(\ln 2\gamma - 1)$ for $\gamma \gg 1$. Finally, the function

$$w_m(x) = \mathrm{e}^{-x^2}\int_0^x \mathrm{d}y\, \mathrm{e}^{y^2}(x^2-y^2)^{|m|} = \frac{x^{2|m|+1}}{2}\int_0^1 \mathrm{d}t\, \frac{\mathrm{e}^{-x^2 t}t|m|}{(1-t)^{1/2}}. \tag{6.6}$$

For $m=0$ the above function reduces to the Dawson function $D_+(x)$, while for $m=\pm1$ it becomes $w_{\pm1}(x) = (2x^2+1)D_+(x)/2 - x/2$. In general the exponential dependence in A_m leads to an ionization rate which is strongly dominated by ionization from $m=0$.

Author Contributions

Paper I: How to optimize high-order harmonic generation in gases

We study optimal generation of high-order harmonics by simulation of wave propagation in gases. We identify two different regimes of phase matching, a high pressure, short medium regime, and a low pressure, long medium regime. The conversion efficiency is found to be similar in the two regimes, but the spatial and temporal properties of the harmonic emission vary. A simple analytic model is developed which accurately predicts the regions of efficient generation.

I performed the simulations, analyzed the results and wrote the manuscript.

Paper II: The two phase-matching regimes in high-order harmonic generation

In this paper, we study experimentally the two different regimes of high-harmonic generation proposed in paper **I**. The similar conversion efficiency along a hyperbolic curve in pressure-length is confirmed. The predicted spatial characteristics are also shown to agree with numerical simulations. Measurements in two beamlines, in different conditions, confirm the independence of the results on focusing geometry, pulse duration and intensity.

I participated in taking the measurements and in the interpretation and discussion of the results. I also provided comments and feedback on the manuscript.

Paper III: Ultrastable, high-repetition-rate attosecond beamline for time-resolved XUV-IR coincidence spectroscopy

In this paper, an ultra-stable high-repetition rate attosecond beamline for pump-probe photoelectron-photoion coincidence spectroscopy is implemented and characterized. Long-term stability with an estimated time delay error of 12 as is achieved by combining industrial-grade lasers with a collinear pump-probe delay line. In particular, a characterization of different gas targets for HHG is performed. The harmonic dependent divergence is investigated experimentally, and compared to simulations, for gas jets and gas cells of different lengths.

I performed the simulations of the HHG divergence. I also provided comments and feedback on the manuscript.

Paper IV: Ultra-stable and versatile high-energy resolution setup for attosecond photoelectron spectroscopy

In this paper, we describe an ultra-stable interferometer for attosecond pump-probe photoelectron spectroscopy. By stabilizing the interferometer directly to the phase relation of the femtosecond pump and probe laser pulses, we obtain advantages in flexibility, allowing several types of interferometric measurement schemes to be performed easily. We show that by reducing the probe bandwidth, the resolution in spectral phase measurement of photoelectrons is enhanced.

I was responsible for building and designing the setup. I also participated in the measurements, and in the writing of the manuscript.

Paper V: Attosecond electron–spin dynamics in Xe 4d photoionization

Photoionization from the 4d shell in xenon is studied by combining attosecond interferometry and coincidence spectroscopy. With the help of calculations using relativistic random phase approximation we identify two interfering ionization mechanisms with different time delays: a fast decaying giant dipole resonance and a slow decaying narrow resonance induced by spin-flip transitions.

I participated in the experimental measurements, and in the discussions and interpretation of the results and provided comments and feedback on the manuscript.

Paper VI: Resonant two-photon ionization of helium atoms studied by attosecond interferometry

We study resonant two-photon ionization via the 3p, 4p, 5p Rydberg states in helium using both angle-resolved and angle-integrated RABBIT measurements. Combining the two experiments with theoretical calculations, we explain the phase variations observed as a function of photoelectron emission angle and energy.

I participated in taking the measurements and in the discussions of the results. I also provided comments and feedback on the manuscript.

Paper VII: The influence of final state interactions in photoelectron interferometric measurements of Fano resonances

In this paper, we performed angle-integrated RABBIT measurements across the spin-orbit resolved $3s^{-1}4p$ Fano resonance in argon with high spectral resolution. We find that the phase depends on whether it is measured above or below the resonance, due to the influence of additional states in the $3s^{-1}$ channel. This asymmetry depends strongly on the probe bandwidth and wavelength. We show that a complex Fano parameter q is required to fully explain the phase behavior.

I participated in the measurements and analysis. I also provided comments and feedback on the manuscript.

Paper VIII: Continuous-variable quantum state tomography of photoelectrons

We propose a protocol (KRAKEN) for continuous variable quantum state tomography of photoelectrons. The protocol uses two synchronized narrowband infrared probe fields at different frequencies to interfere different parts of a photoelectron wavepacket, which is ionized by an XUV harmonic. By varying the XUV-IR delay and probe field frequency difference, the phase and amplitude of the density matrix can be reconstructed. We test the KRAKEN protocol numerically for the case of pure and mixed photoelectron states, in the vicinity of autoionizing resonances in helium and argon.

I participated in the discussions during the development of the protocol, and provided comments and feedback to the manuscript.

Paper IX: Measuring the quantum state of photoelectrons

In this paper, we demonstrate the KRAKEN protocol experimentally. We measure the density matrix of photoelectrons ionized into flat continua in argon and helium and compare the results to theoretical calculations. The density matrix describing the photoelectron in helium is that of a pure state, while in argon the state is mixed due to spin-orbit splitting and ion-electron entanglement.

I participated in taking the measurements and in the interpretation and discussion of the results. I also provided comments and feedback on the manuscript.

Acknowledgments

The work presented in this thesis would never have been possible without the help of many colleagues at the Division of Atomic Physics and collaborators from across the world. First, I would like to thank my main supervisor, Anne L'Huillier. Thank you for all your guidance, for always encouraging me to do more, and for showing such enthusiasm whenever we have discussed the latest results. I have really enjoyed working with you on the "recipe". I would also like to thank my supervisors Cord Arnold and Mathieu Gisselbrecht. You have impressed me with your expertise, and for always being approachable. Together with Anne, you have been able to create such a great and lasting atmosphere in the group.

Special thanks to the people working in the attolab, David Busto, Hugo Laurell, Lana Neoričić, Mattias Ammitzböll, Sizuo Luo, Shiyang Zhong, and the students we have had in the group, Vénus Poulain, Albin Hedse, Ron Demjaha and Hugo Söderberg. The many long days in the lab would have been much longer, and much less enjoyable without you. Thank you David for always taking the time to discuss any questions I have had, and for showing me the wonders that some duct tape and plastic foam can accomplish. Thank you Hugo for offering a different, more theoretical view, of any problem we have had. Doing a PhD in parallel with you, and sharing both the ups and downs, has been great! Thank you Lana for being such a genuine person, and always speaking your mind. Thank you Mattias for your ever-present positive attitude and for the many diverse discussions we had while aligning the beamline (and thank you for not dancing too close to it afterwards). Thank you Sizuo for your encouraging words "Never give up!", and for teaching me much about China.

I would like to thank all collaborators who have contributed to this work. Thank you Stefanos Carlström for providing us with TDSE data. Thank you Laura Rego for performing the SFA calculations. Thank you Peter Smorenburg, Christoph Heyl and Eric Constant for your valuable input and interesting discussions about HHG. I want to thank Balázs Nagyillés, Zsolt Divéki, Balázs Farkas, Katalin Varjú and Subhendu Kahaly for the beamtime at ELI-ALPS and for welcoming us to Szeged. Thank you Dominik Ertel, Gi-

useppe Sansone and the rest of the group at Freiburg University for the discussions about generating stable harmonics in gas cells and jets. Thank you Raimund Feifel and Richard Squibb for all the help with the MBES. Again, thank you Richard, for offering to read through my thesis, and for all your terribly good puns. Thank you Per Eng-Johnson, and thanks to the old 10 Hz crew Jan Lahl, Hampus Wikmark, Sylvain Maclot for the (intense) VMI campaign. Thank you Marcus Isinger and David Kroon for your contributions to the new attolab setup.

During this thesis, much like during the past decades of attosecond science, not only good lasers, but also good theory, has been very important. I would to thank the theorists with whom we have had many fruitful collaborations. Thank you Eva Lindroth, Leon Petersson, Jimmy Vinbladh, Anton Ljungdahl, Göran Wendin, Marcus Dahlström, Fernando Martín, Roger Bello Romero, Luca Argenti, Carlos Marante, Tönu Pullerits, Daniel Finkelstein-Shapiro, Andreas Buchleitner, Christoph Dittel, Shahnawaz Ahmed and Anton Kockum.

Thank you Esa Paju for teaching me many valuable things about vacuum technology and leak testing, and for the help with repairing our vacuum chamber. Thank you Noelle Walsh for lending us the acquisition card. Thank you Håkan Ivansson for all the help with my designs for our setup. Thanks to the Enterprise guys, Samuel Bengtsson, Emma Simpson and Anna Olofsson, headed by Johan Mauritsson, for being great beamline neighbours, and for all you taught me about the laser and the rest of the lab.

Thank you Jasper Peschel for the sailing adventure, and for always being able to make me see things from a different point of view. Thank you Federico Vismarra for your enthusiasm for science and for your perfectly reasonable plans of becoming a world leader, please send my regards to E.W. Chen Guo, 54 68 61 6E 6B 73 for helping me raise M.A. Thank you Serhii Derenko for the trips down the Wikipedia rabbit holes. Thank you Ann-Kathrin Raab for introducing me to Chairs Underwater and for keeping the tradition of the Atto apartment alive. Thank you Elisa Appi for all the wine we had at the wine festival week, and for the work we did on the hyperbola. Thank you Marius Plach for all the travels we did, and for making the best watermelons. Thank you Neven Ibrakovic and Fabian Langer for the lunch game and the many odd conversations during lunch and coffee breaks. Thank you Alexander Permogorov and Ivan Sytcevich for being fellow vodka belters and for blessing us with all the greatest hits of the Bl..ini Boys. Thank you Cornelia Gustafsson for making the teaching of the Zeeman lab more fun. There are many more people who have contributed to the great social and working environment during my PhD: thank you Praveen Kumar Maroju, Anne-Lise Viotti, Maria Hoflund, Sara Mikaelsson, Jan Vogelsang, Daniel Díaz Rivas, Nedjma Ouahioune, Melvin Redon, Nils Weber, Yuman Fang, Dominik Hoff, Marvin Schmoll and everyone else at the Division of Atomic Physics. Finally, I would like to express my gratitude towards Jörgen Larsson, Claes-Göran Wahlström, Anne-Petersson-Ljungbeck, Emelie Niléhn, Åke Johansson, Maria Algotsson and Jakob Testad for their help with administrative and technical issues.

During especially the last year of my PhD I have been fortunate enough to travel a lot, and meet and discuss with many peers. Thank you especially Lisa-Marie Koll and Barbara Merzuk for the great times in Paris and Korea. I would also like to thank my friends. Tack Jenni och Oskar för att ni tvingat ut mig ur källaren. Tack Hampus för de många intressen vi delat, däribland fotonik. Tack Alle och Calle för allt stöd och visat intresse för fysikatomer och lasersvärd. Tack Johanna, William, Indy, Erik och Andreas för alla trevliga stunder ute på schlätta'. Jag vill även tacka min familj för all uppmuntran under de här åren. Slutligen vill jag tacka dig Saga, utan ditt oavbrutna stöd det senaste året hade jag sannolikt förgåtts.

Bibliography

[1] A. Einstein. Über einen die erzeugung und verwandlung des lichtes betreffenden heuristischen gesichtspunkt. *Annalen der Physik*, 322(6):132–148, 1905.

[2] K. Siegbahn and K. Edvarson. β-ray spectroscopy in the precision range of $1 : 105$. *Nuclear Physics*, 1(8):137–159, 1956.

[3] G. A. Mourou, T. Tajima, and S. V. Bulanov. Optics in the relativistic regime. *Reviews of Modern Physics*, 78:309–371, 2006.

[4] E. Matthias, R. Rosenberg, E. Poliakoff, M. White, S.-T. Lee, and D. Shirley. Time resolved vuv spectroscopy using synchrotron radiation: fluorescent lifetimes of atomic kr and xe. *Chemical Physics Letters*, 52(2):239–244, 1977.

[5] L. Mandelstam and I. Tamm. *The Uncertainty Relation Between Energy and Time in Non-relativistic Quantum Mechanics*. Springer Berlin Heidelberg, Berlin, Heidelberg, 1991.

[6] T. H. Maiman. Stimulated optical radiation in Ruby. *Nature*, **187**:493, 1960.

[7] F. J. McClung and R. W. Hellwarth. Giant optical pulsations from ruby. *Applied Optics*, 1(S1):103–105, 1962.

[8] L. E. Hargrove, R. L. Fork, and M. A. Pollack. Locking of HeNe laser modes induced by synchronous intracavity modulation. *Applied Physics Letters*, 5(1):4–5, 1964.

[9] D. Strickland and G. Mourou. Compression of amplified chirped optical pulses. *Optics Communications*, **56**:219, 1985.

[10] D. E. Spence, P. N. Kean, and W. Sibbett. 60-fsec pulse generation from a self-mode-locked Ti:sapphire laser. *Optics Letters*, **16**:42, 1991.

[11] A. H. Zewail. Laser femtochemistry. *Science*, 242(4886):1645–1653, 1988.

[12] N. H. Burnett, H. A. Baldis, M. C. Richardson, and G. D. Enright. Harmonic generation in CO2 laser target interaction. *Applied Physics Letters*, 31(3):172–174, 1977.

[13] A. McPherson, G. Gibson, H. Jara, U. Johann, T. S. Luk, I. A. McIntyre, K. Boyer, and C. K. Rhodes. Studies of multiphoton production of vacuum-ultraviolet radiation in the rare gases. *Journal of the Optical Society of America B*, 4:595–601, 1987.

[14] M. Ferray, A. L'Huillier, X. Li, L. Lompre, G. Mainfray, and C. Manus. Multiple-harmonic conversion of 1064 nm radiation in rare gases. *Journal of Physics B: Atomic, Molecular and Optical Physics*, **21**:L31–L35, 1988.

[15] P. . M. Paul, E. Toma, P. Breger, G. Mullot, F. Augé, P. Balcou, H. Muller, and P. Agostini. Observation of a train of attosecond pulses from high harmonic generation. *Science*, 292(5522):1689–1692, 2001.

[16] K. Klünder, J. M. Dahlström, M. Gisselbrecht, T. Fordell, M. Swoboda, D. Guénot, P. Johnsson, J. Caillat, J. Mauritsson, A. Maquet, R. Taïeb, and A. L'Huillier. Probing single-photon ionization on the attosecond time scale. *Physical Review Letters*, 106:143002, 2011.

[17] E. P. Månsson, D. Guénot, C. L. Arnold, D. Kroon, S. Kasper, J. M. Dahlström, E. Lindroth, A. S. Kheifets, A. L'Huillier, S. L. Sorensen, et al. Double ionization probed on the attosecond timescale. *Nature Physics*, 10:207–211, 2014.

[18] M. Kotur, D. Guénot, A. Jiménez-Galán, D. Kroon, E. W. Larsen, M. Louisy, S. Bengtsson, M. Miranda, J. Mauritsson, C. L. Arnold, S. E. Canton, M. Gisselbrecht, T. Carette, J. M. Dahlström, E. Lindroth, A. Maquet, L. Argenti, F. Martín, and A. L'Huillier. Spectral phase measurement of a Fano resonance using tunable attosecond pulses. *Nature Communications*, 7:10566–, 2016.

[19] V. Gruson, L. Barreau, Á. Jiménez-Galan, F. Risoud, J. Caillat, A. Maquet, B. Carré, F. Lepetit, J.-F. Hergott, T. Ruchon, L. Argenti, R. Taïeb, F. Martín, and P. Salières. Attosecond dynamics through a fano resonance: Monitoring the birth of a photoelectron. *Science*, 354(6313):734–738, 2016.

[20] S. Haessler, B. Fabre, J. Higuet, J. Caillat, T. Ruchon, P. Breger, B. Carré, E. Constant, A. Maquet, E. Mével, P. Salières, R. Taïeb, and Y. Mairesse. Phase-resolved attosecond near-threshold photoionization of molecular nitrogen. *Physical Review A*, 80:011404, 2009.

[21] R. Locher, L. Castiglioni, M. Lucchini, M. Greif, L. Gallmann, J. Osterwalder, M. Hengsberger, and U. Keller. Energy-dependent photoemission delays from noble metal surfaces by attosecond interferometry. *Optica*, 2(5):405–410, 2015.

[22] M. Schultze, M. Fiess, N. Karpowicz, J. Gagnon, M. Korbman, M. Hofstetter, S. Neppl, A. L. Cavalieri, Y. Komninos, T. Mercouris, C. A. Nicolaides, R. Pazourek, S. Nagele, J. Feist, J. Burgdörfer, A. M. Azzeer, R. Ernstorfer, R. Kienberger, U. Kleineberg, E. Goulielmakis, F. Krausz, and V. S. Yakovlev. Delay in photoemission. *Science*, 328(5986):1658–1662, 2010.

[23] A. G. J. MacFarlane, J. P. Dowling, and G. J. Milburn. Quantum technology: the second quantum revolution. *Philosophical Transactions of the Royal Society of London. Series A: Mathematical, Physical and Engineering Sciences*, 361(1809):1655–1674, 2003.

[24] M. Atzori and R. Sessoli. The second quantum revolution: Role and challenges of molecular chemistry. *Journal of the American Chemical Society*, 141(29):11339–11352, 2019.

[25] P. Stammer, J. Rivera-Dean, A. Maxwell, T. Lamprou, A. Ordóñez, M. F. Ciappina, P. Tzallas, and M. Lewenstein. Quantum electrodynamics of intense laser-matter interactions: A tool for quantum state engineering. *PRX Quantum*, 4:010201, 2023.

[26] C. Bourassin-Bouchet, L. Barreau, V. Gruson, J.-F. Hergott, F. Quéré, P. Salières, and T. Ruchon. Quantifying decoherence in attosecond metrology. *Physical Review X*, 10:031048, 2020.

[27] L.-M. Koll, L. Maikowski, L. Drescher, T. Witting, and M. J. J. Vrakking. Experimental control of quantum-mechanical entanglement in an attosecond pump-probe experiment. *Physical Review Letters*, 128:043201, 2022.

[28] J. Duris, S. Li, T. Driver, E. G. Champenois, J. P. MacArthur, A. A. Lutman, Z. Zhang, P. Rosenberger, J. W. Aldrich, R. Coffee, G. Coslovich, F.-J. Decker, J. M. Glownia, G. Hartmann, W. Helml, A. Kamalov, J. Knurr, J. Krzywinski, M.-F. Lin, J. P. Marangos, M. Nantel, A. Natan, J. T. O'Neal, N. Shivaram, P. Walter, A. L. Wang, J. J. Welch, T. J. A. Wolf, J. Z. Xu, M. F. Kling, P. H. Bucksbaum, A. Zholents, Z. Huang, J. P. Cryan, and A. Marinelli. Tunable isolated attosecond x-ray pulses with gigawatt peak power from a free-electron laser. *Nature Photonics*, 14(1):30–36, 2020.

[29] C. Heyl, J. Güdde, A. L'Huillier, and U. Höfer. High-order harmonic generation with μj laser pulses at high repetition rates. *Journal of Physics B: Atomic, Molecular and Optical Physics*, 45(7):074020, 2012.

[30] S. Kühn, M. Dumergue, S. Kahaly, S. Mondal, M. Füle, T. Csizmadia, B. Farkas, B. Major, Z. Várallyay, E. Cormier, M. Kalashnikov, F. Calegari, M. Devetta, F. Frassetto, E. Månsson, L. Poletto, S. Stagira, C. Vozzi, M. Nisoli, P. Rudawski, S. Maclot, F. Campi, H. Wikmark, C. L. Arnold, C. M. Heyl, P. Johnsson, A. L'Huillier, R. Lopez-Martens, S. Haessler, M. Bocoum, F. Boehle, A. Vernier,

G. Iaquaniello, E. Skantzakis, N. Papadakis, C. Kalpouzos, P. Tzallas, F. Lépine, D. Charalambidis, K. Varjú, K. Osvay, and G. Sansone. The ELI-ALPS facility: the next generation of attosecond sources. *Journal of Physics B: Atomic, Molecular and Optical Physics*, 50(13):132002, 2017.

[31] J. Rothhardt, M. Krebs, S. Hädrich, S. Demmler, J. Limpert, and A. Tünnermann. Absorption-limited and phase-matched high harmonic generation in the tight focusing regime. *New Journal of Physics*, 16(3):033022, 2014.

[32] S. Mikaelsson, J. Vogelsang, C. Guo, I. Sytcevich, A.-L. Viotti, F. Langer, Y.-C. Cheng, S. Nandi, W. Jin, A. Olofsson, R. Weissenbilder, J. Mauritsson, A. L'Huillier, M. Gisselbrecht, and C. L. Arnold. A high-repetition rate attosecond light source for time-resolved coincidence spectroscopy. *Nanophotonics*, 10(1):117–128, 2021.

[33] C. M. Heyl, H. Coudert-Alteirac, M. Miranda, M. Louisy, K. Kovacs, V. Tosa, E. Balogh, K. Varjú, A. L'Huillier, A. Couairon, and C. L. Arnold. Scale-invariant nonlinear optics in gases. *Optica*, 3(1):75–81, 2016.

[34] V. Nefedova, M. Albrecht, M. Kozlová, and J. Nejdl. Development of a high-flux xuv source based on high-order harmonic generation. *Journal of Electron Spectroscopy and Related Phenomena*, 220:9–13, 2017.

[35] O. Martinez. 3000 times grating compressor with positive group velocity dispersion: Application to fiber compensation in 1.3-1.6 μm region. *IEEE Journal of Quantum Electronics*, 23(1):59 – 64, 1987.

[36] E. Treacy. Optical pulse compression with diffraction gratings. *IEEE Journal of Quantum Electronics*, 5(9):454 – 458, 1969.

[37] G. N. Lewis, D. Lipkin, and T. T. Magel. Reversible photochemical processes in rigid media. a study of the phosphorescent state. *Journal of the American Chemical Society*, 63(11):3005–3018, 1941.

[38] P. A. Franken, A. E. Hill, C. W. Peters, and G. Weinreich. Generation of optical harmonics. *Physical Review Letters*, **7**:118, 1961.

[39] R. W. Boyd. *Nonlinear Optics*. Academic Press, 2003.

[40] S. Ghimire, A. D. DiChiara, E. Sistrunk, P. Agostini, L. F. DiMauro, and D. A. Reis. Observation of high-order harmonic generation in a bulk crystal. *Nature Physics*, 7(2):138–141, 2010.

[41] T. T. Luu, Z. Yin, A. Jain, T. Gaumnitz, Y. Pertot, J. Ma, and H. J. Wörner. Extreme–ultraviolet high–harmonic generation in liquids. *Nature Communications*, 9(1):3723, 2018.

[42] K. C. Kulander, K. J. Schafer, and J. L. Krause. Dynamics of short-pulse excitation, ionization and harmonic conversion. In *Super-Intense Laser-Atom Physics*. Plenum Press, New York, 1993.

[43] P. B. Corkum. Plasma perspective on strong field multiphoton ionization. *Physical Review Letters*, 71:1994–1997, 1993.

[44] J. L. Krause, K. J. Schafer, and K. C. Kulander. High-order harmonic generation from atoms and ions in the high intensity regime. *Physical Review Letters*, 68:3535–3538, 1992.

[45] J. L. Krause, K. J. Schafer, and K. C. Kulander. Optical harmonic-generation in atomic and molecular-hydrogen. *Chemical Physics Letters*, 178(5-6):573–578, 1991.

[46] M. Lewenstein, P. Balcou, M. Y. Ivanov, A. L'Huillier, and P. B. Corkum. Theory of high-harmonic generation by low-frequency laser fields. *Physical Review A*, 49:2117–2132, 1994.

[47] M. C. Kohler, C. Ott, P. Raith, R. Heck, I. Schlegel, C. H. Keitel, and T. Pfeifer. High harmonic generation via continuum wave-packet interference. *Physical Review Letters*, 105:203902, 2010.

[48] A. Pukhov, S. Gordienko, and T. Baeva. Temporal Structure of Attosecond Pulses from Intense Laser-Atom Interactions. *Physical Review Letters*, 91:173002, 2003.

[49] B. Shan and Z. Chang. Dramatic extension of the high-order harmonic cutoff by using a long-wavelength driving field. *Physical Review A*, 65(1):011804, 2001.

[50] K. Schiessl, K. L. Ishikawa, E. Persson, and J. Burgdorfer. Quantum path interference in the wavelength dependence of high-harmonic generation. *Physical Review Letters*, 99(25):4, 2007.

[51] M. V. Frolov, N. L. Manakov, A. A. Silaev, and N. V. Vvedenskii. Analytic description of high-order harmonic generation by atoms in a two-color laser field. *Physical Review A*, 81(6):063407, 2010.

[52] A. D. Shiner, C. Trallero-Herrero, N. Kajumba, H.-C. Bandulet, D. Comtois, F. Légaré, M. Giguère, J.-C. Kieffer, P. B. Corkum, and D. M. Villeneuve. Wavelength scaling of high harmonic generation efficiency. *Physical Review Letters*, 103:073902, 2009.

[53] J. Tate, T. Auguste, H. G. Muller, P. Salieres, P. Agostini, and L. F. DiMauro. Scaling of Wave-Packet Dynamics in an Intense Midinfrared Field. *Physical Review Letters*, 98:013901, 2007.

[54] A. Fleischer, O. Kfir, T. Diskin, P. Sidorenko, and O. Cohen. Spin angular momentum and tunable polarization in high-harmonic generation. *Nature Photonics*, 8(7):543–549, 2014.

[55] O. Kfir, P. Grychtol, E. Turgut, R. Knut, D. Zusin, D. Popmintchev, T. Popmintchev, H. Nembach, J. M. Shaw, A. Fleischer, H. Kapteyn, M. Murnane, and O. Cohen. Generation of bright phase-matched circularly-polarized extreme ultraviolet high harmonics. *Nature Photonics*, 9(2):99–105, 2015.

[56] T. Fan, P. Grychtol, R. Knut, C. Hernández-García, D. D. Hickstein, D. Zusin, C. Gentry, F. J. Dollar, C. A. Mancuso, C. W. Hogle, O. Kfir, D. Legut, K. Carva, J. L. Ellis, K. M. Dorney, C. Chen, O. G. Shpyrko, E. E. Fullerton, O. Cohen, P. M. Oppeneer, D. B. Milosevic, A. Becker, A. A. Jaron-Becker, T. Popmintchev, M. M. Murnane, and H. C. Kapteyn. Bright circularly polarized soft x-ray high harmonics for x-ray magnetic circular dichroism. *Proceedings of the National Academy of Sciences*, 112(46):14206–14211, 2015.

[57] M. Bellini, C. Lyngå, A. Tozzi, M. Gaarde, C. Delfin, T. Hänsch, A. L'Huillier, and C.-G. Wahlström. Temporal coherence of ultrashort high-order harmonic pulses. *Physical Review Letters*, 81:297, 1998.

[58] M. D. Perry and J. K. Crane. High-order harmonic emission from mixed fields. *Physical Review A*, 48:R4051–R4054, 1993.

[59] P. Salières, B. Carré, L. L. Déroff, F. Grasbon, G. G. Paulus, H. Walther, R. Kopold, W. Becker, D. B. Milošević, A. Sanpera, and M. Lewenstein. Feynman's Path-Integral Approach for Intense-Laser-Atom Interactions. *Science*, **292**:902, 2001.

[60] M. B. Gaarde and K. J. Schafer. Quantum path distributions for high-order harmonics in rare gas atoms. *Physical Review A*, **65**:031406(R), 2002.

[61] M. R. Miller, C. Hernández-García, A. Jaro ń Becker, and A. Becker. Targeting multiple rescatterings through vuv-controlled high-order-harmonic generation. *Physical Review A*, 90:053409, 2014.

[62] C. Hernández-García, A. Picón, J. San Román, and L. Plaja. Attosecond extreme ultraviolet vortices from high-order harmonic generation. *Physical Review Letters*, 111:083602, 2013.

[63] C. Spielmann, N. H. Burnett, S. Sartania, R. Koppitsch, M. Schnürer, C. Kan, M. Lenzner, P. Wobrauschek, and F. Krausz. Generation of coherent x-rays in the water window using 5-femtosecond laser pulses. *Science*, 278(5338):661–664, 1997.

[64] S. M. Teichmann, F. Silva, S. L. Cousin, M. Hemmer, and J. Biegert. 0.5-kev soft x-ray attosecond continua. *Nature Communications*, 7(1):11493, 2016.

[65] G. De Stasio, B. Gilbert, T. Nelson, R. Hansen, J. Wallace, D. Mercanti, M. Capozi, P. A. Baudat, P. Perfetti, G. Margaritondo, and B. P. Tonner. Feasibility tests of transmission x-ray photoelectron emission microscopy of wet samples. *Review of Scientific Instruments*, 71(1):11–14, 2000.

[66] M. Berglund, L. Rymell, M. Peuker, T. Wilhein, and H. M. Hertz. Compact water-window transmission x-ray microscopy. *Journal of Microscopy*, 197(Pt 3):268–273, 2000.

[67] T. Popmintchev, M.-C. Chen, D. Popmintchev, P. Arpin, S. Brown, S. Alisauskas, G. Andriukaitis, T. Balciunas, O. Mücke, A. Pugzlys, A. Baltuska, B. Shim, S. Schrauth, A. Gaeta, C. Hernández-Garcia, L. Plaja, A. Becker, A. J.-B., M. Murnane, and H. Kapteyn. Bright coherent ultrahigh harmonics in the keV X-ray regime from mid-infrared femtosecond lasers. *Science*, 336(6086):1287–1291, 2012.

[68] P. Salières, A. L'Huillier, and M. Lewenstein. Coherence control of high-order harmonics. *Physical Review Letters*, 74:3776–3779, 1995.

[69] Y. Mairesse, A. de Bohan, L. J. Frasinski, H. Merdji, L. C. Dinu, P. Monchicourt, P. Breger, M. Kovačev, R. Taïeb, B. Carré, H. G. Muller, P. Agostini, and P. Salières. Attosecond synchronization of high-harmonic soft X-rays. *Science*, 302:1540, 2003.

[70] C. Guo, A. Harth, S. Carlström, Y.-C. Cheng, S. Mikaelsson, E. Mårsell, C. Heyl, M. Miranda, M. Gisselbrecht, M. B. Gaarde, K. J. Schafer, A. Mikkelsen, J. Mauritsson, C. L. Arnold, and A. L'Huillier. Phase control of attosecond pulses in a train. *Journal of Physics B: Atomic, Molecular and Optical Physics*, 51(3):034006, 2018.

[71] A. Zaïr, M. Holler, F. Schapper, J. Biegert, L. Gallmann, U. Keller, A. Wyatt, A. Monmayrant, I. Walmsley, E. Cormier, T. Auguste, J. Caumes, and P. Salières. Quantum Path Interferences in High-Order Harmonic Generation. *Physical Review Letters*, 100:143902–1–4, 2008.

[72] J. H. Eberly, Q. Su, and J. Javanainen. Nonlinear Light Scattering Accompanying Multiphoton Ionization. *Physical Review Letters*, 62:881, 1989.

[73] B. Shore and K. Kulander. Generation of optical harmonics by intense pulses of laser radiation. *Journal of Modern Optics*, 36(7):857–875, 1989.

[74] K. C. Kulander and B. W. Shore. Calculations of Multiple-Harmonic Conversion of 1064-nm Radiation in Xe. *Physical Review Letters*, 62:524, 1989.

[75] A. L'Huillier, P. Balcou, S. Candel, K. J. Schafer, and K. C. Kulander. Calculations of high-order harmonic-generation processes in xenon at 1064 nm. *Physical Review A*, 46:2778–2790, 1992.

[76] B. Sheehy, J. D. D. Martin, L. F. DiMauro, P. Agostini, K. J. Schafer, M. B. Gaarde, and K. C. Kulander. High harmonic generation at long wavelengths. *Physical Review Letters*, 83:5270–5273, 1999.

[77] M. Lewenstein, K. C. Kulander, K. J. Schafer, and P. H. Bucksbaum. Rings in above-threshold ionization: A quasiclassical analysis. *Physical Review A*, 51:1495–1507, 1995.

[78] A. Dubrouil, O. Hort, F. Catoire, D. Descamps, S. Petit, E. Mével, V. V. Strelkov, and E. Constant. Spatio–spectral structures in high-order harmonic beams generated with terawatt 10-fs pulses. *Nature Communications*, 5(1):4637, 2014.

[79] C. M. Heyl, J. Güdde, U. Höfer, and A. L'Huillier. Spectrally resolved maker fringes in high-order harmonic generation. *Physical Review Letters*, 107:033903, 2011.

[80] K. Amini, J. Biegert, F. Calegari, A. Chacon, M. F. Ciappina, A. Dauphin, D. K. Efimov, C. F. de Morisson Faria, K. Giergiel, P. Gniewek, A. S. Landsman, M. Lesiuk, M. Mandrysz, A. S. Maxwell, R. Moszynski, L. Ortmann, J. A. Perez-Hernandez, A. Picon, E. Pisanty, J. Prauzner-Bechcicki, K. Sacha, N. Suarez, A. Zair, J. Zakrzewski, and M. Lewenstein. Symphony on strong field approximation. *Reports on Progress in Physics*, 82(11):116001, 2019.

[81] A.-T. Le, H. Wei, C. Jin, and C. D. Lin. Strong-field approximation and its extension for high-order harmonic generation with mid-infrared lasers. *Journal of Physics B: Atomic, Molecular and Optical Physics*, 49(5):053001, 2016.

[82] N. B. Delone and V. P. Krainov. *Atoms in strong light fields / N.B. Delone, V.P. Krainov ; [translator, Eugeny M. Yankovsky]*. Springer-Verlag Berlin ; New York, 1985.

[83] G. Farkas and C. Tóth. Proposal for attosecond light pulse generation using laser induced multiple-harmonic conversion processes in rare gases. *Physics Letters A*, **168**:447, 1992.

[84] S. E. Harris, J. J. Macklin, and T. W. Hänsch. Atomic scale temporal structure inherent to high-order harmonic generation. *Optics Communications*, **100**:487, 1993.

[85] P. Antoine, A. L'Huillier, and M. Lewenstein. Attosecond pulse trains using high–order harmonics. *Physical Review Letters*, 77:1234–1237, 1996.

[86] M. Hentschel, R. Kienberger, C. Spielmann, G. A. Reider, N. Milosevic, T. Brabec, P. Corkum, U. Heinzmann, M. Drescher, and F. Krausz. Attosecond metrology. *Nature*, 414(6863):509–513, 2001.

[87] H. R. Telle, G. Steinmeyer, A. E. Dunlop, J. Stenger, D. H. Sutter, and U. Keller. Carrier-envelope offset phase control: A novel concept for absolute optical frequency measurement and ultrashort pulse generation. *Applied Physics B*, 69:327, 1999.

[88] A. Baltuška, T. Udem, M. Uiberacker, M. Hentschel, E. Goulielmakis, C. Gohle, R. Holzwarth, V. S. Yakovlev, A. Scrinzi, T. W. Hänsch, and F. Krausz. Attosecond control of electronic processes by intense light fields. *Nature*, **421**:611, 2003.

[89] G. Sansone, E. Benedetti, F. Calegari, C. Vozzi, L. Avaldi, R. Flammini, L. Poletto, P. Villoresi, C. Altucci, R. Velotta, et al. Isolated single-cycle attosecond pulses. *Science*, 314(5798):443–446, 2006.

[90] F. Ferrari, F. Calegari, M. Lucchini, C. Vozzi, S. Stagira, G. Sansone, and M. Nisoli. High-energy isolated attosecond pulses generated by above-saturation few-cycle fields. *Nature Photonics*, 4(12):875–879, 2010.

[91] R. Kienberger, E. Goulielmakis, M. Uiberacker, A. Baltuška, V. Yakovlev, F. Bammer, A. Scrinzi, T. Westerwalbesloh, U. Kleineberg, U. Heinzmann, M. Drescher, and F. Krausz. Atomic transient recorder. *Nature*, 427:817, 2004.

[92] H. Vincenti and F. Quéré. Attosecond lighthouses: How to use spatiotemporally coupled light fields to generate isolated attosecond pulses. *Physical Review Letters*, 108:113904, 2012.

[93] C. M. Heyl, S. N. Bengtsson, S. Carlström, J. Mauritsson, C. L. Arnold, and A. L'Huillier. Noncollinear optical gating. *New Journal of Physics*, 16(5):052001, 2014.

[94] K. Varjú, Y. Mairesse, B. Carre, M. B. Gaarde, P. Johnsson, S. Kazamias, R. Lopez-Martens, J. Mauritsson, K. J. Schafer, P. Balcou, A. L'Huillier, and P. Salières. Frequency chirp of harmonic and attosecond pulses. *Journal of Modern Optics*, 52(2-3):379–394, 2005.

[95] P. F. Moulton. Spectroscopic and laser characteristics of ti:al2o3. *Journal of the Optical Society of America B*, 3(1):125–133, 1986.

[96] A. Offner. Unit power imaging catoptric anastigmat (u.s. patent no. 3,748,015), 1971.

[97] G. Cheriaux, P. Rousseau, F. Salin, J. P. Chambaret, B. Walker, and L. F. Dimauro. Aberration-free stretcher design for ultrashort-pulse amplification. *Optics Letters*, 21(6):414–416, 1996.

[98] P. Tournois. Acousto-optic programmable dispersive filter for adaptive compensation of group delay time dispersion in laser systems. *Optics Communications*, **140**:245, 1997.

[99] T. Oksenhendler, D. Kaplan, P. Tournois, G. M. Greetham, and F. Estable. Intracavity acousto-optic programmable gain control for ultra-wide-band regenerative amplifiers. *Applied Physics B*, 83(4):491–494, 2006.

[100] S. Backus, C. G. Durfee, G. Mourou, H. C. Kapteyn, and M. M. Murnane. 0.2-tw laser system at 1 khz. *Optics Letters*, 22(16):1256–1258, 1997.

[101] J.-L. Tapie. *Ph.D. thesis*. PhD thesis, Universite de Paris-Sud, 1991.

[102] A. Moulet, S. Grabielle, C. Cornaggia, N. Forget, and T. Oksenhendler. Single-shot, high-dynamic-range measurement of sub-15 fs pulses by self-referenced spectral interferometry. *Optics Letters*, 35(22):3856–3858, 2010.

[103] T. Oksenhendler, S. Coudreau, N. Forget, V. Crozatier, S. Grabielle, R. Herzog, O. Gobert, and D. Kaplan. Self-referenced spectral interferometry. *Applied Physics B*, 99(1):7–12, 2010.

[104] P. Balcou, P. Sali'eres, A. L'Huillier, and M. Lewenstein. Generalized phase-matching conditions for high harmonics: The role of field-gradient forces. *Physical Review A*, 55:3204–3210, 1997.

[105] D. Irimia, D. Dobrikov, R. Kortekaas, H. Voet, D. A. van den Ende, W. A. Groen, and M. H. M. Janssen. A short pulse (7 us FWHM) and high repetition rate (dc-5kHz) cantilever piezovalve for pulsed atomic and molecular beams. *Review of Scientific Instruments*, 80(11):113303, 2009.

[106] K. T. Kim, C. M. Kim, M.-G. Baik, G. Umesh, and C. H. Nam. Single sub-50-attosecond pulse generation from chirp-compensated harmonic radiation using material dispersion. *Physical Review A*, 69:051805, 2004.

[107] N. Nakano, H. Kuroda, T. Kita, and T. Harada. Development of a flat-field grazing-incidence xuv spectrometer and its application in picosecond xuv spectroscopy. *Applied Optics*, 23(14):2386–2392, 1984.

[108] P. Antoine, A. L'Huillier, M. Lewenstein, P. Salières, and B. Carré. Theory of high-order harmonic generation by an elliptically polarized laser field. *Physical Review A*, 53:1725, 1996.

[109] D. Popmintchev, C. Hernández-García, F. Dollar, C. Mancuso, J. A. Pérez-Hernández, M.-C. Chen, A. Hankla, X. Gao, B. Shim, A. L. Gaeta, M. Tarazkar, D. A. Romanov, R. J. Levis, J. A. Gaffney, M. Foord, S. B. Libby, A. Jaron-Becker, A. Becker, L. Plaja, M. M. Murnane, H. C. Kapteyn, and T. Popmintchev. Ultraviolet surprise: Efficient soft x-ray high-harmonic generation in multiply ionized plasmas. *Science*, 350(6265):1225–1231, 2015.

[110] M. D. Feit and J. A. Fleck. Light propagation in graded-index optical fibers. *Applied Optics*, 17(24):3990–3998, 1978.

[111] M. D. Feit and J. A. Fleck. Beam nonparaxiality, filament formation, and beam breakup in the self-focusing of optical beams. *Journal of the Optical Society of America B*, 5(3):633–640, 1988.

[112] A. Couairon, E. Brambilla, T. Corti, D. Majus, O. de J. Ramírez-Góngora, and M. Kolesik. Practitioner's guide to laser pulse propagation models and simulation. *The European Physical Journal Special Topics*, 199(1):5–76, 2011.

[113] M. B. Gaarde, J. L. Tate, and K. J. Schafer. Macroscopic aspects of attosecond pulse generation. *Journal of Physics B: Atomic, Molecular and Optical Physics*, 41(13):132001, 2008.

[114] T. Brabec and F. Krausz. Intense few-cycle laser fields: Frontiers of nonlinear optics. *Reviews of Modern Physics*, 72:545–591, 2000.

[115] C. Altucci, V. Tosa, and R. Velotta. Beyond the single-atom response in isolated attosecond-pulse generation. *Physical Review A*, 75:061401, 2007.

[116] C. M. Heyl, C. L. Arnold, A. Couairon, and A. L'Huillier. Introduction to macroscopic power scaling principles for high-order harmonic generation. *Journal of Physics B: Atomic, Molecular and Optical Physics*, 50(1):013001, 2017.

[117] A. Comby, D. Descamps, S. Beauvarlet, A. Gonzalez, F. Guichard, S. Petit, Y. Zaouter, and Y. Mairesse. Cascaded harmonic generation from a fiber laser: a milliwatt xuv source. *Optics Express*, 27(15):20383–20396, 2019.

[118] J. Boullet, Y. Zaouter, J. Limpert, S. Petit, Y. Mairesse, B. Fabre, J. Higuet, E. Mével, E. Constant, and E. Cormier. High-order harmonic generation at a megahertz-level repetition rate directly driven by an ytterbium-doped-fiber chirped-pulse amplification system. *Optics Letters*, 34(9):1489–1491, 2009.

[119] S. Hädrich, A. Klenke, J. Rothhardt, M. Krebs, A. Hoffmann, O. Pronin, V. Pervak, J. Limpert, and A. Tünnermann. High photon flux table-top coherent extreme-ultraviolet source. *Nature Photonics*, 8(10):779–783, 2014.

[120] H. Coudert-Alteirac, H. Dacasa, F. Campi, E. Kueny, B. Farkas, F. Brunner, S. Maclot, B. Manschwetus, H. Wikmark, J. Lahl, L. Rading, J. Peschel, B. Major, K. Varjú, G. Dovillaire, P. Zeitoun, P. Johnsson, A. L'Huillier, and P. Rudawski. Micro-focusing of broadband high-order harmonic radiation by a double toroidal mirror. *Applied Sciences*, 7(11):1159, 2017.

[121] C. Kleine, M. Ekimova, G. Goldsztejn, S. Raabe, C. Strüber, J. Ludwig, S. Yarlagadda, S. Eisebitt, M. J. J. Vrakking, T. Elsaesser, E. T. J. Nibbering, and A. Rouzée. Soft x-ray absorption spectroscopy of aqueous solutions using a table-top

femtosecond soft x-ray source. *The Journal of Physical Chemistry Letters*, 10(1):52–58, 2019.

[122] N. Tsatrafyllis, B. Bergues, H. Schröder, L. Veisz, E. Skantzakis, D. Gray, B. Bodi, S. Kuhn, G. D. Tsakiris, D. Charalambidis, and P. Tzallas. The ion microscope as a tool for quantitative measurements in the extreme ultraviolet. *Scientific Reports*, 6(1):21556, 2016.

[123] Y. Fu, K. Nishimura, R. Shao, A. Suda, K. Midorikawa, P. Lan, and E. J. Takahashi. High efficiency ultrafast water-window harmonic generation for single-shot soft x-ray spectroscopy. *Communications Physics*, 3(1):92, 2020.

[124] A. L'Huillier, K. J. Schafer, and K. C. Kulander. Theoretical aspects of intense field harmonic generation. *Journal of Physics B: Atomic, Molecular and Optical Physics*, 24(15):3315–3341, 1991.

[125] K. Midorikawa, Y. Nabekawa, and A. Suda. Xuv multiphoton processes with intense high-order harmonics. *Progress in Quantum Electronics*, 32(2):43–88, 2008.

[126] W. Boutu, T. Auguste, O. Boyko, I. Sola, P. Balcou, L. Binazon, O. Gobert, H. Merdji, C. Valentin, E. Constant, E. Mével, and B. Carré. High-order-harmonic generation in gas with a flat-top laser beam. *Physical Review A*, 84:063406, 2011.

[127] C. M. Heyl, H. Coudert-Alteirac, M. Miranda, M. Louisy, K. Kovacs, V. Tosa, E. Balogh, K. Varjú, A. L'Huillier, A. Couairon, and C. L. Arnold. Supplement 1: Scale-invariant nonlinear optics in gases. 2016.

[128] C. Hernández-García, T. Popmintchev, M. M. Murnane, H. C. Kapteyn, L. Plaja, A. Becker, and A. Jaron-Becker. Group velocity matching in high-order harmonic generation driven by mid-infrared lasers. *New Journal of Physics*, 18(7):073031, 2016.

[129] R. Klas. *Efficiency scaling of high harmonic generation using ultrashort fiber lasers*. PhD thesis, Friedrich-Schiller Universität Jena, 2021.

[130] P. D. Maker, R. W. Terhune, M. Nisenoff, and C. M. Savage. Effects of dispersion and focusing on the production of optical harmonics. *Physical Review Letters*, 8:21–22, 1962.

[131] S. Kazamias, D. Douillet, F. Weihe, C. Valentin, A. Rousse, S. Sebban, G. Grillon, F. Augé, D. Hulin, and P. Balcou. Global optimization of high harmonic generation. *Physical Review Letters*, 90:193901, 2003.

[132] A. Rundquist, C. G. Durfee, Z. Chang, C. Herne, S. Backus, M. M. Murnane, and H. C. Kapteyn. Phase-matched generation of coherent soft x-rays. *Science*, 280(5368):1412–1415, 1998.

[133] P. Schwerdtfeger and J. K. Nagle. 2018 table of static dipole polarizabilities of the neutral elements in the periodic table. *Molecular Physics*, 117(9-12):1200–1225, 2019.

[134] B. Henke, E. Gullikson, and J. Davis. X-ray interactions: Photoabsorption, scattering, transmission, and reflection at e = 50-30,000 ev, z = 1-92. *Atomic Data and Nuclear Data Tables*, 54(2):181 – 342, 1993.

[135] A. L'Huillier, X. F. Li, and L. A. Lompré. Propagation effects in high-order harmonic generation in rare gases. *Journal of the Optical Society of America B*, 7:527–536, 1990.

[136] S. Feng and H. G. Winful. Physical origin of the gouy phase shift. *Optics Letters*, 26(8):485–487, 2001.

[137] P. Rudawski, C. M. Heyl, F. Brizuela, J. Schwenke, A. Persson, E. Mansten, R. Rakowski, L. Rading, F. Campi, B. Kim, P. Johnsson, and A. L'Huillier. A high-flux high-order harmonic source. *Review of Scientific Instruments*, 84(7):–, 2013.

[138] S. Kazamias, S. Daboussi, O. Guilbaud, K. Cassou, D. Ros, B. Cros, and G. Maynard. Pressure-induced phase matching in high-order harmonic generation. *Physical Review A*, 83, 2011.

[139] C. G. Durfee, A. R. Rundquist, S. Backus, C. Herne, M. M. Murnane, and H. C. Kapteyn. Phase matching of high-order harmonics in hollow waveguides. *Phys. Rev. Lett.*, 83:2187–2190, 1999.

[140] M. J. Abel, T. Pfeifer, P. M. Nagel, W. Boutu, M. J. Bell, C. P. Steiner, D. M. Neumark, and S. R. Leone. Isolated attosecond pulses from ionization gating of high-harmonic emission. *Chemical Physics*, 366(1):9–14, 2009. Attosecond Molecular Dynamics.

[141] A. M. Perelomov, V. S. Popov, and M. V. Terent'ev. Ionization of Atoms in an Alternating Electric Field. *Soviet Journal of Experimental and Theoretical Physics*, 23:924, 1966.

[142] L. V. Keldysh. Ionization in the Field of a Strong Electromagnetic Wave. *Sov. Phys. JETP*, 20:1307, 1965.

[143] N. Boroumand, A. Thorpe, A. M. Parks, and T. Brabec. Keldysh ionization theory of atoms: mathematical details. *Journal of Physics B: Atomic, Molecular and Optical Physics*, 55(21):213001, 2022.

[144] R. Kopold, W. Becker, M. Kleber, and G. G. Paulus. Channel-closing effects in high-order above-threshold ionization and high-order harmonic generation. *Journal of Physics B: Atomic, Molecular and Optical Physics*, 35:217, 2002.

[145] M. Ammosov, N. Delone, and V. Krainov. Tunnelling ionization of complex atoms and of atomic ions in an alternating electromagnetic field. *Soviet Physics - Journal of Experimental and Theoretical Physics*, 64(6):1191–1194, 1986.

[146] S.-F. Zhao, A.-T. Le, C. Jin, X. Wang, and C. D. Lin. Analytical model for calibrating laser intensity in strong-field-ionization experiments. *Physical Review A*, 93:023413, 2016.

[147] M. Geissler, G. Tempea, and T. Brabec. Phase-matched high-order harmonic generation in the nonadiabatic limit. *Physical Review A*, 62:033817, 2000.

[148] D. Kroon, D. Guénot, M. Kotur, E. Balogh, E. W. Larsen, C. M. Heyl, M. Miranda, M. Gisselbrecht, J. Mauritsson, P. Johnsson, K. Varjú, A. L'Huillier, and C. L. Arnold. Attosecond pulse walk-off in high-order harmonic generation. *Optics Letters*, 39(7):2218–2221, 2014.

[149] P. Rudawski, A. Harth, C. Guo, E. Lorek, M. Miranda, C. M. Heyl, E. W. Larsen, J. Ahrens, O. Prochnow, T. Binhammer, U. Morgner, J. Mauritsson, A. L'Huillier, and C. L. Arnold. Carrier-envelope phase dependent high-order harmonic generation with a high-repetition rate opcpa-system. *The European Physical Journal D*, 69(3):70, 2015.

[150] G. L. Yudin and M. Y. Ivanov. Nonadiabatic tunnel ionization: Looking inside a laser cycle. *Physical Review A*, 64:013409, 2001.

[151] B. Minneker, R. Klas, J. Rothhardt, and S. Fritzsche. Critical laser intensity of phase-matched high-order harmonic generation in noble gases. *Photonics*, 10(1), 2023.

[152] T. Popmintchev, M.-C. Chen, O. Cohen, M. E. Grisham, J. J. Rocca, M. M. Murnane, and H. C. Kapteyn. Extended phase matching of high harmonics driven by mid-infrared light. *Optics Letters*, 33(18):2128–2130, 2008.

[153] R. Klas, A. Kirsche, M. Gebhardt, J. Buldt, H. Stark, S. Hädrich, J. Rothhardt, and J. Limpert. Ultra-short-pulse high-average-power megahertz-repetition-rate coherent extreme-ultraviolet light source. *PhotoniX*, 2(1):4, 2021.

[154] T. Popmintchev, M.-C. Chen, P. Arpin, M. M. Murnane, and H. C. Kapteyn. The attosecond nonlinear optics of bright coherent x-ray generation. *Nature Photonics*, 4(12):822–832, 2010.

[155] A. Ludwig, J. Maurer, B. W. Mayer, C. R. Phillips, L. Gallmann, and U. Keller. Breakdown of the dipole approximation in strong-field ionization. *Physical Review Letters*, 113:243001, 2014.

[156] C.-J. Lai and F. X. Kärtner. The influence of plasma defocusing in high harmonic generation. *Optics Express*, 19(23):22377, 2011.

[157] H. T. Kim, I. J. Kim, D. G. Lee, K.-H. Hong, Y. S. Lee, V. Tosa, and C. H. Nam. Optimization of high-order harmonic brightness in the space and time domains. *Physical Review A*, 69:031805, 2004.

[158] D. E. Rivas, B. Major, M. Weidman, W. Helml, G. Marcus, R. Kienberger, D. Charalambidis, P. Tzallas, E. Balogh, K. Kovács, V. Tosa, B. Bergues, K. Varjú, and L. Veisz. Propagation-enhanced generation of intense high-harmonic continua in the 100-ev spectral region. *Optica*, 5(10):1283–1289, 2018.

[159] B. Major, K. Kovács, V. Tosa, P. Rudawski, A. L'Huillier, and K. Varjú. Effect of plasma-core-induced self-guiding on phase matching of high-order harmonic generation in gases. *Journal of the Optical Society of America B*, 36(6):1594–1601, 2019.

[160] H.-W. Sun, P.-C. Huang, Y.-H. Tzeng, J.-T. Huang, C. D. Lin, C. Jin, and M.-C. Chen. Extended phase matching of high harmonic generation by plasma-induced defocusing. *Optica*, 4(8):976–981, 2017.

[161] K. Cassou, S. Daboussi, O. Hort, O. Guilbaud, D. Descamps, S. Petit, E. Mével, E. Constant, and S. Kazamias. Enhanced high harmonic generation driven by high-intensity laser in argon gas-filled hollow core waveguide. *Optics Letters*, 39(13):3770–3773, 2014.

[162] B. Major, M. Kretschmar, O. Ghafur, A. Hoffmann, K. Kovács, K. Varjú, B. Senfftleben, J. Tümmler, I. Will, T. Nagy, D. Rupp, M. J. J. Vrakking, V. Tosa, and B. Schütte. Propagation-assisted generation of intense few-femtosecond high-harmonic pulses. *Journal of Physics: Photonics*, 2(3):034002, 2020.

[163] A. S. Johnson, D. R. Austin, D. A. Wood, C. Brahms, A. Gregory, K. B. Holzner, S. Jarosch, E. W. Larsen, S. Parker, C. S. Strüber, P. Ye, J. W. G. Tisch, and J. P. Marangos. High-flux soft x-ray harmonic generation from ionization-shaped few-cycle laser pulses. *Science Advances*, 4(5):eaar3761, 2018.

[164] B. Major, K. Kovács, E. Svirplys, M. Anus, O. Ghafur, K. Varjú, M. J. J. Vrakking, V. Tosa, and B. Schütte. High-order harmonic generation in a strongly overdriven regime. *Physical Review A*, 107:023514, 2023.

[165] E. E. Fill. Focusing limits of ultrashort laser pulses: analytical theory. *Journal of the Optical Society of America B*, 11(11):2241–2245, 1994.

[166] W. P. Leemans, C. E. Clayton, W. B. Mori, K. A. Marsh, P. K. Kaw, A. Dyson, C. Joshi, and J. M. Wallace. Experiments and simulations of tunnel-ionized plasmas. *Physical Review A*, 46:1091–1105, 1992.

[167] S. Rae. Ionization-induced defocusing of intense laser pulses in high-pressure gases. *Optics Communications*, 97(1):25–28, 1993.

[168] E. Constant, D. Garzella, P. Breger, E. Mével, C. Dorrer, C. Le Blanc, F. Salin, and P. Agostini. Optimizing high harmonic generation in absorbing gases: Model and experiment. *Physical Review Letters*, 82:1668–1671, 1999.

[169] T. Ruchon, C. P. Hauri, K. Varjú, E. Mansten, M. Swoboda, R. López-Martens, and A. L'Huillier. Macroscopic effects in attosecond pulse generation. *New Journal of Physics*, 10 No. 2:025027, 2008.

[170] J. W. Cooper. Photoionization from outer atomic subshells. a model study. *Physical Review*, 128:681–693, 1962.

[171] B. Major and K. Varju. Extended model for optimizing high-order harmonic generation in absorbing gases. *Journal of Physics B: Atomic, Molecular and Optical Physics*, 2021.

[172] J. R. Sutherland, E. L. Christensen, N. D. Powers, S. E. Rhynard, J. C. Painter, and J. Peatross. High harmonic generation in a semi-infinite gas cell. *Optics Express*, 12(19):4430–4436, 2004.

[173] Y. Tao, S. J. Goh, H. M. J. Bastiaens, P. J. M. van der Slot, S. G. Biedron, S. V. Milton, and K. J. Boller. Temporal model for quasi-phase matching in high-order harmonic generation. *Optics Express*, 25(4):3621–3638, 2017.

[174] A. Nayak, I. Orfanos, I. Makos, M. Dumergue, S. Kühn, E. Skantzakis, B. Bodi, K. Varju, C. Kalpouzos, H. I. B. Banks, A. Emmanouilidou, D. Charalambidis, and P. Tzallas. Multiple ionization of argon via multi-xuv-photon absorption induced by 20-gw high-order harmonic laser pulses. *Physical Review A*, 98:023426, 2018.

[175] A. Comby, S. Beaulieu, E. Constant, D. Descamps, S. Petit, and Y. Mairesse. Absolute gas density profiling in high-order harmonic generation. *Optics Express*, 26(5):6001–6009, 2018.

[176] H. Ruf, C. Handschin, R. Cireasa, N. Thiré, A. Ferré, S. Petit, D. Descamps, E. Mével, E. Constant, V. Blanchet, B. Fabre, and Y. Mairesse. Inhomogeneous high harmonic generation in krypton clusters. *Physical Review Letters*, 110:083902, 2013.

[177] P. Balcou, A. S. Dederichs, M. B. Gaarde, and A. L'Huillier. Quantum-path analysis and phase-matching of high-order harmonic generation and high-order frequency mixing processes in strong laser fields. *Journal of Physics B: Atomic, Molecular and Optical Physics*, 32:2973, 1999.

[178] B. Major, O. Ghafur, K. Kovács, K. Varjú, V. Tosa, M. J. J. Vrakking, and B. Schütte. Compact intense extreme-ultraviolet source. *Optica*, 8(7):960–965, 2021.

[179] H. Wikmark, C. Guo, J. Vogelsang, P. W. Smorenburg, H. Coudert-Alteirac, J. Lahl, J. Peschel, P. Rudawski, H. Dacasa, S. Carlström, S. Maclot, M. B. Gaarde, P. Johnsson, C. L. Arnold, and A. L'Huillier. Spatiotemporal coupling of attosecond pulses. *Proceedings of the National Academy of Sciences*, 116(11):4779–4787, 2019.

[180] L. Quintard, V. Strelkov, J. Vabek, O. Hort, A. Dubrouil, D. Descamps, F. Burgy, C. Péjot, E. Mével, F. Catoire, and E. Constant. Optics-less focusing of XUV high-order harmonics. *Science Advances*, 5(4), 2019.

[181] M. Hoflund, J. Peschel, M. Plach, H. Dacasa, K. Veyrinas, E. Constant, P. Smorenburg, H. Wikmark, S. Maclot, C. Guo, C. Arnold, A. L'Huillier, and P. Eng-Johnsson. Focusing properties of high-order harmonics. *Ultrafast Science*, 2021:9797453, 2021.

[182] J. C. P. Koliyadu, S. Kunzel, T. Wodzinski, B. Keitel, J. Duarte, G. O. Williams, C. P. Joao, H. Pires, V. Hariton, M. Galletti, N. Gomes, G. Figueira, J. M. Dias, N. Lopes, P. Zeitoun, E. Plönjes, and M. Fajardo. Optimization and characterization of high-harmonic generation for probing solid density plasmas. *Photonics*, 4(2), 2017.

[183] M. Sayrac, A. A. Kolomenskii, S. Anumula, Y. Boran, N. A. Hart, N. Kaya, J. Strohaber, and H. A. Schuessler. Pressure optimization of high harmonic generation in a differentially pumped ar or h2 gas jet. *Review of Scientific Instruments*, 86(4):043108, 2015.

[184] D. Charalambidis, V. Chikán, E. Cormier, P. Dombi, J. A. Fülöp, C. Janáky, S. Kahaly, M. Kalashnikov, C. Kamperidis, S. Kühn, F. Lepine, A. L'Huillier, R. Lopez-Martens, S. Mondal, K. Osvay, L. Óvári, P. Rudawski, G. Sansone, P. Tzallas, Z. Várallyay, and K. Varjú. *The Extreme Light Infrastructure—Attosecond Light Pulse Source (ELI-ALPS) Project*, pages 181–218. Springer International Publishing, Cham, 2017.

[185] B. Manschwetus, L. Rading, F. Campi, S. Maclot, H. Coudert-Alteirac, J. Lahl, H. Wikmark, P. Rudawski, C. M. Heyl, B. Farkas, T. Mohamed, A. L'Huillier, and P. Johnsson. Two-photon double ionization of neon using an intense attosecond pulse train. *Physical Review A*, 93:061402, 2016.

[186] J. M. Dahlström and E. Lindroth. Study of attosecond delays using perturbation diagrams and exterior complex scaling. *Journal of Physics B: Atomic, Molecular and Optical Physics*, 47(12):124012, 2014.

[187] A. Jiménez-Galán, L. Argenti, and F. Martín. Modulation of Attosecond Beating in Resonant Two-Photon Ionization. *Physical Review Letters*, 113(26):263001, 2014.

[188] Á. Jiménez-Galán, F. Martín, and L. Argenti. Two-photon finite-pulse model for resonant transitions in attosecond experiments. *Physical Review A*, 93(2):023429, 2016.

[189] V. Véniard, R. Taïeb, and A. Maquet. Phase dependence of (N+1) - color (N>1) ir-uv photoionization of atoms with higher harmonics. *Physical Review A*, **54**:721, 1996.

[190] J. Dahlström, A. L'Huillier, and A. Maquet. Introduction to attosecond delays in photoionization. *Journal of Physics B: Atomic, Molecular and Optical Physics*, 45(18):183001, 2012.

[191] J. M. Dahlström, D. Guénot, K. Klünder, M. Gisselbrecht, J. Mauritsson, A. L'Huillier, A. Maquet, and R. Taïeb. Theory of attosecond delays in laser-assisted photoionization. *Chemical Physics*, 414:53–64, 2013.

[192] R. Pazourek, S. Nagele, and J. Burgdörfer. Attosecond chronoscopy of photoemission. *Reviews of Modern Physics*, 87:765–802, 2015.

[193] E. P. Wigner. Lower limit for the energy derivative of the scattering phase shift. *Physical Review*, 98:145–147, 1955.

[194] C. Palatchi, J. M. Dahlström, A. Kheifets, I. Ivanov, D. Canaday, P. Agostini, and L. DiMauro. Atomic delay in helium, neon, argon and krypton. *Journal of Physics B: Atomic, Molecular and Optical Physics*, 47(24):245003, 2014.

[195] D. Guénot, D. Kroon, E. Balogh, E. Larsen, M. Kotur, M. Miranda, T. Fordell, P. Johnsson, J. Mauritsson, M. Gisselbrecht, et al. Measurements of relative photoemission time delays in noble gas atoms. *Journal of Physics B: Atomic, Molecular and Optical Physics*, 47(24):245602, 2014.

[196] M. Ossiander, F. Siegrist, V. Shirvanyan, R. Pazourek, A. Sommer, T. Latka, A. Guggenmos, S. Nagele, J. Feist, J. Burgdörfer, R. Kienberger, and M. Schultze. Attosecond correlation dynamics. *Nature Physics*, 13(3):280–285, 2017.

[197] L. Argenti, A. Jiménez-Galán, J. Caillat, R. Taïeb, A. Maquet, and F. Martín. Control of photoemission delay in resonant two-photon transitions. *Physical Review A*, 95:043426, 2017.

[198] D. Busto, L. Barreau, M. Isinger, M. Turconi, C. Alexandridi, A. Harth, S. Zhong, R. J. Squibb, D. Kroon, S. Plogmaker, M. Miranda, Á. Jiménez-Galán, L. Argenti, C. L. Arnold, R. Feifel, F. Martín, M. Gisselbrecht, A. L'Huillier, and P. Salières. Time–frequency representation of autoionization dynamics in helium. *Journal of Physics B: Atomic, Molecular and Optical Physics*, 51(4):044002, 2018.

[199] U. Fano. Effects of configuration interaction on intensities and phase shifts. *Physical Review*, 124(6):1866, 1961.

[200] C. Alexandridi, D. Platzer, L. Barreau, D. Busto, S. Zhong, M. Turconi, L. Neoričić, H. Laurell, C. L. Arnold, A. Borot, J.-F. Hergott, O. Tcherbakoff, M. Lejman, M. Gisselbrecht, E. Lindroth, A. L'Huillier, J. M. Dahlström, and P. Salières. Attosecond photoionization dynamics in the vicinity of the cooper minima in argon. *Physical Review Research*, 3:L012012, 2021.

[201] J. Peschel, D. Busto, M. Plach, M. Bertolino, M. Hoflund, S. Maclot, J. Vinbladh, H. Wikmark, F. Zapata, E. Lindroth, M. Gisselbrecht, J. M. Dahlström, A. L'Huillier, and P. Eng-Johnsson. Attosecond dynamics of multi-channel single photon ionization. *Nature Communications*, 13(1):5205, 2022.

[202] D. Busto, H. Laurell, D. Finkelstein-Shapiro, C. Alexandridi, M. Isinger, S. Nandi, R. J. Squibb, M. Turconi, S. Zhong, C. L. Arnold, R. Feifel, M. Gisselbrecht, P. Salières, T. Pullerits, F. Martín, L. Argenti, and A. L'Huillier. Probing electronic decoherence with high-resolution attosecond photoelectron interferometry. *The European Physical Journal D*, 76(7):112, 2022.

[203] C. Bourassin-Bouchet and M.-E. Couprie. Partially coherent ultrafast spectrography. *Nature Communications*, 6(1), 2015.

[204] F. Mintert, A. R. Carvalho, M. Kus, and A. Buchleitner. Measures and dynamics of entangled states. *Physics Reports*, 415(4):207–259, 2005.

[205] A. Zaïr, E. Mével, E. Cormier, and E. Constant. Ultrastable collinear delay control setup for attosecond ir-xuv pump-probe experiment. *Journal of the Optical Society of America B*, 35(5):A110–A115, 2018.

[206] H. Ahmadi, S. Kellerer, D. Ertel, M. Moioli, M. Reduzzi, P. K. Maroju, A. J⊠ger, R. N. Shah, J. Lutz, F. Frassetto, L. Poletto, F. Bragheri, R. Osellame, T. Pfeifer, C. D. Schröter, R. Moshammer, and G. Sansone. Collinear setup for delay control in two-color attosecond measurements. *Journal of Physics: Photonics*, 2(2):024006, 2020.

[207] M. Chini, H. Mashiko, H. Wang, S. Chen, C. Yun, S. Scott, S. Gilbertson, and Z. Chang. Delay control in attosecond pump-probe experiments. *Optics Express*, 17(24):21459–21464, 2009.

[208] M. Sabbar, S. Heuser, R. Boge, M. Lucchini, L. Gallmann, C. Cirelli, and U. Keller. Combining attosecond XUV pulses with coincidence spectroscopy. *Review of Scientific Instruments*, 85(10):103113, 2014.

[209] M. Isinger, D. Busto, S. Mikaelsson, S. Zhong, C. Guo, P. Salières, C. L. Arnold, A. L'Huillier, and M. Gisselbrecht. Accuracy and precision of the rabbit technique. *Philosophical Transactions of the Royal Society A: Mathematical, Physical and Engineering Sciences*, 377(2145):20170475, 2019.

[210] D. Kroon. *Attosecond interferometry: techniques and spectroscopy*. PhD thesis, Lund University, 2016.

[211] P. Kruit and F. H. Read. Magnetic field paralleliser for 2π electron-spectrometer and electron-image magnifier. *Journal of Physics E*, 16:313, 1983.

[212] A. T. J. B. Eppink and D. H. Parker. Velocity map imaging of ions and electrons using electrostatic lenses: Application in photoelectron and photofragment ion imaging of molecular oxygen. *Review of Scientific Instruments*, 68:3477, 1997.

[213] J. Gao, J. Wu, Z. Lou, F. Yang, J. Qian, Y. Peng, Y. Leng, Y. Zheng, Z. Zeng, and R. Li. High-order harmonic generation in an x-ray range from laser-induced multivalent ions of noble gas. *Optica*, 9(9):1003–1008, 2022.

[214] G. A. Garcia, L. Nahon, and I. Powis. Two-dimensional charged particle image inversion using a polar basis function expansion. *Review of Scientific Instruments*, 75(11):4989–4996, 2004.

[215] M. Miranda, T. Fordell, C. Arnold, A. L'Huillier, and H. Crespo. Simultaneous compression and characterization of ultrashort laser pulses using chirped mirrors and glass wedges. *Optics Express*, 20(1):688–697, 2012.

[216] M. Miranda, C. L. Arnold, T. Fordell, F. Silva, B. Alonso, R. Weigand, A. L'Huillier, and H. Crespo. Characterization of broadband few-cycle laser pulses with the d-scan technique. *Optics Express*, 20(17):18732–18743, 2012.

[217] G. Wendin. Collective resonance in the 4d10 shell in atomic xe. *Physics Letters A*, 37(5):445–446, 1971.

[218] G. Wendin. Collective effects in atomic photoabsorption spectra. iii. collective resonance in the 4d10 shell in xe. *Journal of Physics B: Atomic and Molecular Physics*, 6(1):42, 1973.

[219] E. Crljen and G. Wendin. Many-body theory of effective local potentials for electronic excitations. iii. application to giant dipole resonances. *Physical Review A*, 35:1571–1581, 1987.

[220] K. T. Cheng and W. R. Johnson. Orbital collapse and the photoionization of the inner $4d$ shells for xe-like ions. *Physical Review A*, 28:2820–2828, 1983.

[221] M. Adam, F. Wuilleumier, S. Krummacher, N. Sandner, V. Schmidt, and W. Mehlhorn. Recent progress in the study of photoionization processes of atomic species by electron spectroscopy using synchrotron radiation. *Journal of Electron Spectroscopy and Related Phenomena*, 15(1):211–224, 1979.

[222] M. Isinger, R. J. Squibb, D. Busto, S. Zhong, A. Harth, D. Kroon, S. Nandi, C. L. Arnold, M. Miranda, J. M. Dahlström, E. Lindroth, R. Feifel, M. Gisselbrecht, and A. L'Huillier. Photoionization in the time and frequency domain. *Science*, 358(6365):893–896, 2017.

[223] L. Drescher, T. Witting, O. Kornilov, and M. J. J. Vrakking. Phase dependence of resonant and antiresonant two-photon excitations. *Physical Review A*, 105:L011101, 2022.

[224] A. Autuori, D. Platzer, M. Lejman, G. Gallician, L. Maeder, A. Covolo, L. Bosse, M. Dalui, D. Bresteau, J.-F. Hergott, O. Tcherbakoff, H. J. B. Marroux, V. Loriot, F. Lepine, L. Poisson, R. Taieb, J. Caillat, and P. Salieres. Anisotropic dynamics of two-photon ionization: An attosecond movie of photoemission. *Science Advances*, 8(12):eabl7594, 2022.

[225] S. Heuser, A. Jiménez Galán, C. Cirelli, C. Marante, M. Sabbar, R. Boge, M. Lucchini, L. Gallmann, I. Ivanov, A. S. Kheifets, J. M. Dahlström, E. Lindroth, L. Argenti, F. Martín, and U. Keller. Angular dependence of photoemission time delay in helium. *Physical Review A*, 94:063409, 2016.

[226] C. Cirelli, C. Marante, S. Heuser, C. L. M. Petersson, Á. J. Galán, L. Argenti, S. Zhong, D. Busto, M. Isinger, S. Nandi, S. Maclot, L. Rading, P. Johnsson, M. Gisselbrecht, M. Lucchini, L. Gallmann, J. M. Dahlström, E. Lindroth, A. L'Huillier, F. Martín, and U. Keller. Anisotropic photoemission time delays close to a fano resonance. *Nature Communications*, 9(1), 2018.

[227] J. Vinbladh, J. M. Dahlström, and E. Lindroth. Many-body calculations of two-photon, two-color matrix elements for attosecond delays. *Physical Review A*, 100:043424, 2019.

[228] M. Turconi, L. Barreau, D. Busto, M. Isinger, C. Alexandridi, A. Harth, R. J. Squibb, D. Kroon, C. L. Arnold, R. Feifel, M. Gisselbrecht, L. Argenti, F. Martín, A. L. 'Huillier, and P. Salières. Spin–orbit-resolved spectral phase measurements around a fano resonance. *Journal of Physics B: Atomic, Molecular and Optical Physics*, 53(18):184003, 2020.

[229] G. S. Agarwal, S. L. Haan, and J. Cooper. Radiative decay of autoionizing states in laser fields. i. general theory. *Physical Review A*, 29:2552–2564, 1984.

[230] A. Zielinski, V. P. Majety, S. Nagele, R. Pazourek, J. Burgdörfer, and A. Scrinzi. Anomalous fano profiles in external fields. *Physical Review Letters*, 115:243001, 2015.

[231] J. Vinbladh, J. M. Dahlström, and E. Lindroth. Relativistic two-photon matrix elements for attosecond delays. *Atoms*, 10(3), 2022.

[232] A.-L. Viotti, M. Seidel, E. Escoto, S. Rajhans, W. P. Leemans, I. Hartl, and C. M. Heyl. Multi-pass cells for post-compression of ultrashort laser pulses. *Optica*, 9(2):197–216, 2022.

[233] M. Han, H. Liang, J. bao Ji, L. C. Sum, K. Ueda, J. M. Rost, and H. J. Wörner. Laser-assisted fano resonance: attosecond quantum control and dynamical imaging, 2023.

[234] J. Su, H. Ni, A. Jaroń-Becker, and A. Becker. Time delays in two-photon ionization. *Physical Review Letters*, 113(26):263002, 2014.

[235] B. Doughty, L. H. Haber, C. Hackett, and S. R. Leone. Photoelectron angular distributions from autoionizing 4s14p66p1 states in atomic krypton probed with femtosecond time resolution. *The Journal of Chemical Physics*, 134(9):094307, 2011.

[236] U. Bhattacharya, T. Lamprou, A. S. Maxwell, A. Ordonez, E. Pisanty, J. Rivera-Dean, P. Stammer, M. F. Ciappina, M. Lewenstein, and P. Tzallas. Strong-laser-field physics, non-classical light states and quantum information science. *Reports on Progress in Physics*, 86(9):094401, 2023.

[237] K. E. Priebe, C. Rathje, S. V. Yalunin, T. Hohage, A. Feist, S. Schäfer, and C. Ropers. Attosecond electron pulse trains and quantum state reconstruction in ultrafast transmission electron microscopy. *Nature Photonics*, 11(12):793–797, 2017.

[238] M. Lewenstein, M. F. Ciappina, E. Pisanty, J. Rivera-Dean, P. Stammer, T. Lamprou, and P. Tzallas. Generation of optical schrödinger cat states in intense laser–matter interactions. *Nature Physics*, 17(10):1104–1108, 2021.

[239] A. Gorlach, O. Neufeld, N. Rivera, O. Cohen, and I. Kaminer. The quantum-optical nature of high harmonic generation. *Nature Communications*, 11(1):4598, 2020.

[240] A. Gorlach, M. E. Tzur, M. Birk, M. Krüger, N. Rivera, O. Cohen, and I. Kaminer. High-harmonic generation driven by quantum light. *Nature Physics*, 2023.

Part II: Publications

Printed by Media-Tryck, Lund 2023 NORDIC SWAN ECOLABEL 3041 0903

LUND
UNIVERSITY

Department of Physics
Division of Atomic Physics
Lund Reports on Atomic Physics, LRAP 593 (2023)

ISBN 978-91-8039-742-1
ISSN 0281-2762

9 789180 397421